

FABRICATION OF MICROFLUIDIC
STRUCTURES BY LASER ABLATION AND
AUTOMATION OF OPTICAL TESTING

Thesis by

Christopher Walker

In Partial Fulfillment of the Requirements for the
degree of

Doctor of Philosophy

CALIFORNIA INSTITUTE OF TECHNOLOGY

Pasadena, California

2010

(Defended June 1st, 2010)

© 2010

Christopher Walker

All Rights Reserved

ACKNOWLEDGEMENTS

Science works best as a collaborative exercise, and I would like to thank the current and former members of our diverse group for their support, whether in the laboratory, or through many conversations. In particular, Jingqing Huang, Aditya Rajagopal, Devin Underwood, Luke Guo, Dr. Zhenyu Li, Dr. Saurabh Vyawahare, Dr. Teresa Emery, Dr. Jörg Schilling, Dr. Tom Baehr-Jones, Professor Michael Hochberg, and Professor Mladen Barbic have been extremely helpful. Over several years, Professor Emil Kartalov has provided a great deal of support and encouragement on the project which makes up the bulk of this thesis, and on other areas in the field of microfluidics. Finally, I would like to thank my advisor, Professor Axel Scherer. Professor Scherer places nearly unreserved trust in his students. His willingness to grant students near autonomy to pursue self initiated, high risk research efforts is an uncommon and deeply generous trait; without his backing and encouragement, this project would not have been possible.

This thesis is dedicated to my parents, Terry and Janis Walker.

ABSTRACT

A versatile, semi-automated instrument to fabricate embedded devices by laser ablation was designed, built, and tested. The expertise required for this came partially from the development of an optical testing system. This system and its utility in testing silicon on oxide waveguide structures are briefly explored. Processes for reproducibly fabricating microfluidic channels and vias were developed. Using one of these processes, design rules for more complex features were developed, and fully three dimensional structures realized. The phenomenon of nonlinear fluidic resistance in deformable channels was explored; a simple analytical model was designed, and compared favorably to measured data. Finally, using this effect, fully embedded valves were developed. With the combination of large scale accurate feature placement, a developed process for three dimensional features, and the development of valves, this instrument is capable of fabricating complex systems of devices, and should prove a useful tool in the future.

TABLE OF CONTENTS

Acknowledgements	iii
Abstract	iv
Table of Contents.....	v
Chapter 1: Motivation for Laser Ablation.....	1
Chapter 2: Automation of Optical Testing.....	5
Stage to Chip Alignment	9
Testing Results	10
Chapter 3: Ablation System Design.....	12
Stage Error Budget	13
Chip Mounting and Fabrication Error	17
Stage and Platen Hardware	19
Laser.....	19
Optomechanics and Optical Alignment.....	20
Hardware Control	21
Alignment Software	22
Control Software.....	26
Chapter 4: Ablation Optics Design	37
Resolution	37
Design Approach.....	40
Volume Resolution.....	45
Chapter 5: Fabrication Process and Results.....	53
Experiment Design	53
Focusing Optics	54
Process Flow and Testing Procedure	55
Fast Aspheric Condenser System Results.....	58
PAC 040 Achromat System Results	59
Microscope Objective System Results	63
Chapter 6: 3D Features Fabricated by Laser Ablation	81
Tolerances and Design Rules	81
Three Dimensional Structures.....	83
Chapter 7: Fluid Flow Characteristics of Channels and Valves.....	89
Channel Flow Characteristics	89
Valves	94
Chapter 8: Future Work.....	98
Alternate Materials for Ablation	98
Microfluidic Chips Configured by Laser Ablation	99
Analog Microfluidic Systems	100
Fabrication of Microfluidic Systems in Printed Circuit Boards.....	102
Bibliography	113

Chapter 1

MOTIVATION FOR LASER ABLATION

Many microfluidic devices today rely on a soft-lithography process pioneered near the turn of the century[1-3] . In the basic technique, replication molding with photoresist molds is used to define grooves in a layer of polydimethylsiloxane (PDMS). These grooves are transformed into channels as the cast elastomeric layer is released from the mold and assembled onto a substrate. Multiple such layers may then be stacked vertically to assemble a multi-layer device[3]. In such a device, channels in different layers cross over one another one to define valves and cross-overs[3]. These architectures have been used to construct sophisticated microfluidic devices for a plethora of important biological, biochemical, and biomedical applications[4, 5] due to the offered advantages of miniaturization, parallelization, and intricate fluidic control at the micro scale.

However, in the basic multi-layer technique[3], channels are defined in thin horizontal layers and thus are geometrically restricted in the plane. Just as most electronic chips require vertical traces, or “vias”, many microfluidic[6] applications require interlayer connectivity.

Consequently, researchers in recent years have developed several techniques to produce vertical connections within microfluidic devices: stacking thin PDMS membrane layers[7, 8], using multiple resist layers[6, 9, 10], solid object printing[11], or through femtosecond laser ablation[12]. Here, we explore the direct fabrication of embedded devices in PDMS by nanosecond laser ablation.

A pulsed laser is focused into a cured slab of PDMS. At the focal point, a volume element (voxel) is ablated by each pulse. Features are cut directly into the bulk material as the stages are scanned (Figure 1). With adequate pulse energy, ablation can be initiated within the bulk of the material; starting a feature at a surface is not required. The laser pulses graphitize the PDMS at the focus. The formula for PDMS is $(\text{CH}_3)_3\text{SiO}[\text{Si}(\text{CH}_3)_2\text{O}]_n\text{Si}(\text{CH}_3)_3$; breakdown products should be dominated by the products of the $[\text{Si}(\text{CH}_3)_2\text{O}]$ group. The ablation waste products likely consist of compounds similar to silica/silicon carbide, and amorphous carbon[13]. Since PDMS is porous, gaseous byproducts ($\text{C}_n\text{H}_{2n+2}$), etc, should slowly diffuse away from the channel through the bulk material. Solid ablation byproducts may then be flushed out with water, leaving the embedded channels. By taking advantage of the high accuracy of computer controlled linear stages, we should be able to position the focal point of the laser to a high accuracy within the block of PDMS.

This technique offers important advantages in comparison to the other fabrication techniques. In comparison with layered techniques, we have complete freedom in defining three dimensional microfluidic structures, as the laser focal point may be freely translated in 3 dimensions. For example, we can ablate a helix with essentially equal ease as with ablating a straight channel, while building a helix with a multilayer photoresist technique[6, 9, 10] would require multiple molds, layers, and labor-intensive alignment. In comparison with other ablative techniques[12, 14, 15] which use ultrafast lasers, this one relies on a nanosecond pulsed laser, and is thus significantly more affordable. While ultrafast ablation does produce superior surface quality[16, 17], typical microfluidic features are on the scales of tens of microns, so rough surface features are functionally acceptable.

This approach is also applicable in fabricating microfluidic structures in transparent materials other than PDMS, which was chosen because of its widespread use in microfluidics. In addition, the described technique is immediately useful in the precise modification of conventionally fabricated devices, e.g. 2-D multi-layer chips. The latter application is likely to grow further in significance since the future will likely see the advent of complete, highly-integrated systems including optical, electronic, and fluidic elements in three-dimensional architectures to offer complex functionalities in a variety of advanced applications.

This project had two major components: system design and construction, and the development of a repeatable fabrication process with associated devices. To understand the genesis of the project, as well as the system design process, it is helpful to take a slight detour and revisit a previous project, the automation of optical testing for silicon on oxide waveguide structures.

- 1 – Nd:YAG @532 nm
- 2 – Focusing optics
- 3 – PDMS chip
- 4 – XYZ stages

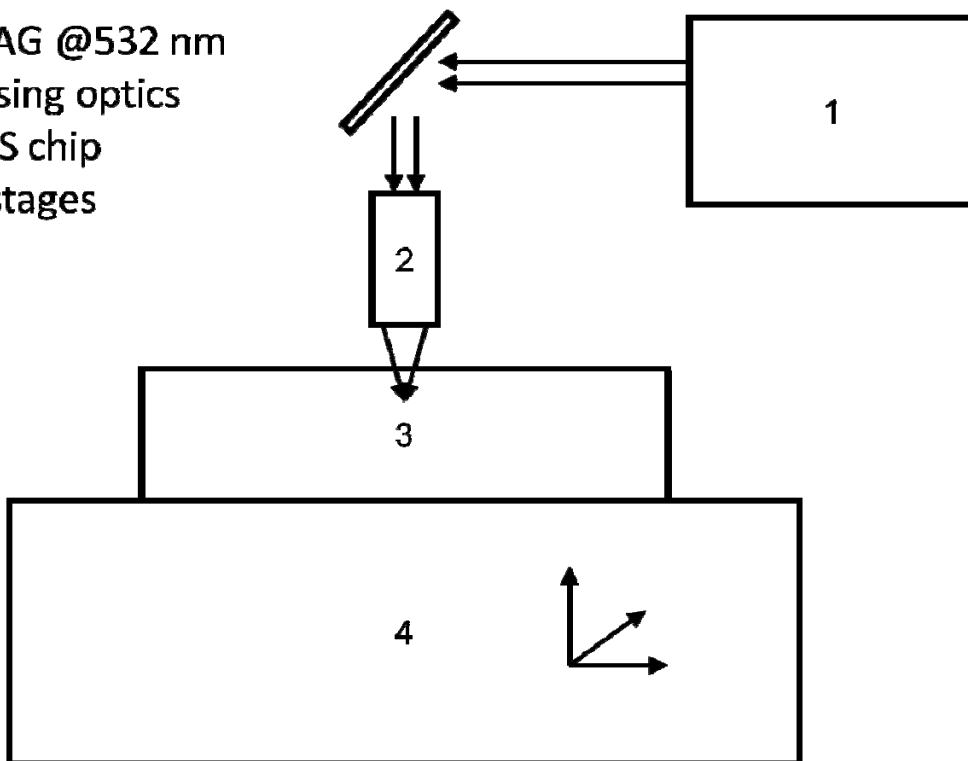


Figure 1: Schematic of volume laser ablation system. A pulsed laser (1) is focused through an optical system (2) into a block of PDMS (3). As the laser fires, a set of computer controlled stages (4) are driven in a path, resulting in ablated features cut into the block of PDMS.

Chapter 2

AUTOMATION OF OPTICAL TESTING

The first project I worked on after joining our group was the automation of optical testing for silicon on oxide waveguide structures. Silicon is an excellent choice for integrated optical systems as it is transparent at the dominant telecommunications wavelengths (near 1550nm), is a widely used material with highly developed processing techniques, and, with silicon dioxide as cladding, can be made into high index contrast waveguides. The high index contrast between silicon (3.5) and silicon dioxide (1.46) allows for tight confinement of the optical mode, and thus small features with tight bend radii.

Our waveguides were fabricated on silicon-on-insulator (SOI) wafers, had typical dimensions of 120 nm by 500 nm, and possesses optical modes that were well-confined to the waveguide and immediate cladding volume. Coupling light from these waveguides into commercially available testing equipment presents an alignment problem. Most telecommunication-wavelength test gear is coupled to single mode fiber; for this and for reasons of convenience, injecting and extracting light from the chip via optical fiber is desirable.

Traditionally, fibers are coupled to waveguides by either cleaving the waveguide, or dicing and polishing it, and then manually aligning a fiber to the edge of the waveguide. This immediately results in power loss from mode mismatch. Common optical fiber has an approximately Gaussian beam shape, with a $1/e^2$ radius of 5.2 μm . This is significantly larger than the mode size within

silicon waveguides. Furthermore, the fiber must be aligned precisely to the waveguide; accuracy of $2\ \mu\text{m}$ or greater is desirable.

For a simple two-port waveguide structure, edge alignment is a reasonable approach. The input fiber needs to be aligned in 5 dimensions (X, Y, Z; tip/tilt), but only the lateral directions result in significant loss with misalignment. If light can be captured from the output port with a large free space detector, it is straightforward to perform the alignment by optimizing the coupling efficiency. This can be performed manually; a skilled operator can perform an alignment of this nature in less than two minutes.

The alignment problem grows dramatically as the number of device ports is increased. If fibers are aligned one at a time, the total number of degrees of freedom of the alignment task will be $5m$ for a system with m fiber ports. In addition, with an edge-coupled approach, the total number of devices on a chip which are accessible to testing is limited by the linear dimension of the edge.

If light can be coupled out of the plane of the waveguide chip, and the degrees of freedom reduced, then alignment time can be cut, and large numbers of devices accessed for testing on a single chip. For SOI structures, the use of grating couplers[18, 19] accomplishes the first task. These are simple gratings etched into the waveguide layer of the chip, which are optimized to couple light from the waveguide to an out of plane free space mode which matches the guided mode of the optical fiber. For multiple fibers, the total degrees of alignment freedom may be reduced by using commercially available fiber arrays. These are typically glass or silicon blocks in which fibers are mounted in a linear array to micron accuracy. The output face is polished to a defined angle (typically 8 degrees) which minimizes backreflection from the fiber face. Performing an alignment from a fiber array to

an array of lithographically defined grating couplers on a chip now has 6 degrees of freedom – three translation axes, and rotation about those axes.

If we can build a system to mechanically constrain some of these degrees of freedom, and automatically align the others, we can align a chip to a fiber array automatically, and align specific devices within the chip automatically as well. This system was built with XY linear motor stage stack, $\theta\phi\psi$ manual stage stack, which carries the chip chuck, and a ballscrew driven Z stage, which carries the fiber array in a separate $\phi\psi$ stage. The X, Y, and Z stages are under computer control, and the X and Y stages can be driven rapidly (20 Hz) for small (100 micron) motions. The rotation and tip/tilt stages are required to control all degrees of freedom between the chip and fiber array. A detector and tunable laser, both under computer control, were used to inject and measure light from the devices. Together with the computer controlled stages, and custom software package, they allow automatic alignment of the chip along the X and Y axes.

Our goal is to be able to align a fiber array to an optical chip at an arbitrary location on the plane defined by the chip. Doing this requires controlling all of the degrees of freedom that exist between the chip and fiber array. One way to approach this is to consider that the chip and exit face of the fiber array both define planes in space. We need both planes to be coplanar, coincident, and aligned in rotation as well. This requires a total of 6 degrees of freedom. However, the system as designed in fact has 8 degrees of freedom for reasons we will now elaborate on.

If we just wanted to align a fiber array to a single device, we could theoretically bring the two into near alignment visually, search for an optical signal, and then complete the alignment procedure by using a 6 degree of freedom signal maximization procedure. There are a few techniques to a

perform this (the “hill climb” algorithm, for example), and, if we are fortunate enough to start off near the maximum, a maximization procedure should ensure that we reach the global maximum coupling position. However, this is a non-deterministic procedure, and doesn’t guarantee that we reach the maximum if the starting point is significantly off. A local maximum, for example, may trap the alignment before it reaches the global maximum. Also, since the error terms between axes are coupled, this is a slow technique. For example, a change in angle of the fiber array without parcentric rotation about its optical axis will result in a lateral shift as well, which will reduce the signal. A simple iterative hill climb approach, in which each degree of freedom is sequentially optimized can take many iterations to complete. While this is occurring, the alignment must be visually monitored as well to prevent mechanical interference between the fiber array and chip. Finally, once our alignment procedure is complete, we will have only aligned a single device to our fiber array. We want to align a chip to our fiber array so that we can easily probe multiple devices.

A different approach is deterministic alignment, or alignment to a standard. In this approach, we create a linear map in the X and Y axes between the coordinate system of the chip (chip coordinate frame), and the coordinate system of the stages (stage coordinate frame), and passively control the other degrees of freedom.

What such a map allows is deterministic placement of the fiber array relative to the chip coordinate frame. Once we know the location of the fiber array, we can place the fiber at an arbitrary point on the chip with high precision. A secondary alignment technique (hill climb, spiral mapping) in a reduced set of coordinates can then be used to optimize the coupling between the fiber and chip.

Stage to Chip Alignment

Both the chip and fiber were mechanically leveled to the stage axes with a dial indicator. This ensures that the chip, fiber array, and stage axes of motion are all parallel to each other to within 5 microns over a 5 mm range. This constrains the tip and tilt axes, and ensures constant vertical separation between chip and fiber array. The fiber array could now be lowered to within 10 microns of the chip; at this point 3 of the 6 degrees of freedom have been constrained.

The stage-chip map is generated by locating a set of on-chip fiducial devices, recording their positions in the stage coordinate frame, and then generating a linear fit based on the stage and chip coordinates. A set of simple devices were used as fiducial markers. These were two grating couplers connected to each other through a waveguide. A laser was connected to one fiber in the array, and a detector to the other; aligning the fiber array to the waveguide device closed the optical loop. The throughput optical signal could thus be used to verify alignment; at this time, the relative rotation of the chip and fiber array were manually adjusted to maximize coupling. Fiducials were located in easily recognizable blocks (arrays), typically a 3 by 3 array on each corner of the chip. Once the fiber array was placed above the chip, a spiral mapping technique was used to find the rough location of these arrays. The fiber array could be located next to visible on-chip fiducials to an accuracy of about 50 μm visually (through a camera system); the spiral mapping generated a throughput intensity map of the coupler locations. Usually, scanning a 100 by 100 micron square grid at a resolution of a few microns sufficed to give a reasonable map of one of these grating coupler fiducial arrays.

Once an array had been located, high accuracy location of the grating coupler-waveguide devices was performed via iterative spiral mapping. The chip was moved to align the fiber array to one of the devices at the corner of the alignment array, and the positions recorded. Once this process had been repeated for at least 3 non-collinear points (typically a much larger set), a linear map between the stage and chip coordinate frames could be established.

At this point, the system could now be driven under computer control to a known device location, with an accuracy that would typically guarantee first light, and a fine alignment spiral alignment could be performed. A software control package was written to automate this process, so that once a chip was aligned to the system, the system would automatically iterate through all devices on the chip, align to them, take a spectrum with the tunable laser, and save the data to a file.

Testing Results

This is an incredibly powerful tool. Alignments of devices with many ports now take as long as alignments of two port devices. With the automatic alignment to devices on a chip, the time an operator needs to spend setting up an experiment is invariant with the number of devices tested. Typically, setting up the chip alignment in the system took 30 minutes. The system could then be allowed to run continuously, for days in some cases, gathering data on hundreds, or even thousands of devices on a single chip.

With this system, a number of silicon waveguide and photonic integrated circuit structures were tested. These included ring resonators[20], resonators based on slotted waveguides[21], segmented waveguide structures (which can be easily connected to electrical channels)[22], and SOI waveguides coupled to metal plasmonic structures[23]. Automated testing enables research on

devices which are difficult to fabricate, or devices with a low probability of functioning. In the case of the plasmonic waveguides, approximately 5,000 devices were tested before a single working device was located. With automation, this is a total of 7 days of continuous testing. Without automation, this would have required about two months of manual testing. This project would be impractical were automated testing not available.

Building this system also resulted in expertise in precision alignment, optical system design, and automation control. Microfluidic structures have significantly lower precision (tens of microns) than SOI integrated waveguides; they are typically fabricated via soft lithography techniques. Building a quasi-automated tool to modify and fabricate bespoke microfluidic structures came as a natural next step.

Chapter 3

ABLATION SYSTEM DESIGN

The goal of this project was to develop a laser ablation process and fabricate novel devices, and in the process build a robust, flexible instrument useful to the research group as a whole. The design process was driven by this goal, and the hardware choices reflect this. The basic goal of the system is volume laser ablation within PDMS with an inexpensive flashlamp-pumped Nd:YAG laser, but other projects were considered during the design phase as well.

Perhaps the most ambitious of these other projects was fabricating features by two-photon three-dimensional photopolymerization. Features fabricated by this technique have achieved length scales under $1/7$ of the wavelength[24]. This goal pushed the lateral stage resolution requirement down to the range of tens of nm. Optical fabrication by vector scanning also requires backlash-free stage motion. Acquiring a higher power, higher pulse rate laser in the future for volume laser ablation would require fast stage movement; high energy, regeneratively pumped ultrafast lasers have repetition rates up to 5 kHz, which requires a stage system capable of 50 mm/s movement rates for 10 μm pulse spacing. Finally, since chips fabricated by the more conventional techniques at Caltech's KNI Microfluidics Foundry may be up to two inches across with typical feature sizes of 100 μm , modification of conventional structures by laser ablation sets the translation requirement to 50 mm x 50 mm, with an absolute accuracy of 50 μm . Also, the optical system would need to be extremely flexible – capable of being altered to handle different wavelengths and focal conditions. These rough stage requirements are summarized in the following table:

Stage Property	Requirement
Lateral Translation	50 mm
Vertical Translation	5 mm
Lateral Resolution	50 nm
Vertical Resolution	150 nm
Lateral Velocity	50 mm/s
Dynamic/Tracking Errors	10 μm
Backlash	50 nm
Accuracy	50 μm

The range of motion requirements rule out short-throw piezoelectric stages; the precision, speed, and low backlash motion requirements rule out stepper motor/ballscrew stages. The optical system constraints indicated against a microscope-based system. These design requirements led to choosing a stacked linear drive stage system (Figure 1), mounted under a large platen on which arbitrary optical systems could be implemented.

Stage Error Budget

When building a precision system, error budgeting is critical to success. In this case, we want to be able to translate the ablation point through the full range of stage motion with a point-to-point vectorial error less than 50 μm . Laser ablation inside of a transparent material has two sources of placement error. The first is the index variability of the material. If a beam focuses a depth z inside a material with an index of refraction n , then the total optical length traversed by the beam will be nz . A small change in index δn will translate into a placement error of $z\delta n$. If this is due to local variability of the index, the placement error reflects the index variability, and can only be removed by the system by first mapping the index variation, and then correcting the beam placement. If the

entire block of material has a uniform shift in index, then this height error is easily removed by a linear fit. In practice, uniformity of index was assured by using long (5 minutes) mixing times for the PDMS; uniform index errors were automatically removed by alignment routines in the control software.

The second source of placement error is the stage-to-optics positioning. This is composed of both static errors in the stages, dynamic errors caused by stage tracking / flexibility in the optical mounting systems, and surface error in the chip itself. Static errors are due to linear inaccuracy in the stage motion, misalignment of the stage axes, and angle induced error. Linear accuracy is an inherent property of the stage mechanics and feedback system. Misalignment of the axes creates coupling between stage motions. If, for example, the X and Y stages are misaligned by an angle θ from the normal, then a motion d along one axis will cause a placement error of $d \sin(\theta)$ along the normal axis. This is a systemic error, and was removed via the control software.

As a stage moves, it tends to wobble slightly about the axes parallel and normal to its motion. These slight changes in angle are referred to as pitch, roll, and yaw (Figure 2). At a point above the stage, they induce position errors of the form:

$$\Delta\vec{x} = \mathbf{R}\vec{s}$$

Here, \vec{s} is the moment arm from the center of stage motion to the desired point on the chip, and \mathbf{R} is a rotation matrix. Since the angular errors are very small, only the first order rotation terms need be considered. For each of the angles and moment arms, this gives:

$$\Delta x_i = \sum_{i \neq j \neq k} \theta_j s_k$$

The stages selected were Aerotech ALS25010 linear drive stages for the X and Y axes, and an Aerotech AVS125 for the Z axis. The ALS25010 stages have a travel of 100 mm, an accuracy of 1 μm , resolution of 20 nm, and nominal pitch/yaw errors of 5 arc seconds. The AVS125 has a travel of 25 mm, resolution of 106 nm, accuracy of 1 μm , and nominal pitch/yaw errors of 10 arc seconds. When stacked, and combined with other mounting hardware, there are substantial moment arms from the stage axes to the chip. This leads to the following table for the nominal X and Y-axis errors:

Axis	Maximum Moment Arm (mm)	Angular Error (μrad)	Single Axis Error (μm)	Total Error (μm)
X	323	24.2	7.8	11
Y	205	24.2	4.9	6.9
Z	70	48.4	3.3	4.6

These are just the dominant terms for wobble induced error; together they sum to 22.5 μm . When combined with the linear errors, they add to 25.5 μm . This is nearly half of the error budget for the system. Aerotech aligned and tested the stage block at their factory with an interferometer system, and were able to verify that it maintained an accuracy of 10 μm at the surface of the top stage over the full range of stage motion (100 mm x 100 mm x 25 mm). The moment arm from this point to the chip is 135 mm; the moment arm from the top of the X stage to the top of the Z stage is 187 mm. If the wobble-induced error is the dominant source, scaling suggests that the error at the chip will be less than 17 μm .

Dynamic accuracy errors are caused by stage tracking errors and backlash, and soft coupling between the stages and system optics. Stage backlash is the dead band that occurs when changing the direction of motion of a stage axis (Figure 3). In screw-driven stages, this is caused by mechanical play between the screw and nut. It can be mitigated through drive software by always approaching the target point from the same direction. This may require overshooting the target point, changing direction, and then backing up to the target point. For a system required to smoothly change direction over a three dimensional contour, this is not acceptable.

Linear motors, however, do not have a mechanical drive system. They use a U-shaped magnetic channel system to directly generate force, and thus do not suffer from backlash. The selected stages use linear motors to drive the stage, combined with glass scale encoders to generate position feedback; they are backlash-free.

Tracking accuracy is the ability of a stage system to follow a given vectorial path while maintaining a specific velocity profile. Driving an XY pair of stages in a circle at fixed velocity, for example, requires that they accelerate continuously. In our case, structures such as ablated corners require high accuracy, and thus high stage acceleration. We specified that the stages be able to accelerate at 0.79 m/s^2 while maintaining an accuracy of $10 \text{ }\mu\text{m}$; this means the stages can accelerate around a $50 \text{ }\mu\text{m}$ radius corner at 6 mm/s .

Combining the static and dynamic errors gives a lateral nominal error of $27 \text{ }\mu\text{m}$, just slightly over half the maximum allowed; this leaves $23 \text{ }\mu\text{m}$ of lateral error budget for the PDMS chip, mounting, and optical system.

Chip Mounting and Fabrication Error

In order to ensure that the chip face is parallel to the axes of motion of the XY stage, a small manual tip/tilt stage is mounted on top of the automated XYZ stage block. On this was mounted a custom vacuum chuck which holds the chip. The chuck was fabricated out of stainless steel, and lapped; when tested with a dial indicator, it was flat to within 5 microns across the bulk of its face, with slightly larger errors near machined features (bolt reliefs, vacuum holes, etc). By translating the stages while measuring the top face of the chuck with a dial indicator, the wedge angle between the top surface of the chuck and the plane defined by the XY stages can be measured. The Newport 37 tip/tilt stage was then adjusted to remove this wedge error. The chuck surface can thus be made flat and parallel to the stage axes to within the flatness of the chuck – 5 μm .

In addition to the stages, error in the PDMS chip must also be considered. As mentioned previously, local variability in the index of refraction can result in an error in position in the focal point. The surfaces of the chip must also be accurately fabricated. For bulk samples of PDMS, this was accomplished by molding a rectangular block in a kinematically constrained mold. A kinematically constrained mechanical system is one in which only the minimum required degrees of freedom are controlled. This eliminates unnecessary stress within the system, and tends to make it more stable under externally applied stress (as occurs during temperature cycling, for example).

The mold is designed to cast a 2.75x2.75x0.5 inch block of PDMS, with the large faces flat and parallel to within 10 microns. This is accomplished by constraining two lapped stainless steel plates with a set of 3 hardened chrome steel gauge balls. An aluminum ring mold – not under mechanical stress – lies within the stainless plates, and forms a cavity into which the liquid

monomer is poured. The top plate has a relief recess for the aluminum ring. Once the lower mold is filled with PDMS monomer, the top plate is lowered into place and then spring loaded for the curing process. The mold is then forced open with bolts, and the PDMS chip is extracted. This process works surprisingly well – the resulting PDMS blocks are typically flat to within 15 μm across the range of the molded surface. Figure 4 shows the mold in both open and closed configurations.

For chips which have been manufactured by standard soft lithographic techniques, the top and bottom faces will not necessarily be parallel. Such wedge errors can be significant – 0.5 mm is not uncommon. However, being molded on a silicon wafer, the channel side of such a chip will typically be flat to within 10-20 μm . The wedge error can be removed from the system once the chip is in place by manipulating the Newport 37 tip/tilt stage; again, this allows the top surface of the PDMS chip to be leveled to the 10-15 μm range.

The molding and mounting of the PDMS chips thus contributes between 15 and 20 μm of vertical error to the system. These errors are orthogonal to the 27 μm of lateral errors obtained from the stage system, resulting in a total vectorial displacement error about 31 μm to 34 μm . This lies within the error budget of a 50 μm vectorial displacement.

The system mechanical specifications are thus:

Stage Property	Required	Implemented
Lateral Translation	50 mm	100 mm
Vertical Translation	5 mm	25 mm
Lateral Resolution	50 nm	50 nm
Vertical Resolution	150 nm	53 nm
Lateral Velocity	50 mm/s	1 m/s
Dynamic / Tracking Errors	Unknown	10 μm at 0.8 m/s^2
Backlash	50 nm	0
Dynamic and Static Accuracy	50 μm	34 μm

Stage and Platen Hardware

The stage stack described in the error budget section was mounted on a granite block on a small optical table, and combined with a mechanical tip/tilt stage (Newport 37). A computer-aided design (CAD) model of the complete stage system and mounting platen was built; this facilitated the design of custom mounts and adapters; Figure 5 shows the model and stage hardware. The system was mounted on a small dedicated optical table. Since the stages can undergo hard acceleration, and the table was in a fairly quiet environment, the optical table was not floated; this helps damp acceleration-induced vibration in the system. The platen is a solid half-inch thick aluminum plate, which is mounted on a cage of extruded aluminum channel obtained from McMaster Carr.

Laser

The laser used was a Continuum Minilite I flashlamp-pumped Nd:YAG. This system is composed of a small laser head containing the laser and optical hardware, and a separate unit containing the

drive electronics and water cooling supply. Q-switching is controlled by an electrically triggered Pockels cell; at the native wavelength of 1064 nm, pulse length falls in the 5-7 ns range. Output power is controlled by a rotatable cross polarization filter, mounted outside the laser cavity. An internally mounted doubler crystal shifts the wavelength to 532 nm, and reduces the pulse length to 3-5 ns. With a new flashlamp, and careful tuning, output energies of up to 12 mJ / pulse at 532 nm were reliably obtained. The output beam is roughly Gaussian, with a diameter of 3 mm.

Optomechanics and Optical Alignment

The laser head was mounted on a small plate mounted normal to the main platen; all other optical elements were mounted on a separate plate normal to the main platen (Figure 6). The optical system is composed of the collimating and focusing block discussed in the previous section, coupled to the laser. A small adjustable tip/tilt fold mirror was used to couple the laser into the focusing section. This mirror sets the optical axis of the system. To ensure a coma-free focus, all of the elements in the beam train must be laterally aligned to the optical axis.

The optical axis was set normal to the stage axes as follows. First, the vacuum chuck on the stages was mechanically aligned to the stage axes. A mirrored optical flat was then placed on the chuck. The laser was fired at the mirror on the chuck, and the fold mirror adjusted so that the reflected beam was nearly coincident with the output port of the laser. With a loop path length of about 750 mm, and a return beam offset of 5 mm, this results in an error relative to stage normal less than 0.5 degrees. For focusing systems using achromats or microscope objectives, off the shelf

optomechanics were used. The beam line was assembled element by element, with care taken to center each lens along the optical axis.

Systems based on fast aspheric condenser lenses used a custom machined optomechanical mounting set (Figure 7). This mounting system is composed of an aluminum base with a large, precision-cut channel. Rectangular aluminum mounts were machined which keyed into this channel; a mounted lens could thus be translated along the base without lateral motion or wobble. These mounts were designed to mate with annular aluminum lens mounts, into which lenses were glued with about 75 μm of lateral error. The completed system allows lenses to be swapped into the system without performing lateral alignment. In addition to the annular lens mounts, aluminum disks with centered pinholes were fabricated as alignment tools. When these are loaded into the system in lieu of lenses, only a laser beam parallel and coincident with the optical axis of the system may pass through. The system can thus be aligned to the optical axis by maximizing through power; when lenses are swapped in for the pinholes, they are automatically in alignment.

Hardware Control

The goal of this system is to perform ablation in a quasi-automated fashion. Once a chip has been mounted, and aligned, we want to load a geometry file – a set of instructions defining structures – and have the system execute them autonomously. This is realized through computer control. A top level program, written in LabView, is used to generate a set of GCode commands. These are piped to a real time software layer, which in turn interfaces with the stage controller. This control unit in turn drives the stages and laser (Figure 8).

Stage motion is directed by a real time software layer that runs on the main control computer. This program runs directly on the CPU – underneath the operating system – and is thus lag-free. The real time software layer accepts commands in a modified version of GCode, a common CNC machining language. The version used by the real time software program is extended to include position sensing, triggering, and auxiliary (PID loop control, etc) commands. This software layer executes GCode commands synchronously with stage motion.

The control computer is connected to a stage controller via Firewire. This controller contains the drive amplifiers for each stage axis, the stage PID feedback loop hardware, and a variety of TTL logic and analog outputs. It also contains internal, software-settable hardware that can trigger these outputs in real time based on stage position. All controller functions can be controlled through the real time software layer.

The laser flashlamp and Q-switch can be triggered either internally or through 5V TTL inputs. The flashlamp TTL trigger was wired to one of the TTL output ports on the stage controller; the Q-switch was set to automatically trigger after the flashlamp.

The hardware is thus capable of taking a set of GCode instructions for stage motion and laser firing points and executing them in a real time, synchronous fashion. The final task required to control the system is generating the driving GCode.

Alignment Software

There are a wide variety of computer aided machining (CAM) software packages commercially available. CAM programs can take a design file from a CAD program and convert it into GCode.

Some of these programs can perform offset alignment (a fixed vectorial offset) and integrate cutter (laser) control information in their output. In our application, however, we required much more control over both the laser fire timing and alignment.

The simplest laser firing control technique sets the laser to trigger at a fixed frequency; with the stages moving at a fixed velocity, this results in laser pulses which are evenly spaced in distance. Real world stages, however, do not move at fixed velocities when generating any feature more complicated than an infinite line. At a corner, for example, the stage must simultaneously decelerate along one axis while accelerating along another. Our stages are excellent at this, and can in fact maintain a constant vectorial velocity along smooth contours (subject to stage acceleration limits). Yet, at sharp corners and endpoints, acceleration is unavoidable. A laser firing at fixed frequency combined with stage motion of variable velocity results in unevenly spaced voxels. To ensure evenly spaced voxels, the stages are equipped with a position synchronized output (PSO) controller. This is an embedded controller which dynamically captures the real stage position, and then triggers an output (wired to the laser) at specified vectorial distances. With this approach, pulses can be evenly distributed even with variable stage velocity. Enabling and controlling the PSO functionality required additional commands, integrated into the geometry GCode, which cannot be produced by CAM programs.

Alignment of the optical/stage system to the chip requires altering the GCode appropriately. When a chip is mounted on the chuck, its position and index of refraction define a three axis coordinate system. This coordinate system is not coincident with that defined by the stage axes. In the case where a blank piece of PDMS is going to be ablated, this doesn't really matter; once ablation

begins, the stages impose their coordinate system on the chip; as long as it isn't moved relative to the mounting chuck, features on the chip will be aligned relative to each other.

Chips with an existing pattern – such as those produced through soft lithography – possess their own coordinate frame, which must be reconciled with the stage coordinate frame. In addition, neither coordinate frame is consistently scaled or orthonormal. There are a variety of error sources in both frames. The stages have a slight amount of skew – angular misalignment from normal – which translates into lateral errors under axis motion. PDMS chips are subject to shrinkage; this means that the features as realized on the physical chip will be slightly closer spaced than those specified in the chip design file. This shrinkage can be compensated for somewhat during chip design, but it takes only a small variability in shrinkage to result in critical errors in alignment. For a 50 mm wide chip, a shrinkage error of 0.1% results in a cumulative position error of 50 μm across the chip. When combined with the stage and optical positioning error budget, this makes alignment to 100 μm features rather a hit-or-miss proposition. In addition to shrinkage, the chip will be laterally rotated relative to the stage coordinate frame. Finally, vertical motion needs to be scaled by the index of refraction of the PDMS – which is not well controlled.

Fortunately, all of these errors are linear in nature. This means that we may relate a stage frame coordinate to a chip frame coordinate as follows:

$$\vec{x}_s = \mathbf{M}\vec{x}_c + \vec{s}$$

or

$$x_{si} = \sum_{j=1}^3 m_{ij}x_{cj} + s_i$$

Here, \vec{x}_s is a stage frame vector, \vec{x}_c a chip frame vector, \vec{s} a vectorial offset, and M the matrix which embodies the assorted rotation, skew, and scaling coefficients. Combining the matrix and offset vector elements gives a total of twelve constants which must be determined to map the stage and chip coordinate frames. In practice, this is accomplished by adding fiducials to PDMS chips. By iteratively firing the laser and moving the stages, while observing the ablation point, the stage/laser system can be aligned to a fiducial. The stage coordinates are then recorded; this process is then repeated for at least 4 fiducials. Once this is accomplished, we have a set of chip and stage frame coordinates which correspond to each other. Performing a linear fit between these two data sets then generates coefficients for the above linear map. This linear map can then be applied during the software conversion from a CAD design file to GCode, resulting in a GCode file that is aligned to the chip coordinate frame.

Commercially available CAM software exists which can perform offset and rotation alignments. In this case, however, we require the ability to map between two essentially arbitrarily related coordinate frames. It is theoretically possible to take a GCode file generated by a CAM package, extract all of the stage motion commands, map them to aligned locations, insert laser control code, and repackage this into a control file. When combined with the need to perform the manual, iterative alignment technique, and need to perform other functions (system initialization, etc) through software, using a standalone CAM package as part of this process becomes cumbersome. A decision was made to integrate geometry generation and alignment mapping into custom software for overall system control. While requiring more initial effort, this results in a more user

friendly final system – one which can also be modified to suit changing hardware or process requirements.

Control Software

A system level control program was written in LabView. In addition to the automated stage control and alignment portions, it includes system housekeeping functions, and allows the user to manually control the laser and stages. Using LabView as a development system encourages good software practices; all functional elements were designed to be as modular as possible.

An intermediate geometry control language was created to function as an input to this control program. This is a simple, human-readable language which contains a small set of commands for controlling the laser and stages. A separate compiler was written which can parse AutoCad files into this format. The benefit of using this approach is that test files may be easily written or modified by hand, and stored in text files. This also allows complex geometrical structures, or patterns of structures with variable parameters to be easily defined by scripting. For example, one of the most common test patterns used was a set of channels ablated at continuous pulse power, but with pulse spacing swept across the set of channels. Constructing GCode for such a structure by laying out a design in a CAD program, and then altering the resulting GCode to vary the pulse spacing would be tedious. Using an intermediate language which is easily scripted makes this a fairly trivial exercise. More complicated structures, such as valves, would later be generated by scripting in this intermediate language as well. An example of a control file written in the geometry language and its associated compiled output are attached at the end of this chapter.

The control software contains a compiler which translates the intermediate language into GCode. Once the alignment process has been performed, and a linear map generated, this compiler applies the linear map to the geometry definitions as it compiles them into GCode. After this has been completed, the resulting GCode is piped directly to the real time stage controller. From this point onwards, the process is fully automated, and the user can leave the system unattended.

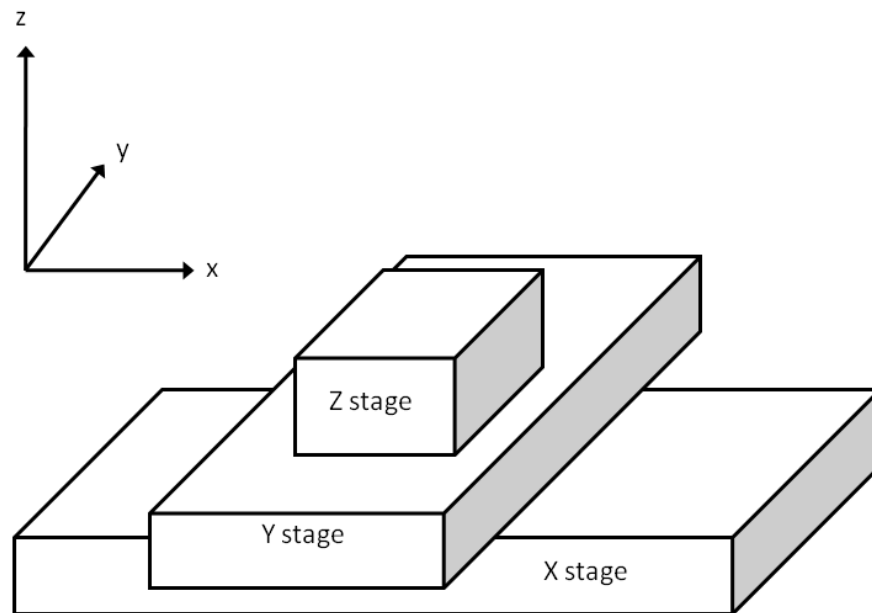


Figure 1: Computer driven stage stack and directions of motion.

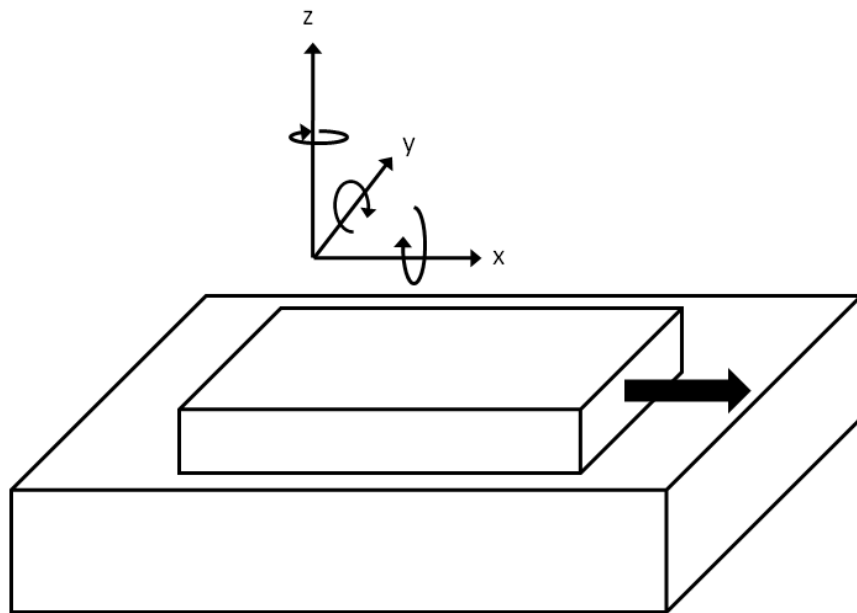


Figure 2: Angular error caused by stage motion; during translation, the stage wobbles, inducing pitch, roll, and yaw errors, shown here about the ordinal axes.

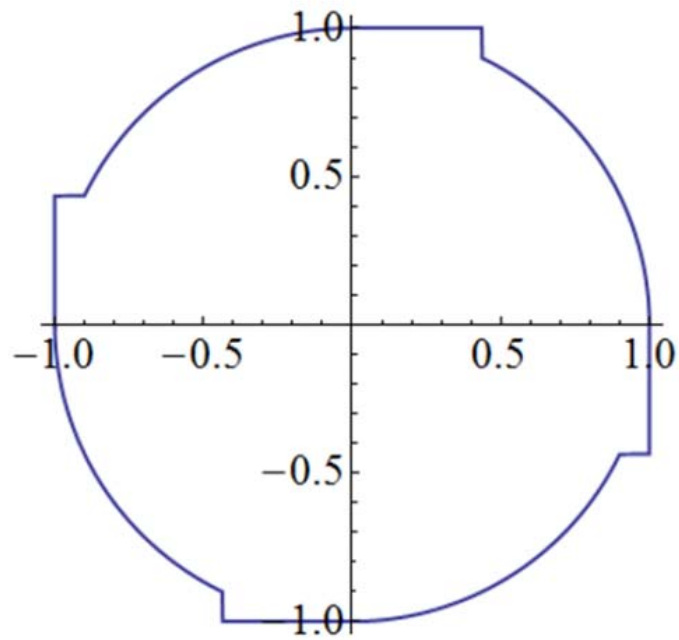


Figure 3: Backlash. This is a simulation of stage motion containing backlash. The X and Y axes are driven a sinusoidal motion; backlash appears as a stuttering motion at each stage extremum. The simulated backlash is one tenth of the radius of motion.

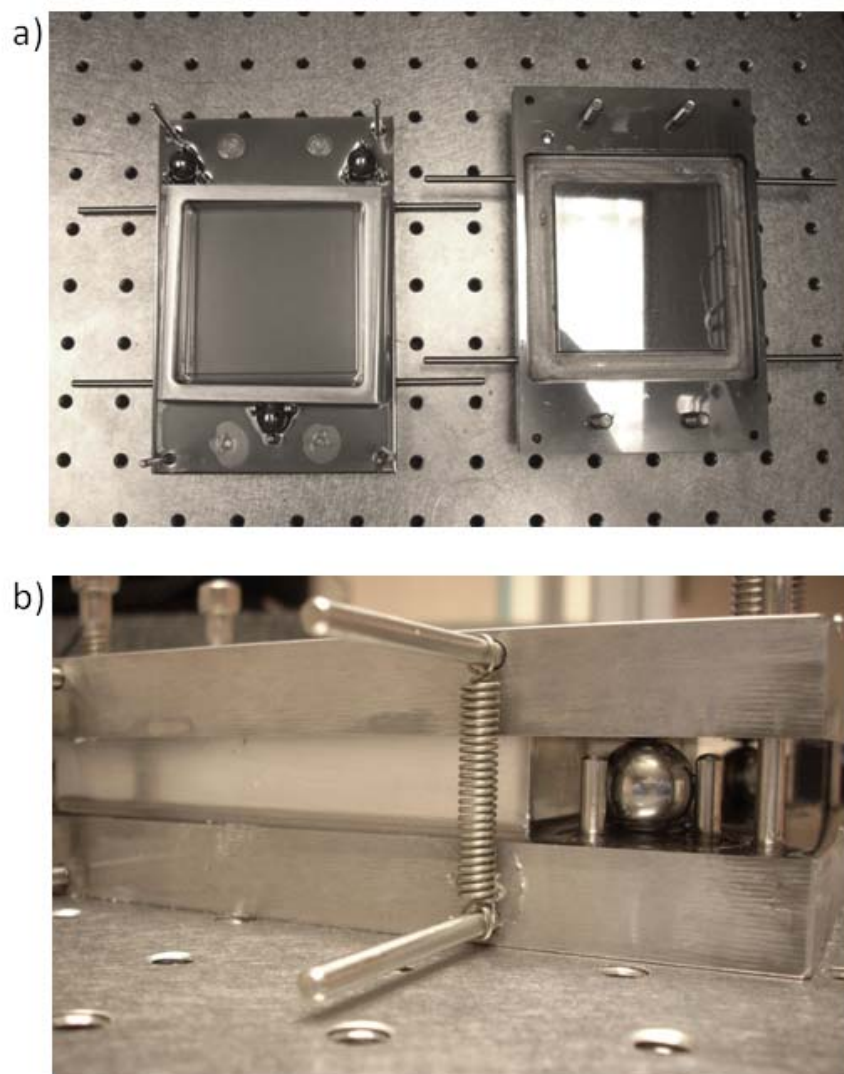


Figure 4: Precision stainless steel mold used to fabricate blank PDMS chips shown opened with cured PDMS (4a) and in the closed, spring loaded state used for curing (4b).

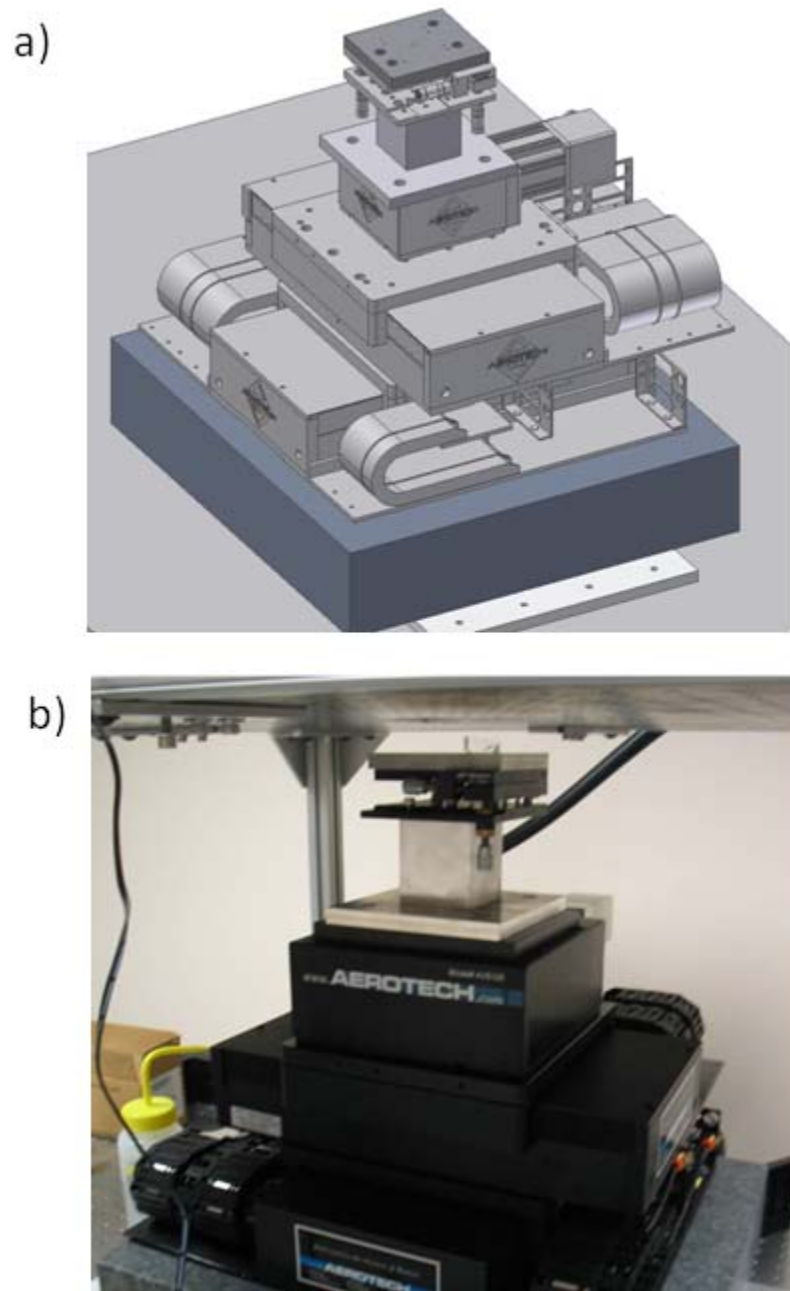


Figure 5: Figure 5a shows a CAD model of the Aerotech stages, granite mounting base, Newport tip/tilt stage, and other mounting hardware. Figure 5b shows the stage system as implemented.

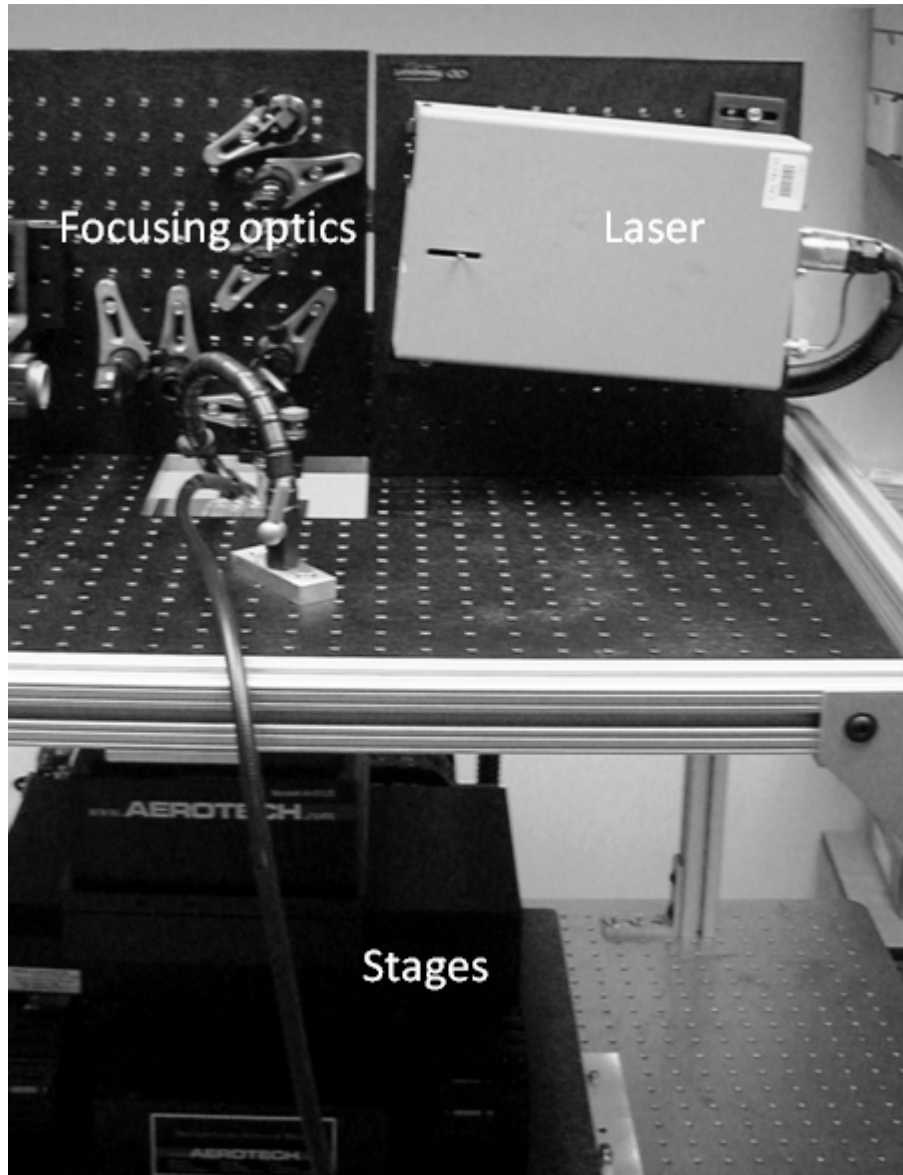


Figure 6: Isometric view of the completed system, showing the laser, stages, a set of focusing optics, and mounting platens.

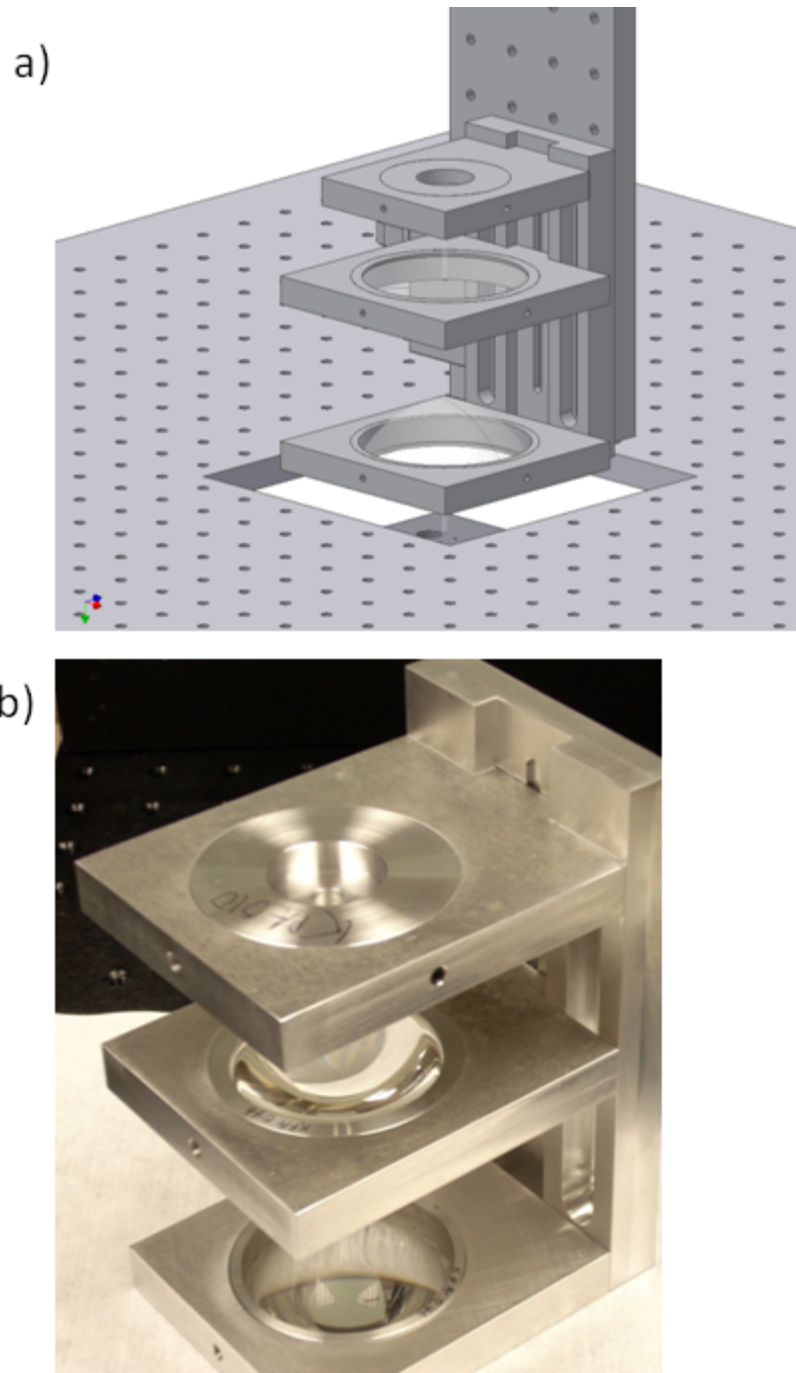


Figure 7: A custom machined mechanical set for aspheric lens-based focusing systems is shown as a CAD model (7a) and as realized (7b).

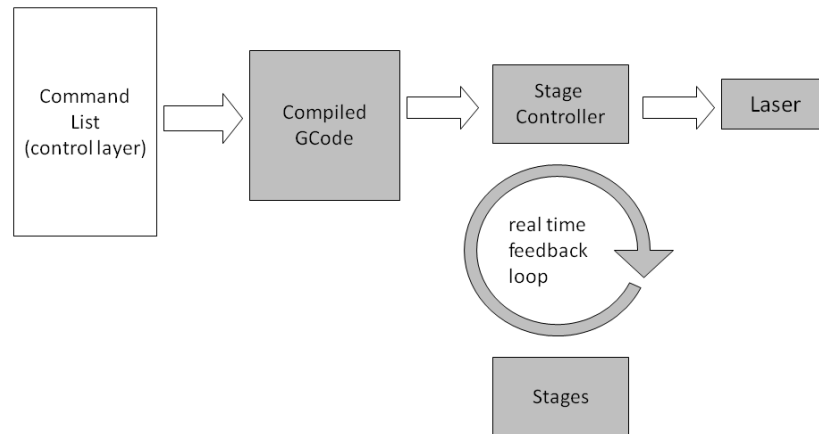


Figure 8: Command flow for the control system. Commands are compiled into CNC GCode, and directed to the stage controller. This in turn drives the laser through a TTL link, and drives the stages via a real time PID feedback loop.

Example of a geometry control file:

```
//This is a square and 4 alignment rings designed as a
//demonstration of alignment capability

// set laser frequency and pulse spacing
laser freq 10
pso 0.005

//move to start

laser off
velocity 1
coord -.5 -.5 5

// write the square

velocity 0.5
laser arm
dwell 0.1
coord -.5 -.5 5
coord -.5 .5 5
coord .5 .5 5
coord .5 -.5 5
coord -.5 -.5 5
laser off

// alignment rings
// 0.5 mm diameter rings on a 3 mm square

coord -3.25 -3 5
laser arm
GRing -3.25 -3 5 -3 -3 5
laser off

coord -3.25 3 5
laser arm
GRing -3.25 3 5 -3 3 5
laser off

coord 2.75 3 5
laser arm
GRing 2.75 3 5 3 3 5
laser off

coord 2.75 -3 5
laser arm
GRing 2.75 -3 5 3 -3 5
```

Example of the GCode compiled from the above control
file in a shifted, rotated coordinate system:

```
PSOPULSE X TIME 100000.000000 1000.000000
PSODISTANCE X FIXED 0.001000 UNITS
PSOCONTROL X OFF
F1.000000
LINEAR X9.420772 Y9.594420 Z6.000000
F0.500000
PSOCONTROL X ARM
DWELL 0.100000
LINEAR X9.420772 Y9.594420 Z6.000000
LINEAR X9.594420 Y10.579228 Z6.000000
LINEAR X10.579228 Y10.405580 Z6.000000
LINEAR X10.405580 Y9.420772 Z6.000000
LINEAR X9.420772 Y9.594420 Z6.000000
PSOCONTROL X OFF
LINEAR X6.278430 Y7.609933 Z6.000000
PSOCONTROL X ARM
LINEAR X6.278430 Y7.609933 Z6.000000
CW X6.278430 Y7.609933 I0.246202 J-0.043412

PSOCONTROL X OFF
LINEAR X7.320319 Y13.518780 Z6.000000
PSOCONTROL X ARM
LINEAR X7.320319 Y13.518780 Z6.000000
CW X7.320319 Y13.518780 I0.246202 J-0.043412

PSOCONTROL X OFF
LINEAR X13.229166 Y12.476891 Z6.000000
PSOCONTROL X ARM
LINEAR X13.229166 Y12.476891 Z6.000000
CW X13.229166 Y12.476891 I0.246202 J-0.043412

PSOCONTROL X OFF
LINEAR X12.187277 Y6.568044 Z6.000000
PSOCONTROL X ARM
LINEAR X12.187277 Y6.568044 Z6.000000
CW X12.187277 Y6.568044 I0.246202 J-0.043412

PSOCONTROL X OFF
```

Chapter 4

ABLATION OPTICS DESIGN

To obtain a controlled ablated volume, the incoming laser beam must be tightly focused into the PDMS. The output beam size from the laser is roughly 3 mm in diameter, so it must be expanded, collimated, and then refocused into the bulk material. The basic system to perform this was composed of a small lens to expand the beam, followed by a large positive lens, which collimates it, and completed by a positive lens to focus the beam (Figure 1).

Due to the potentially high pulse powers used, minimizing the complexity and number of elements in the optical path is essential for reliability. For example, the expanding lens, which sees the highest pulse fluence in the system, was typically a BK7 singlet lens. Initial attempts to use a small achromat for the expander quickly resulted in fractured lenses; a later attempt to increase the expansion angle by cascading two negative BK7 lenses also resulted in fractured lenses if care was not taken to ensure that the ghost focus of the second singlet was outside the body of the initial lens.

Resolution

We want to deliver a spatially confined pulse to a point embedded in the PDMS. Lateral resolution is determined by the convergence, or speed, of the final focusing lens. For a thin lens focusing a collimated beam down to a spot (Figure 2), resolution can be estimated using the Airy criterion for spot size[25]:

$$(1) \quad \delta x = 1.22 \frac{f\lambda}{D}$$

Here, δx is the lateral dimension of the spot, f the focal length of the lens, and D the diameter of the collimated beam impinging on the focusing lens (Figure 2). This can also be rewritten in terms of the numerical aperture (NA) of the system, which for a beam half-angle θ is defined as:

$$NA = n \sin \theta$$

Rewriting in the resolution in terms of the NA yields:

$$NA = n \sin \left(\tan^{-1} \left(\frac{D}{2f} \right) \right)$$

$$(2) \quad \delta x = 1.22 \frac{f\lambda}{2 \tan \left(\sin^{-1} \left(\frac{NA}{n} \right) \right)} \approx \frac{0.61\lambda}{NA}$$

Increasing the convergence of the beam yields a smaller spot size, at the expense of working distance, or of beam diameter for a fixed working distance.

An alternate approach to determining resolution uses the Gaussian beam model. The Gaussian model is a natural choice for free space optics as it describes both far and near field beam behavior for slowly converging fields. It is also straightforward to manipulate mathematically, and can be used in conjunction with the ABCD propagation technique to model lens systems[26, 27]. A Gaussian beam is defined as:

$$E(r, z) = \frac{E_0 w_0}{w(z)} \exp \left\{ -i[kz - \eta(z)] - \frac{r^2}{w^2(z)} - \frac{ikr^2}{2R(z)} \right\}$$

$$k = \frac{2\pi n}{\lambda}$$

$$z_0 = \frac{\pi n w_0^2}{\lambda}$$

$$w^2(z) = w_0^2 \left(1 + \frac{z^2}{z_0^2} \right)$$

$$\eta(z) = \tan^{-1} \left(\frac{z}{z_0} \right)$$

$$\theta = \tan^{-1} \left(\frac{\lambda}{\pi n w_0} \right) \approx \frac{\lambda}{\pi n w_0}$$

$$R(z) = z \left(1 + \frac{z_0^2}{z^2} \right)$$

Here, w_0 is the radius of the beam at the waist, k is the wavenumber, and θ is half the far field divergence angle.

The Gaussian beam waist may be related to the numerical aperture by:

$$(3) \quad w_0 = \frac{\lambda}{\pi n \tan\left(\sin^{-1}\left(\frac{NA}{n}\right)\right)} \approx \frac{\lambda}{\pi NA}$$

Both the Airy and Gaussian models dictate a highly convergent beam for minimal spot size. For a given lens size – corresponding to a collimated beam diameter – there is an inverse relationship between working distance and resolution. The vertical motion stage has a 25 mm range of motion; to fully utilize this range, while maintaining a small spot size, requires a large, fast, final focusing optic. The additional constraints of minimizing component count, cost, and system complexity led to a simple three-element system of discrete lenses. Microscope objectives, which can deliver very small spot sizes, were initially ruled out as focusing elements. Inexpensive objectives typically have short working distances (well under 1 mm), and are not designed to handle high pulse energies. Long working distance objectives, such as the ones produced by Mitutoyo, were deemed too expensive to use in a system where they could easily be destroyed by high pulse energies.

Design Approach

Initial design studies used Zemax to perform raytracing and Gaussian beam modeling, and used the Newport PAC achromat lenses as elements. A variety of achromat-based systems were modeled; the prime metrics being a tight spot diagram (minimal lateral ray aberration), small Gaussian spot

size, and simplicity. Systems using large molded aspheric condenser lenses were modeled in Code V and LightTools (Optical Research Associates). Raytracing analysis of the aspheric systems proved fruitless due to the difficulty of obtaining accurate lens prescriptions – the set of coefficients which define the lens surface - from the manufacturer. Also note that these are inexpensive molded aspheres, designed for illumination rather than imaging applications. High precision aspheres, fabricated either via molding or diamond CNC machining do exist, but at high cost.

Of the achromat-based approaches, the system which emerged as the best candidate from this process was composed of a 6.35 mm Newport KBC 013 negative lens with a focal length of -6.3 mm, followed by a pair of 25.4 mm Newport PAC 040 doublet achromats, each with 50.8 mm focal lengths, as the collimator and focusing lenses. The achromats are diffraction limited at 514.5 nm, and should be nearly as aberration-free at 532 nm. An ABCD analysis of this system follows.

First, we place the waist of the incoming laser beam at the input of the negative expansion lens. This is not the true location of the waist, which is actually located in the laser cavity; it is, however, a good approximation, since the laser beam is only slowly divergent.

The ABCD matrix for the first lens is:

$$\begin{bmatrix} A & B \\ C & D \end{bmatrix} = \begin{bmatrix} 1 & 0 \\ -1/f_1 & 1 \end{bmatrix}$$

This is followed by a distance of free space d:

$$\begin{bmatrix} 1 & d \\ 0 & 1 \end{bmatrix}$$

The collimation portion of the system is performed by a focusing lens of focal length f_2 . The beauty of the ABCD approach is that the system matrix is simply the ordered product of its component matrices, and the new Gaussian beam parameter may be found through:

$$\frac{1}{q_0} = \frac{1}{R(z)} - \frac{i\lambda}{\pi w^2(z)} = \frac{1}{R(z)} - \frac{i}{z_0}$$

$$q_1 = \frac{A + Bq_0}{C + Dq_0}$$

For numerical solutions of optical systems, using the system transfer matrix is an excellent approach. However, because all terms – even negligibly small terms – are included, it can lead to an unwieldy analytical solution. In this case, we will propagate the beam stepwise through the elements, eliminating small terms at each step[26]. Placing the incoming waist at the input of the expansion lens yields:

$$\frac{1}{q_1} = \frac{1}{q_0} - \frac{1}{f_1} = -\frac{1}{f_1} - \frac{i}{z_0}$$

For this lens, f_1 is -6.3 mm, but z_0 is roughly 13.3 meters, yielding:

$$q_1 = -\left(\frac{f_1 - \frac{if_1^2}{z_0}}{1 + \left(\frac{f_1}{z_0}\right)^2}\right) \approx -f_1 + i\frac{f_1^2}{z_0}$$

Propagating a distance d to the collimating lens gives:

$$q_2 = q_1 + d = (d - f_1) + i\frac{f_1^2}{z_0}$$

$$\frac{1}{q_2} = \frac{(d - f_1) - i \frac{f_1^2}{z_0}}{(d - f_1)^2 + \frac{f_1^4}{z_0^2}} \approx \frac{(d - f_1) - i \frac{f_1^2}{z_0}}{(d - f_1)^2}$$

And through the collimating lens:

$$\frac{1}{q_3} = \frac{(d - f_1) - i \frac{f_1^2}{z_0}}{(d - f_1)^2} - \frac{1}{f_2}$$

We want to place a beam waist on the output face of the second lens. At a waist, the real part of the Gaussian beam parameter goes to zero; solving for the lens-to-lens separation gives:

$$d = f_1 + f_2$$

$$\frac{1}{q_3} = \frac{-i\lambda}{\pi w_0^2} \left(\frac{f_1}{f_2} \right)^2$$

The new beam waist is thus scaled by the lateral magnification factor predicted by geometrical optics. Since we are working in a size regime five orders of magnitude larger than the wavelength, this is expected. With an input beam waist diameter of 3 mm and lens focal lengths of -6.3 mm and 50.8 mm, this yields a new beam waist with a diameter of 24.2 mm, just under the clear aperture of the 25.4mm PAC 040 achromats.

If we use this beam waist as the input to the final collimating lens, and the Airy criterion from above to estimate voxel resolution, we obtain a lateral spot size of 1.36 microns. Conversely, using the ABCD technique to propagate the beam to the final focal point yields:

$$w_4 = \frac{f\lambda}{\pi w_3}$$

This gives a Gaussian waist with a diameter of 0.71 microns; this differs from the Airy resolution by a factor of nearly two. In this case, since we are assuming a Gaussian profile to the incoming beam, rather than a uniform (top hat) profile, the Gaussian solution should be closest. It is worth recalling that both these approaches are approximations. The Fraunhofer approximation, from which the Airy resolution limit is derived, and the Gaussian approximation both assume that the lateral components of the electric field are small. In free space systems, this assumption is not necessarily true near a beam waist for spot sizes comparable to the wavelength of the light. Both approximations are still useful as rough guidelines when analyzing design tradeoffs between working distance, resolution, and system cost.

In general, the asphere based systems had significantly faster optics, and thus smaller nominal spot sizes, assuming diffraction-limited propagation. For example, one system which was later tested replaced the final PAC040 with a Newport KPA031 asphere as the final focusing lens. With its focal length of 17 mm, this gives a NA of 0.58 and Airy spot size of 0.56 microns. Note that the sole reliance on the diffraction limit to resolution neglects potential aberration-induced distortions of the focal region. Without a raytracing analysis to determine focal spot quality, these systems would have to be tested experimentally.

The design process thus resulted in two basic designs that delivered adequate working distance at low cost. A system built from achromats should have a nearly diffraction limited focus, at the expense of resolution; systems using an aspheric lens should have better resolution if the lenses were in fact diffraction limited.

Volume Resolution

Since we intend to ablate a voxel, a volume element, we should consider longitudinal resolution as well as spot size. We will use the Gaussian beam approximation along the axis of the beam to solve for approximate resolution. Taking the intensity from the above expression for the electric field along the beam axis gives:

$$I(0, z) = \frac{I_0}{1 + \left(\frac{z}{z_0}\right)^2}$$

To compare the longitudinal spot size to the beam waist size, we choose the $1/e^2$ point along the beam axis:

$$I(0, z) = \frac{I_0}{1 + \left(\frac{z}{z_0}\right)^2} = \frac{I_0}{e^2}$$

Or

$$z = \frac{\pi w_0^2 n}{\lambda} \sqrt{e^2 - 1}$$

For our system, and assuming an index of refraction of 1.4 for PDMS, this gives a longitudinal resolution of 10.5 microns.

Since any device will be fabricated by a string of sequential laser pulses, modeling a pulse chain may yield insight into the scales of the completed devices. With the Gaussian approach, this is straightforward. The Gaussian beam can be treated as a scalar field, and a surface of constant

intensity drawn around the focal point. Figure 3 shows a single voxel for a beam with an NA of 0.24 – the beam generated by the PAC 040 achromat system analyzed above - at a wavelength of 532 nm and a contour value of half the peak intensity at the focus. Figure 4 compares this voxel to that generated by a Newport MV-40X objective. With an NA of 0.65, this objective has a nominal spot size of 0.50 microns (Equation 2); note the vastly larger voxel generated by a beam waist only 2.7 times larger than that of the microscope objective system. Note also that these voxels imply different energy levels. The volumes shown are for beams with the same peak intensity; the smaller voxel requires much less total energy to reach the same intensity at the center.

If we treat a channel as the sum of the individual channels, a smooth surface emerges. This model one would use for single photon lithographic processes. An example of this is shown in Figure 5. An array of Gaussian foci are combined, and treated as a single scalar field; the constant intensity contour is then drawn around the combined field.

Ablation, however, is a fundamentally sequential process. Each ablation pulse alters the nature of the material. Material is vaporized, melted, graphitized, and redistributed; if a pulse overlaps the region ablated by the pulse before it, it will be absorbed and scattered by the ablated region. Modeling these processes is beyond the scope of this work, however, some insight may be gained by simply plotting overlapping discrete voxels. An example of this approach is shown in Figure 6. Note that this channel, composed of discretely contoured voxels, is substantially rougher than the one obtained by the combined field approach; this suggests that ablated channels will display the pulse spacing of the ablation process quite clearly.

The convergence of the focus also affects the threshold fluence required to initiate ablation. Again, using a Gaussian model for the beam we have:

$$I(r, 0) = I_0 \exp\left(\frac{-2r^2}{w_0^2}\right)$$

The total power crossing the plane of the beam waist will be:

$$(3) \quad U = \int_0^{2\pi} \int_0^{\infty} I(r, 0) r dr d\theta = \frac{I_0 \pi w_0^2}{2}$$

Thus, for a certain minimum intensity required to initiate ablation, the total power will grow quadratically with beam waist size. Also note that the intensity reached at the focal point is high. A 1 mJ beam with a pulse length of 5 ns has a peak power of 200 kW; when focused through our example PAC 040 system, the intensity reached at the focus is 25 terawatts / cm². The power density at the surface of the sun, by contrast, can be derived from Stefan-Boltzmann law for a black body:

$$j = \sigma T^4$$

In the above equation, σ is the Stefan-Boltzmann constant, and is equal to $5.67 \cdot 10^{-8} \text{ W m}^{-2}\text{K}^{-4}$. At the Sun's temperature (5780K), this translates into an irradiance of 6.3 kW / cm²; the power

density at the focus of the incident beam is thus over 40 billion times that at the surface of the sun. Conversely, if we consider the ablated region as a blackbody in radiative equilibrium with the pump laser, the temperature at the focus is approximately 1.4 million Kelvin.

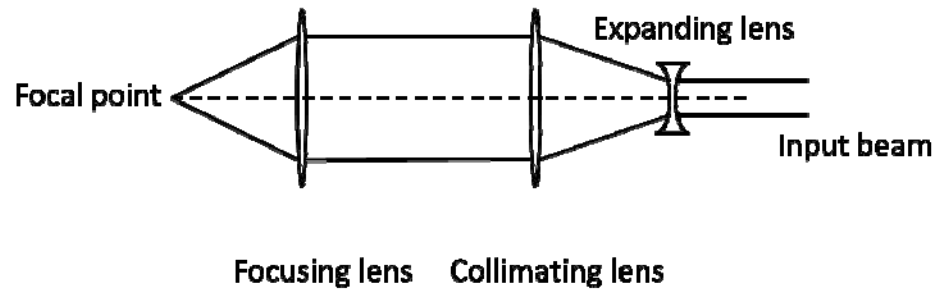


Figure 1: Schematic of optical system.

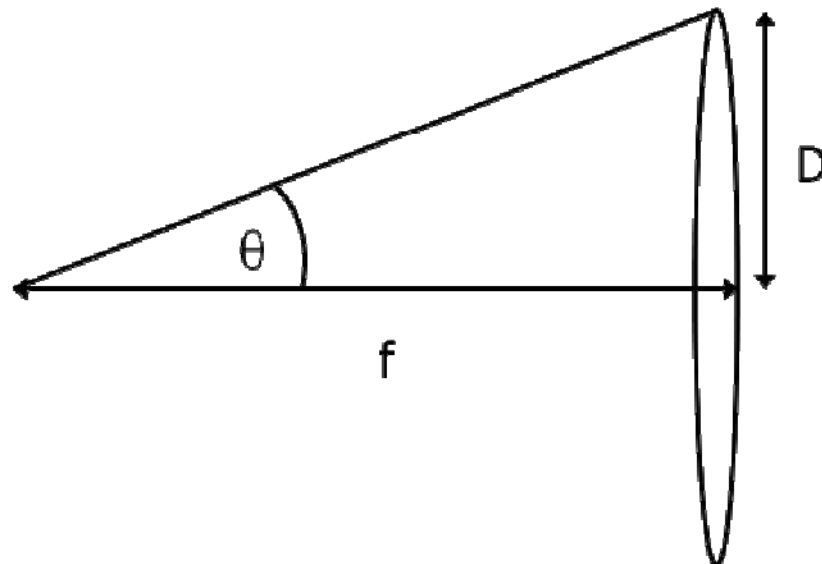


Figure 2: Focusing lens, focal length, convergence angle.

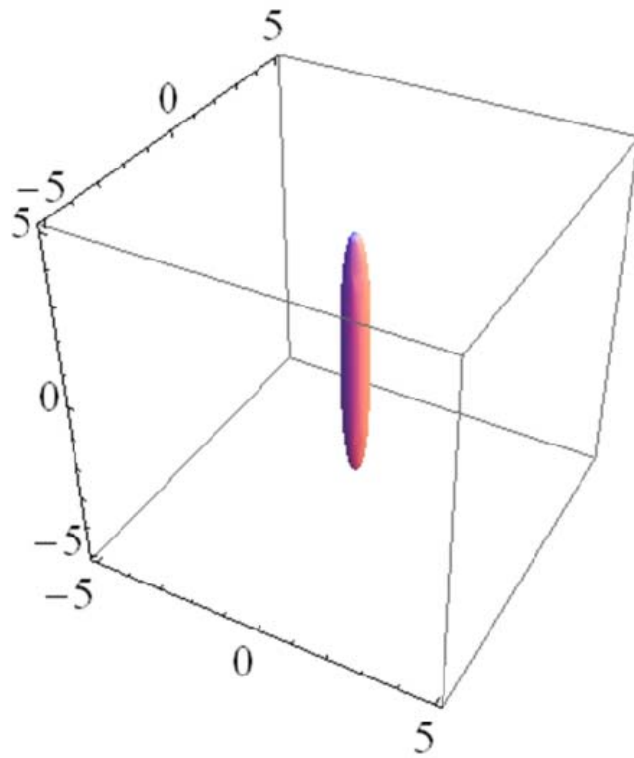


Figure 3: Single voxel, 0.24 NA at 532 nm, 50% peak intensity contour, all axes in microns.

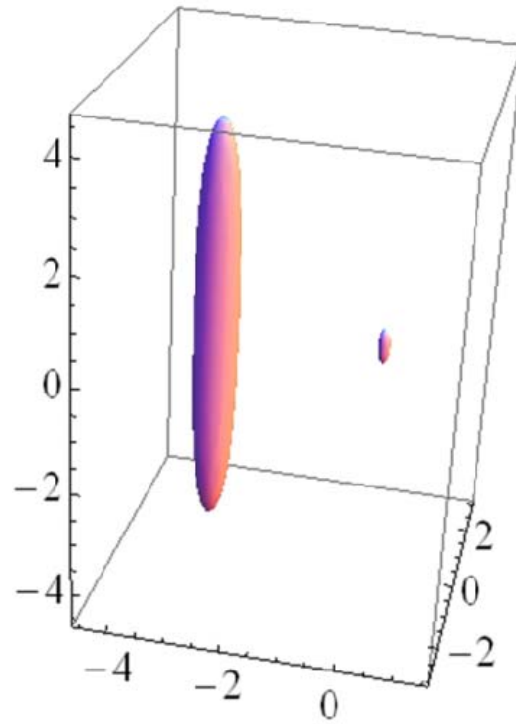


Figure 4: Discrete voxels, 50% peak intensity contours, corresponding to input beams with NAs equal to 0.24 and 0.65 at 532 nm, all axes in microns. Both voxels are shown with the same peak intensity; the 0.65 NA voxel thus requires much less total energy than the larger voxel.

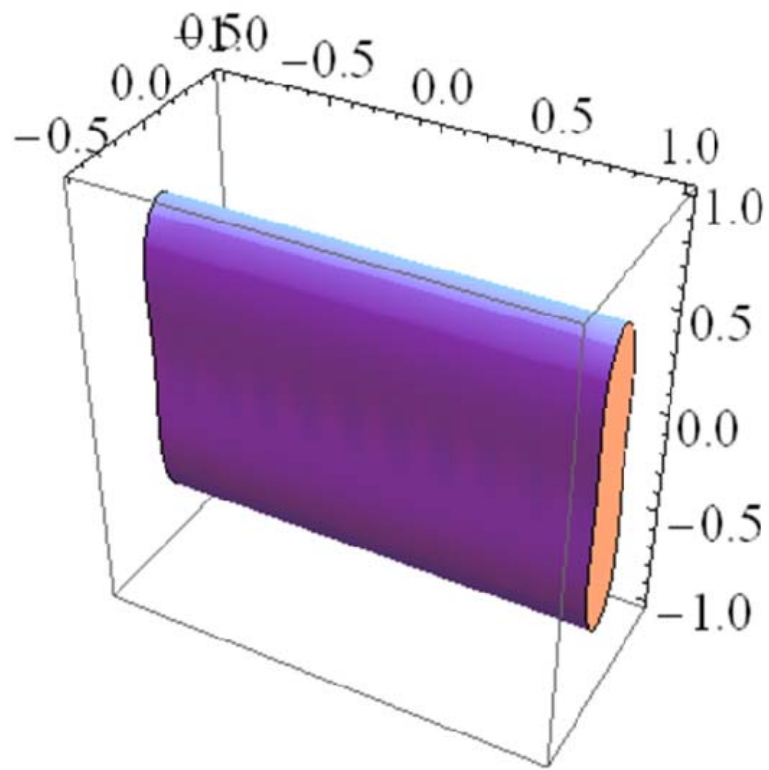


Figure 5: Additive channel, 0.2 micron spacing, 0.65 NA, 532 nm, 50% peak intensity contour, all axes in microns.

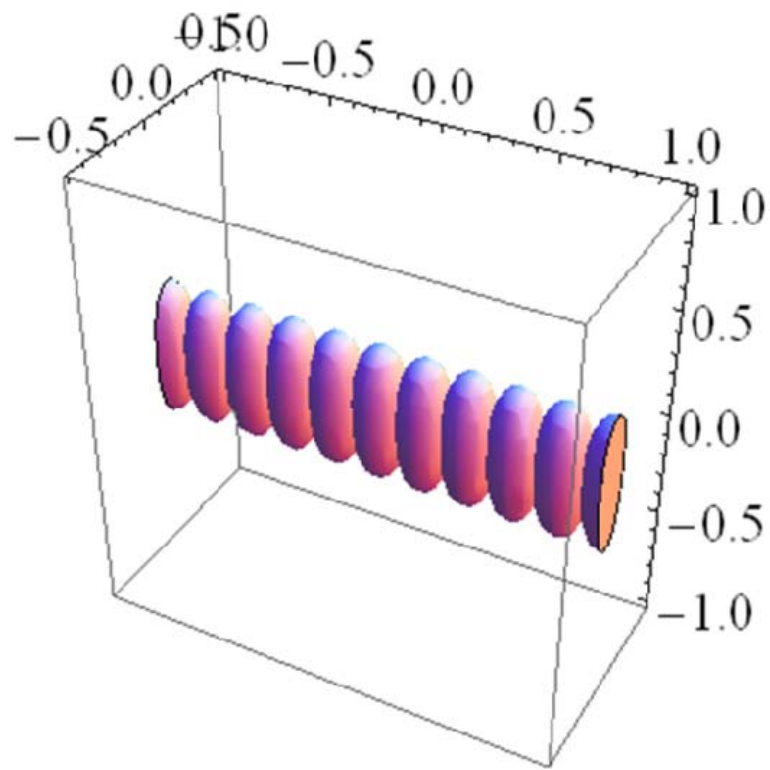


Figure 6: Channel modeled as discrete, pulses. 0.20 micron pulse spacing, 0.65 NA, 532 nm light, 50% peak intensity contour, all axes in microns.

Chapter 5

FABRICATION PROCESS AND RESULTS

Experiment Design

The first features to be attempted were simple embedded channels and vias (vertical channels). These are the basic building blocks for more complex systems, and thus worth the effort of optimization. The ablation system gives us several parameters to explore, some of which may be computer controlled. The spot size and focal quality of the incoming laser beam may be adjusted by choice of optical system. The pulse energy may be adjusted manually. Voxel spacing, laser pulse rate, and stage velocity may be adjusted by computer control.

While modeling the optical system through analytic or raytracing techniques is fairly straightforward, analytic modeling of this type of ablation process presents a number of challenges. For laser pulses with lengths greater than a few picoseconds, the bulk of the damage will be thermally induced[17]. For an isolated voxel, ablation may be initiated when the applied electric field induces photoionization (picosecond timescales) or when enough energy has been transferred to the material by electron heating to induce damage[17]. This takes place on timescales of picoseconds.

Our laser has a nominal pulse length of 5 ns. Energy flow into the ablated region thus continues long after ablation has been initiated. For a simple nonreactive dielectric such as silicon dioxide, the laser boils, fractures, and generally violently redistributes the material. In our case, however, we are ablating a polymer. In addition to the mechanical/hydrodynamic thermal processes, the

polymer breaks down, resulting in a variety of new compounds with much higher absorbance than pure bulk PDMS. Each successive laser pulse will see a completely different environment at the focal point than the preceding one. Modeling channel formation by sequential voxel ablation thus requires modeling a large set of complex nonlinear physical processes.

Rather than modeling the ablation process for channels, process optimization was performed by a brute force parameter sweep approach. Initially, ablation of isolated voxels was performed; once this could be accomplished, large arrays of channels were written at varying voxel spacing. This was repeated for a span of pulse energies. These arrays were characterized in an electron microscope (SEM), and by fluidic testing. This entire process was repeated for several optical systems.

Focusing Optics

The initial system used was based on Newport PAC040 achromats. This is a fairly slow system – about $F/2$ – and was initially used as a test bed for system debugging. The long focal length to lens diameter ratio leaves a large amount of clear space above the sample. A side-mounted camera could then be used to view the ablation process in real time, facilitating debugging of the system control software.

The next systems implemented were based on fast, molded aspheric condenser lenses. These (Newport KPA 046, KPA 031) are extremely fast ($F/0.66$), and thus promised excellent spatial resolution. They were used as focusing lenses, with the expander/collimator portion of the system based on conventional spherical lenses.

The optical system was then rebuilt with the achromat-based design. While this results in a slower beam, achromats possess low aberration, and thus should result in a larger, but very clean focal spot. A wide set of pulse energy and voxel spacing parameter sweeps were performed with this system.

The final, and most effective system used combined a microscope objective (Newport MV-40X, NA 0.65) as the focusing element with an achromat expander/collimator. This system has numerous disadvantages – short working distance, limited pulse energy damage threshold for the objective – but should produce both a clean and small beam focus.

Process Flow and Testing Procedures

The process flow for a channel/via test sample begins with casting a PDMS blank. Raw PDMS monomer (Dow Sylgard 184) was mixed with catalyst at a 10:1 ratio. Mixing times were at least five minutes, followed by at least three minutes of defoaming. Mixed PDMS was then carefully poured into the stainless steel mold described in the ablation system chapter. This was placed in a vacuum chamber, and degassed until no bubbles were visible. The degassing process typically required thirty minutes, but could vary between fifteen and ninety minutes depending on how carefully liquid PDMS was poured into the mold. The mold was then closed, preloaded with springs, and allowed to rest undisturbed for a minimum of one day. Initially, the mold was cured in an oven at 80°C. While this usually worked well, the thermal expansion of even a small residual air bubble by oven curing would result in a large distorted area on the final blank. Longer curing times at room temperature eliminate this risk. For the first few PDMS castings, wax (Meguiar's Cleaner Wax) was applied to the stainless mold to act as a mold release. The wax was then stripped from

the mold and cured PDMS blank by a liberal application of isopropanol (IPA). The use of a mold release agent was later found to be unnecessary; later castings relied on a simple thorough cleaning of the mold with IPA prior to pouring the PDMS.

Once cured, molding flash was removed from the blank with a razor. The blank was mounted in the system, and ablated. Post ablation, the slab was manually diced with a razor, and either examined via SEM or processed for fluidic testing.

Samples destined for SEM analysis were cleaved normal to the channel direction. Cleaving in lieu of cutting ensures a clean surface. In the case of a thick block of flexible polymer, cleaving is performed by making a deep incision with a razor and steel rule, and then carefully (slowly) bending the sample along the cut. Prior to SEM imaging, samples were sputtered with a thin layer of AuPd to reduce charging during imaging. All imaging was performed in an FEI Quanta environmental SEM (ESEM). The ESEM allows imaging with soft vacuum (1 Torr); this allows un-metalized samples to be imaged without charging. Some samples were left un-metalized, and imaged in the ESEM mode; the imaging results obtained this way were equivalent to those from metalized samples. Imaging in the normal non-ESEM mode is easier – greater field of view and depth of field – so the bulk of samples were metalized for imaging.

Fluidic connections to the resulting devices were created by punching holes intersecting the channels; these could then be connected to Microbore tubing via stainless capillary tubes. The hole punching process leaves the channel open on the back side of the chip; this must then be bonded to a substrate to seal the system. In the future, it may be possible to obviate the need for a sealing

substrate by punching the connecting hole to an intermediate depth, and mechanically extracting the PDMS slug.

The ablated, punched PDMS chips were sealed to 1 mm thick glass slides with several bonding techniques. The simplest technique was an oxygen plasma treatment of both chip and glass slide; initial parameters used were a 30 s exposure in an 80W plasma at 100 milli Torr. The oxygen plasma ensures a clean, organic-free surface on the glass slide. On the PDMS chip, it breaks down the polymer at the surface, creating dangling bonds which then attach to the silica slide. The plasma-assisted sealing technique results in chips that are ready for immediate use, and can typically support pressures of 15 psi without delaminating.

It quickly became apparent that higher pressures would be required for testing purposes. After all, the channels are packed with residual ablation debris, which must be forced out under pressure. An alternative sealing technique was developed to support higher applied pressures without chip-slide delamination. In this approach, the glass slide was covered with a film of liquid PDMS. Films were applied by spinning, typically at 2000 rpm for 60 seconds; this results in a roughly 10 μm thick layer. The glass slide was then placed in an 80C oven briefly, partially curing the PDMS to a gel state. When the chip is then bonded to the slide, this gel deforms, partially filling the punched holes and forming a mechanical seal between slide and PDMS chip. Controlling the partial cure of the film is crucial for this process to work. Insufficient curing results in a low viscosity gel which can flow up into the punched region, and may seal the channels. Excessive curing prevents adequate deformation of the film. Cure times between 1.5 to 2 minutes worked well. Once bonded, sealed chips were returned to the oven for a minimum of one hour to guarantee a thorough cure. Chips sealed using this technique could tolerate pressures of up to 60 PSI without delamination.

This partially cured sealing film approach works, but requires additional processing effort. During the course of chip fabrication and testing, chips which had been bonded after plasma treatment and then allowed to rest for about 1 week before testing were discovered to have greater resistance to delamination. The mechanism for this is unclear; there could be a long timescale for residual dangling bonds to attach to the glass slide; it is possible that the PDMS chip contained residual uncured monomer which gradually polymerizes while in contact with the slide. Whatever the cause, it was ascertained that combining longer oxygen plasma treatments (120 seconds) with either a post-sealing rest period or overnight placement in an 80C oven resulted in a robust seal. Once this was determined, remaining chips were sealed in this fashion.

Fast Aspheric Condenser System Results

The first optical system to be characterized used inexpensive, molded aspheres as collimating and focusing lenses. It was not possible to obtain the aspheric prescription for these lenses from the manufacturer. It was thus not possible to determine focal point aberration qualities by raytracing. Regardless, it was hoped that the high convergence (F/0.66) would render lens aberrations irrelevant. If we assume a nominally perfect lens, the electric field at the focus is the Fourier transform of the field at the lens aperture. Treating aberrations in the lens as phase errors in the aperture field yields their Fourier transform at the focal plane. Low frequency phase errors would thus be near the focal point, with higher frequency ones farther away. With luck, the phase aberrations in the aspheric lenses would be high frequency in nature, and thus not affect the focal region.

Also, performing ablation at pulse energies near the ablation threshold should result in a cleaner ablated region than would be expected from a distorted beam. Consider a system with spherical aberration; at the focal point, the beam will form a central spot surrounded by a large ring due to the aberration. If the field in the ring is low compared to that at the center of the beam spot, and the system run such that the threshold ablation fluence is only slightly exceeded at the central spot, then the portion of the beam in the aberration ring should pass through the material without effect.

This analysis neglects the effect of longitudinal aberration at the focal point. In fact, none of the aspheric based systems were able to produce clean voxels. Features fabricated using aspheres as condenser lenses inevitably possessed two ablated regions separated longitudinally. An example of this is shown in Figure 1. Besides beam aberration, another cause considered was self-focusing due to the Kerr effect. This could potentially result in a secondary focus. PDMS, however, has a low Kerr coefficient. Also, the energy required to initiate ablation was nearly one mJ. This is a much higher threshold than was observed during system testing with a slower optical system – another indication of poor focal quality. At higher powers – near 10 mJ – the double foci become joined by a thin connecting volume. Rather than attempting to discern the cause of the double foci, systems using molded aspheres were quickly abandoned for a system with known low aberration.

PAC 040 Achromat System Results

The next optical system tried was based on dual F/2 achromats, an ABCD analysis which may be found in the optical system design chapter. Though comparatively slow, this system had the advantage of a low aberration beam, and thus, presumably, a clean focal region. Voxels could be produced at powers as low as 100 μJ ; this was, however, unreliable. At energies of 200 μJ , voxels

could be produced with absolute reliability. Figures 2 and 3 make this comparison quite clear. This range between minimum and reliable thresholds can be partially attributed to pulse-to-pulse energy variation in the laser (up to 10%), and to the presence of defects, such as bubbles, in the PDMS.

A parameter sweep of channel ablation was performed with pulse energies from 100 μJ to 3.2 mJ and voxel spacing from 5 μm to 125 μm ; a parameter sweep of via ablation was performed at the same powers, with vertical voxel spacing ranging from 5 μm to 200 μm . Note that vias are cut from the inside of the material up towards the top surface; this prevents the ablated via from obscuring the laser.

There were two basic limits on voxel spacing and pulse energy for ablating continuous structures. If the voxel spacing is too high for a given power level, gaps will remain between successive voxels, resulting in a discontinuous channel. If the voxel spacing is too low for a given power level, the features will “bloom” into large bubbles of melted and reflowed material. This blooming effect occurs even at the lowest power levels, at spacing down to 10 μm . Bloomed areas can block the beam, and thus result in gaps in the channels or vias. The effect is dramatically worsened at higher powers and in vias; see Figures 3 and 4.

Channel and via test blocks were imaged via SEM, and heights and widths recorded. Channel widths were fairly constant for given pulse energy level, and ranged from about 20 μm (200 μJ) to 50 μm (3.2 mJ). Channel heights displayed more variance; Figure 5 shows the channel heights obtained from the energy/spacing parameter sweep. In general, reduced voxel spacing results in increased channel height; intuitively, the greater overlap between successive voxels results in more absorbed energy, and thus a taller channel.

Once a range of pulse energies and voxel spacings which produced smooth channels were indentified, structures designed for fluidic testing were produced. These consisted of arrays of 10 mm long channels connected to the surface by vias the end of each channel. The vias were used solely as alignment fiducials to facilitate accurate placement of the cylinder punch, and were removed during punching. Pulse energies of 600 μJ and 800 μJ were used; voxel spacing was swept within the arrays. Once punched and sealed, these test blocks were connected to water filled Tygon Microbore tubing via stainless capillary tubes. The water filled tubing was connected to a dry nitrogen pressure regulator, and pressure was applied to the embedded channels. Despite testing a wide range of channel ablation parameters, and applied pressure, it was not possible to obtain liquid flow through the channels.

In order for the channels to successfully carry liquid flow, the bulk of the residual material created by the ablation process must be flushed out. It was hoped that this residue would largely consist of graphitized PDMS in small grains, which would easily detach from the channel and be swept clean by flowing water. SEM examination of these channels revealed, however that the ablation residue has a larger structure than hoped (Figures 6 and 7). Rather than smaller grains of material, the residue forms a porous, sponge-like structure. In addition to graphitized PDMS, this likely contains large quantities of melted and recast PDMS. Under applied pressure, the residue adheres to the channel walls and blocks fluid flow.

Reducing the voxel spacing – thus increasing the overlap between successive pulses – might somewhat reduce this debris structure. If each successive laser pulse applies damage to previous voxels, then the melted, recast material blocking the channel should be further graphitized and reduced in scale. Unfortunately, with this optical system, even channels fabricated close to the

minimum ablation energy display blooming at low voxel spacing. One possible way to mitigate this is to switch to a laser with faster pulses. This would allow lower energy pulses to have the same peak intensity. This should mitigate thermal effects by reducing the total amount of energy deposited.

In addition to the thermally induced channel/via blooming, channels produced with this optical system suffered from decreased placement accuracy. As lateral channels were ablated, the center of the channel would rise towards the direction of the incoming laser beam. This process is a direct result of the altered optical environment presented to the beam on successive pulses; on the first pulse, ablation is initiated at or near the focal point of the beam. On the second pulse, however, the previously ablated voxel acts as an absorption defect, and ablation is initiated at a vertically shifted point from the beam focus. This vertical shift between successive voxels continues until an asymptotic limit is reached; on some channels, this resulted in vertical shifts up to the full height of the channel between the channel start and the asymptotic steady state. For a system designed to accurately define ablated features within bulk material, this is unacceptable.

Some insight may be gained by recalling that the convergence of the incoming beam is fairly low. With an F/2 optical system, the beam convergence half angle is 26 degrees in free space. With a nominal index of refraction of 1.4 inside the PDMS, this drops to 18 degrees. The light is thus largely approaching the voxel from the vertical direction. If we increase the convergence angle, the effect of vertically placed absorption defects should decrease as more light approaches the focus from the sides. Moving to a faster optical system should mitigate this effect.

The combination of blooming, porous ablation residue, and vertical shift during channel formation led to the abandonment of this optical system in favor of a microscope objective based one.

Microscope Objective System Results

The final optical system combined a Newport MV-40X microscope objective with the achromat based collimator of the previous optical system; the final focusing lens was replaced by the objective. This system had a higher NA (0.65) than the other systems, with corresponding increased beam spread angle and decreased spot size.

This system posed two immediate challenges. First, since the working distance of the objective (nominally 600 μm) is short compared to its width, the exit face of the objective needed to be aligned parallel to the top surface of the PDMS chip. This was accomplished by mounting the objective on a small tip/tilt stage, mounting a dial indicator on the XYZ stage block, and carefully adjusting the angle of the objective to align the output face to the XY axes of motion. Combined with the precision-cast PDMS chips and leveled mounting chuck, this ensured relative parallelism accurate to 10 μm over the objective output face. To compensate for this and other mechanical error sources in the system, a nominal minimum distance of 50 μm was maintained between the objective and PDMS chip.

Second, since these inexpensive objectives are not designed to handle large fluences, they can easily be destroyed by the pulsed laser system. This occurred either when high pulse energies were applied, or when the output lens of the objective was not perfectly clean. Since cutting features near or at the surface of the PDMS results in a spray of ejected material, the objective had to be periodically inspected and cleaned of ejected ablation residue. Later features would be cut entirely

within the bulk of the material with no vias connecting to the surface, eliminating this source of failure.

The collimated beam produced by the PAC040 has a width of approximately 24 mm; this overfills the clear aperture at the input of the objective. This reduced the maximum pulse energy available for ablation by a factor of 8.1; this was determined by measuring the energy at the input and exit planes of the objective and performing a linear fit. Sampling only a small central aperture of the collimated beam, produces a fairly clean, constant field at the objective input plane, and thus a clean, Airy-limited spot when focused, rather than a Gaussian one. While this clipping is wasteful of laser power, the total pulse energy available (12 mJ) far exceeded the amount required for ablation.

The threshold energy for reliable ablation was found to be 40 μJ . Rather than beginning with an extensive energy/spacing parameter sweep, as was performed for the achromat based system, a set of channels for fluidic testing was fabricated with best-guess parameters for pulse energy (45 μJ – slightly over the ablation threshold) and voxel spacing (1-10 μm sweep). Fluidic testing of the completed chip immediately yielded functional channels (Figure 8).

Following the success of the initial channels, a parameter sweep of voxel spacing was performed at 50, 100, and 150 μJ for SEM analysis. Figures 9 and 10 show SEM cross sections of channels and vias cut at typical process parameters. As hoped for, the ablation residue was primarily composed of granular debris, typically about 5 μm in scale. While the feature sidewalls are rough, and show some evidence of melted and recast material, the visible effects of this process are greatly reduced compared to channels fabricated with the slower F/2 achromat system.

Channel heights and widths extracted from SEM imaging are plotted in Figures 11 and 12. As expected, channel height increased with increased pulse energy, and increased with decreased voxel spacing as well. Via widths also followed a similar pattern, starting at roughly 20 μm for 100 μm spaced voxels, and increasing to roughly 30 μm for voxels spaced at 5 μm (Figure 13). Channel widths were surprisingly invariant with voxel size.

The increase in the variance of the measured channel height as voxel spacing decreases may be attributed to increasing channel roughness as the voxel spacing increases. With each laser pulse essentially carving out a roughly ellipsoidal volume, as the distance separating each pulse increases, so does the resulting scalloping. Only when inter-voxel spacing is small compared to voxel size does a smooth surface result. This is visibly apparent when channels are viewed from above with an optical microscope (Figure 13a-c). Minimum voxel separations to ensure smooth and functional channels were 3, 6, and 8 μm for the 50, 100, and 150 μJ pulse energies. There is a tradeoff between channel quality and fabrication time. For the 100 μJ case, functioning channels could be cut with 10 μm spacing; but had a 50% failure rate when tested for fluid flow. Channels cut at 5 μm spacing generally worked. For a system designed to automatically cut large systems of structures, the spacing/quality tradeoff has a large effect on processing time. Our flashlamp-pumped laser has a maximum repetition rate of 15 Hz; at 5 μm pulse spacing, this gives a cutting rate of 65 μm / second. For

With the microscope objectives' output lens only 50 μm above the surface of the PDMS chip, the average depth of channels cut at 100 μJ was 624 μm . This is shallower than we expect. Applying Snell's Law, and solving for the working distance geometrically, we obtain a depth scaling factor s :

$$s = n \frac{\sqrt{1 - (NA/n)^2}}{\sqrt{1 - (NA)^2}}$$

With a numerical aperture of 0.65, and index of 1.43, the depth scaling factor is 1.68. With a nominal working distance of 600 μm , and height offset of 50 μm , the channel depth should be 924 μm , assuming the channels are centered on the focal point of the beam. One explanation is that the objective used was designed for microscope use. The working distance assumes a backside focal point 170 mm away (a standard for microscopes); since we are driving the objective with an essentially collimated beam, the working distance drops. We can solve for this error by applying the Gaussian lens formula to the objective:

$$\frac{1}{f} = \frac{1}{s_1} + \frac{1}{s_2}$$

Here, s_1 and s_2 are the lens-to-image distances, and f is the resulting focal length – the new working distance for the objective. This suggests a shift of only 3 μm in the working distance. At present, it is not clear why the maximum channel depth is lower than expected.

The maximum channel depth allows for at least three channels to be fabricated vertically without interference. This allows for more complex three-dimensional structures to be fabricated.

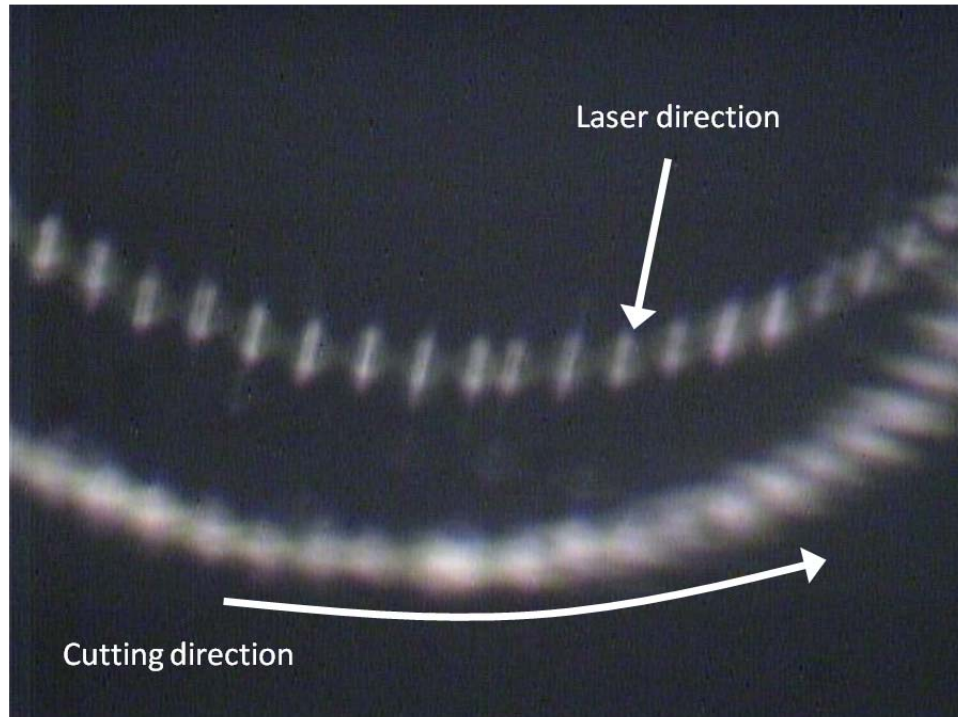


Figure 1: Voxels cut with using a Newport KPA031 asphere as the focusing lens (F/0.66) with pulse energies of 1 mJ. Voxel to voxel spacing is 80 μm ; note the dual longitudinally spaced ablation points. This is an isometric view of a section of a ring; the laser beam enters the material from above.

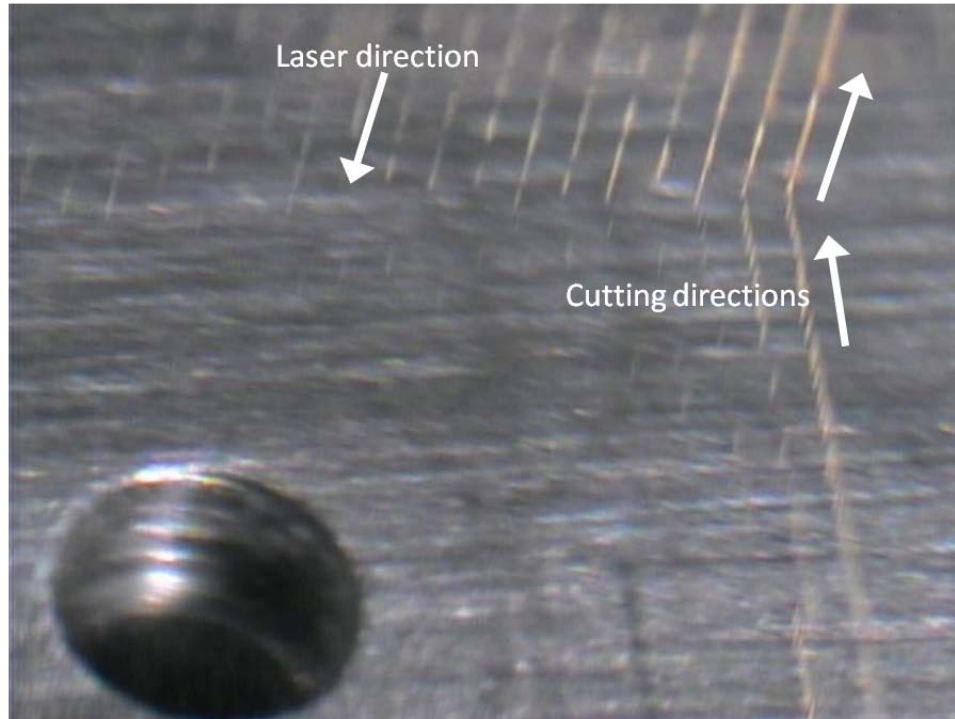


Figure 2: Isometric view of a combined channel (foreground) and via array ablated with a PAC040 focusing lens (F/2) at 100 μJ . The pulse spacing starts at 5 μm on the rightmost channel and increases in 5 μm increments. The laser enters from above.

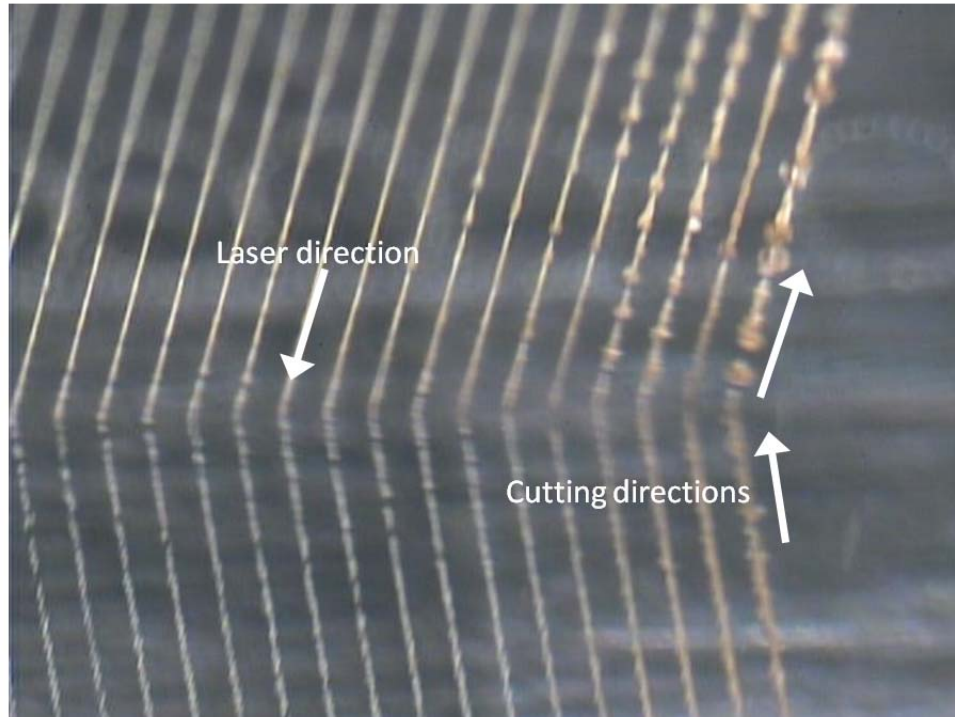


Figure 3: Isometric view of a combined channel (foreground) and via array ablated with a PAC040 focusing lens (F/2) at 200 μJ . The pulse spacing starts at 5 μm on the rightmost channel and increases in 5 μm increments. Thermally induced blooming is visible on the 5 μm spaced channel, but most noticeable on the vias.

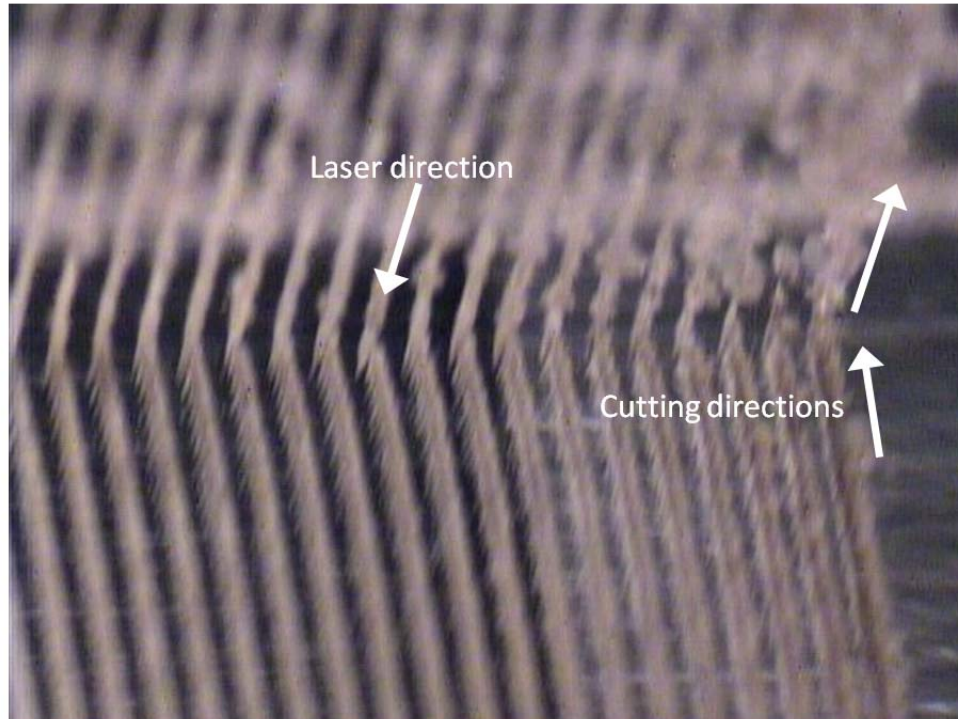


Figure 4: Isometric view of a combined channel (foreground) and via array ablated with a PAC040 focusing lens (F/2) at 3.2 mJ. The lateral pulse spacing starts at 30 μm on the rightmost channel and increases in 5 μm increments; vertical pulse spacing starts at 50 μm , and increases in 7.9 μm increments.

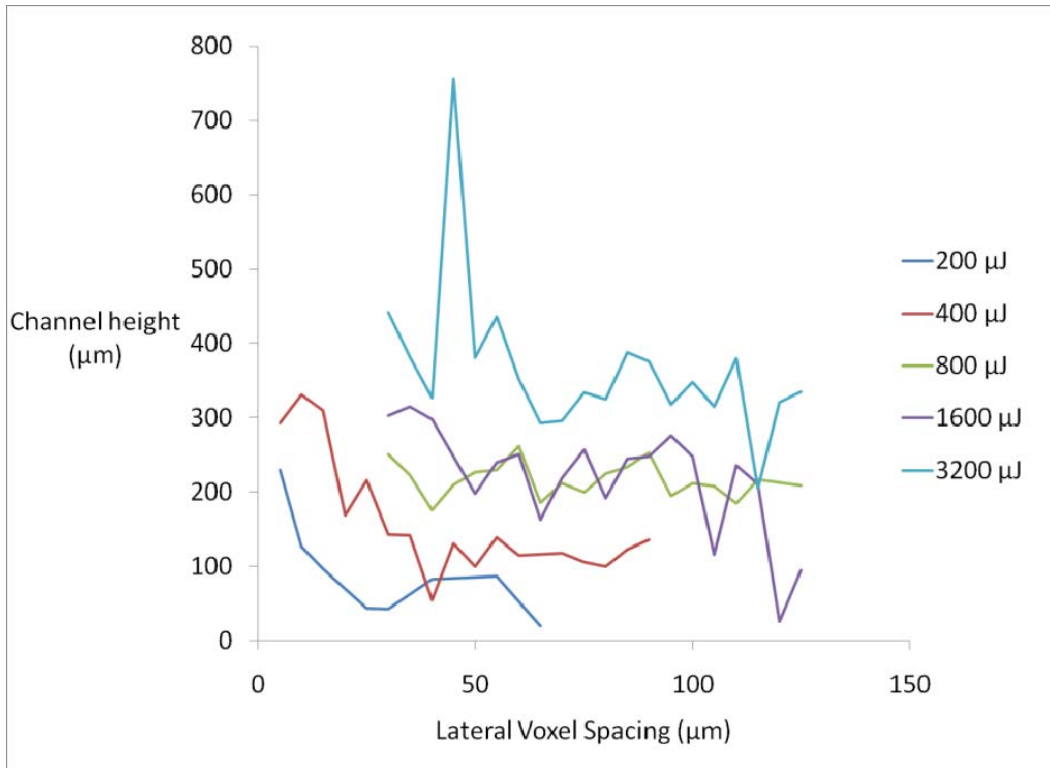


Figure 5: Channel height in μm as a function of pulse spacing for tested pulse energy levels for the PAC040 focusing lens (F/2).

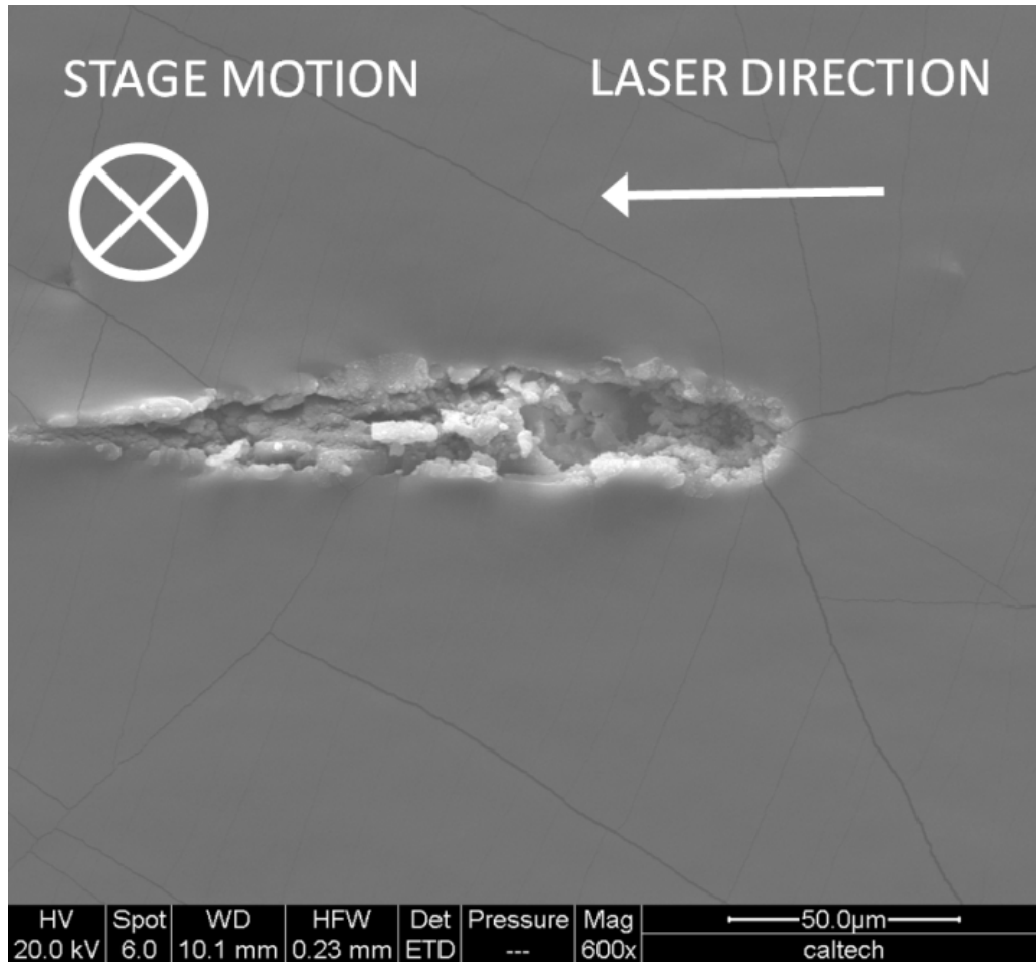


Figure 6: SEM image of a channel ablated with the PAC 040 (F/2) optical system at a pulse energy of $400 \mu\text{J}$ with $20 \mu\text{m}$ spacing. When examined under an optical microscope, this is a smooth, continuous channel. The embedded ablated material forms a porous internal structure, which is not removed under applied fluidic pressure.

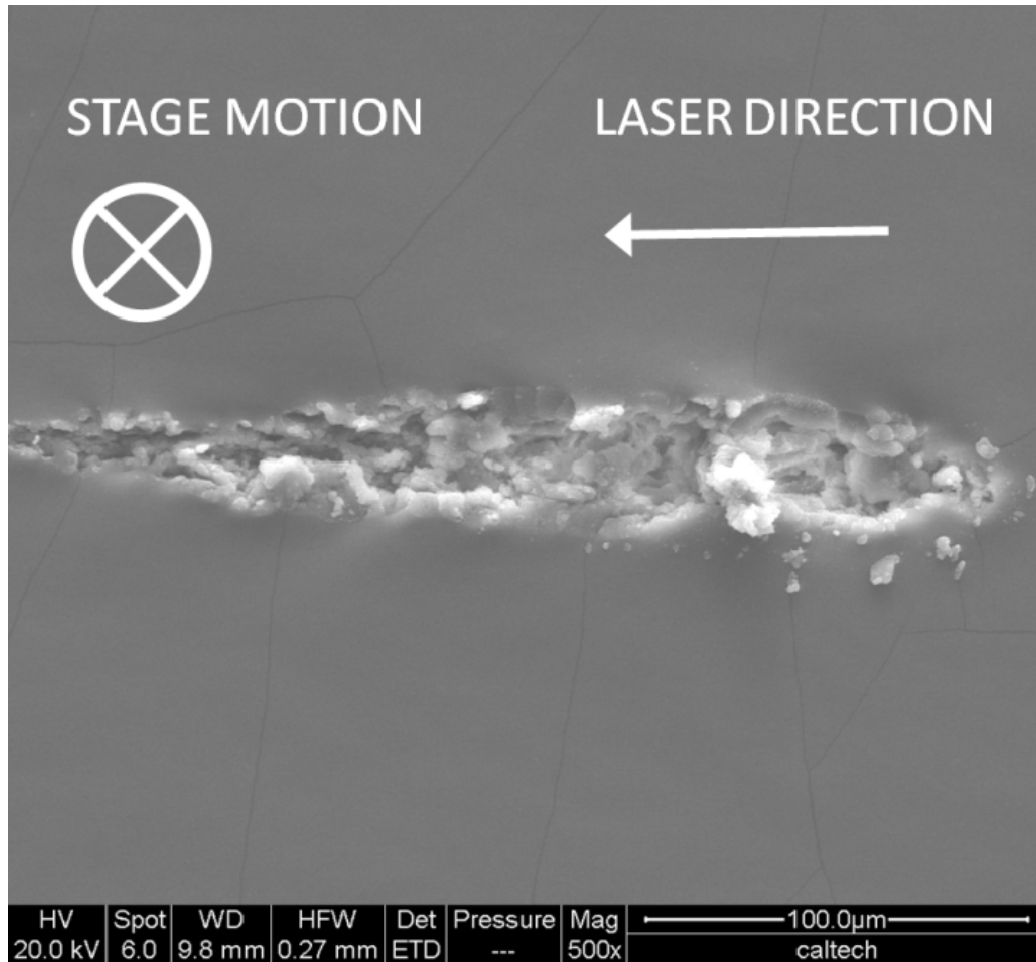


Figure 7: SEM image of a channel ablated with the PAC 040 (F/2) optical system at a pulse energy of 800 μJ with 35 μm spacing. When examined under an optical microscope, this is a smooth, continuous channel. The embedded ablated material forms a porous internal structure, which remains despite applied fluidic pressure.

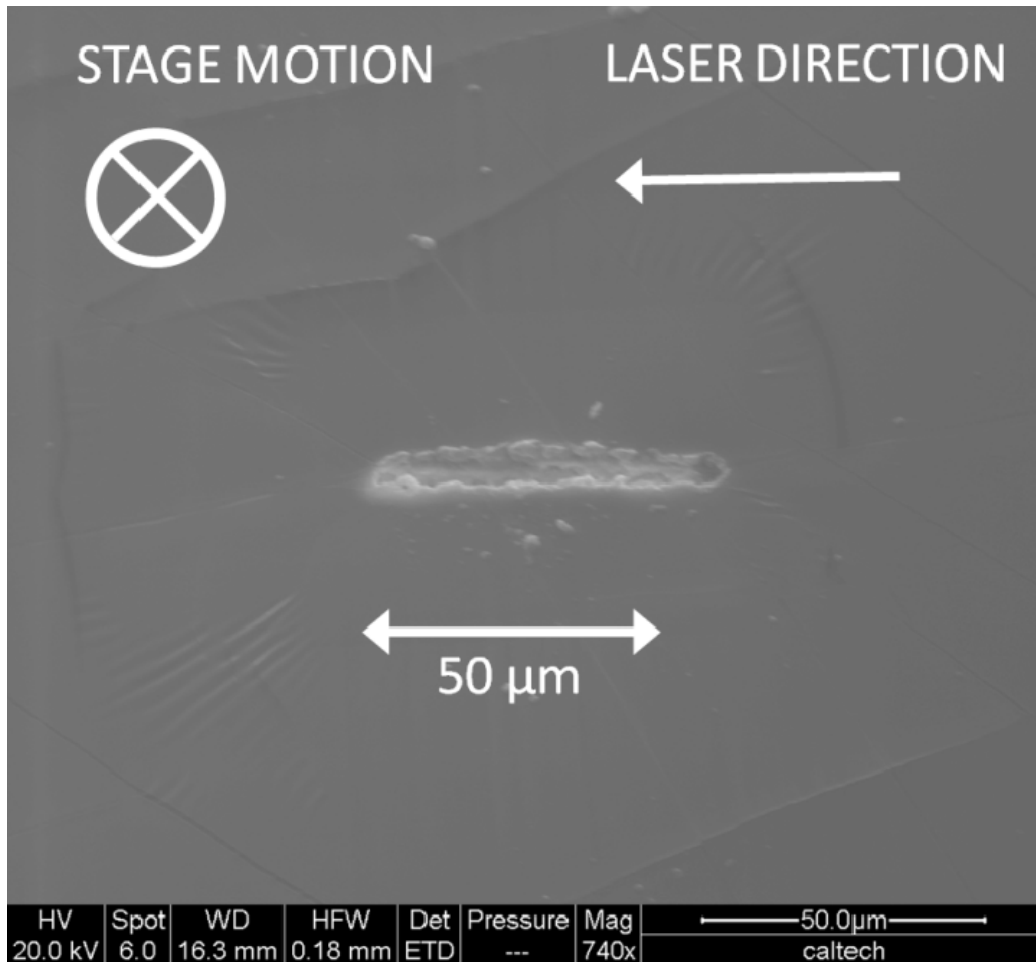


Figure 8: Cross section of one of the first functional channels resulting from the ablation process. This channel was fabricated with $45 \mu\text{J}$ pulses spaced $5 \mu\text{m}$ apart; a microscope objective was used as the focusing element. The channel has been flushed with water, removing the ablation residue. The sample has been cleaved at 90° to the channel direction, and imaged at 20° from vertical.

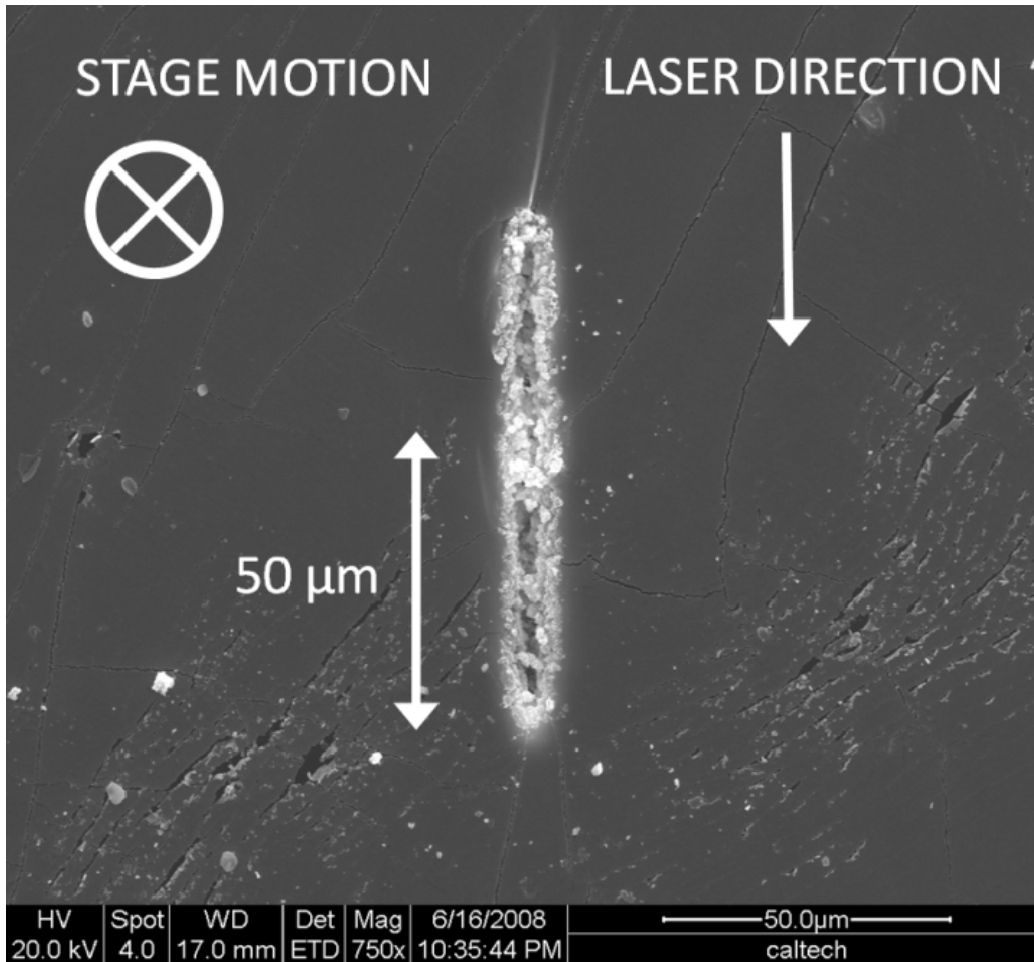


Figure 9: Cross section of a channel fabricated with a 0.65 NA microscope objective with a pulse energy of 100 μJ and voxel spacing of 5 μm . This channel has not been flushed, and thus contains ablation residue; note the comparatively small ablation debris/channel dimension scale.

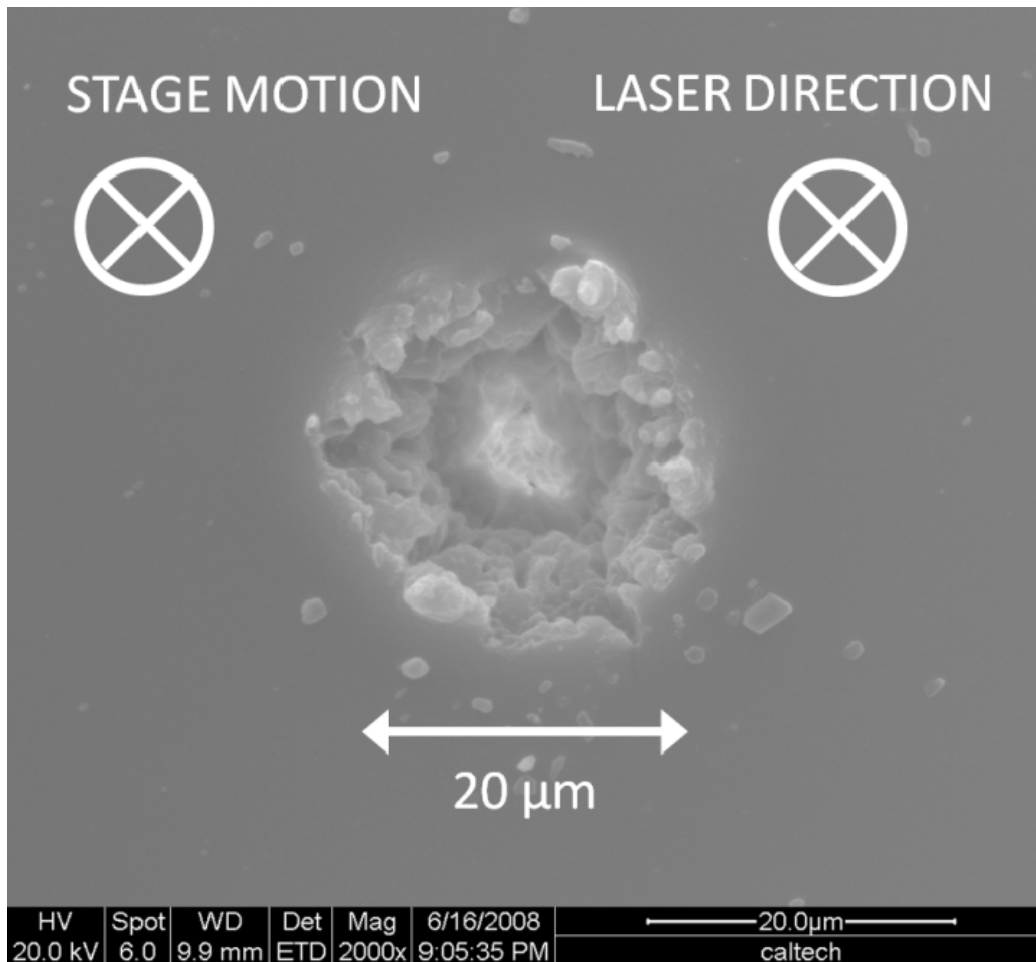


Figure 10: Surface exit of a via fabricated with a 0.65 NA microscope objective with a pulse energy of 100 μJ and voxel spacing of 30 μm . Ablation residue has been removed from the top of the via with compressed air. Vias are cut from within the bulk material towards the top surface, ensuring that the laser focus is not obscured by the feature.

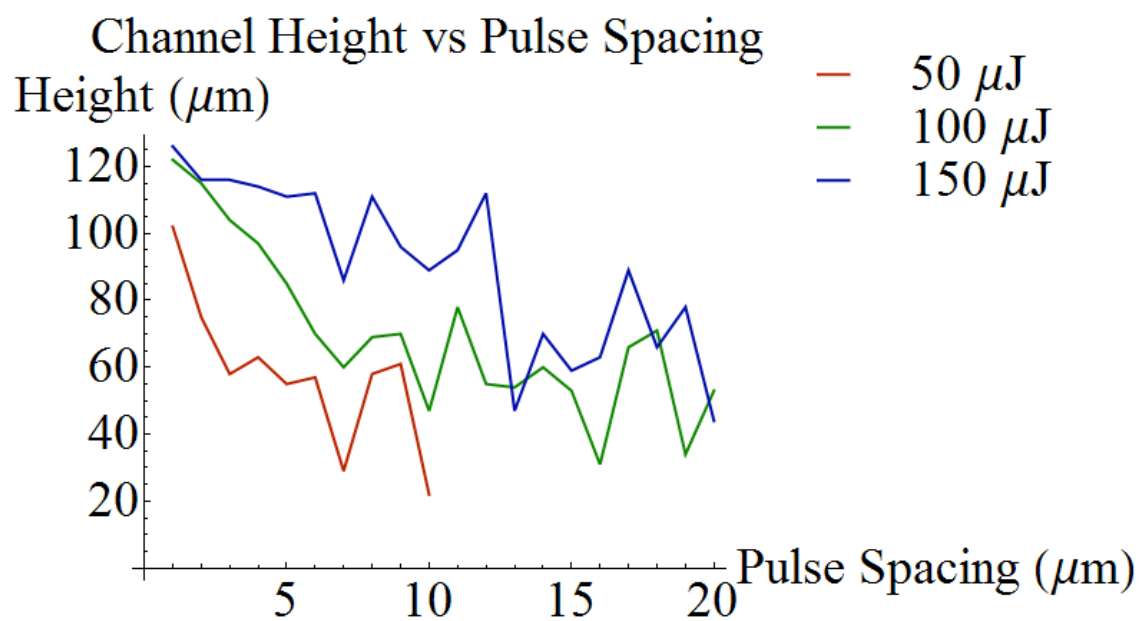


Figure 11: Heights of channels fabricated with a 0.65 NA microscope objective; dimensions were measured by SEM imaging of cross sections.

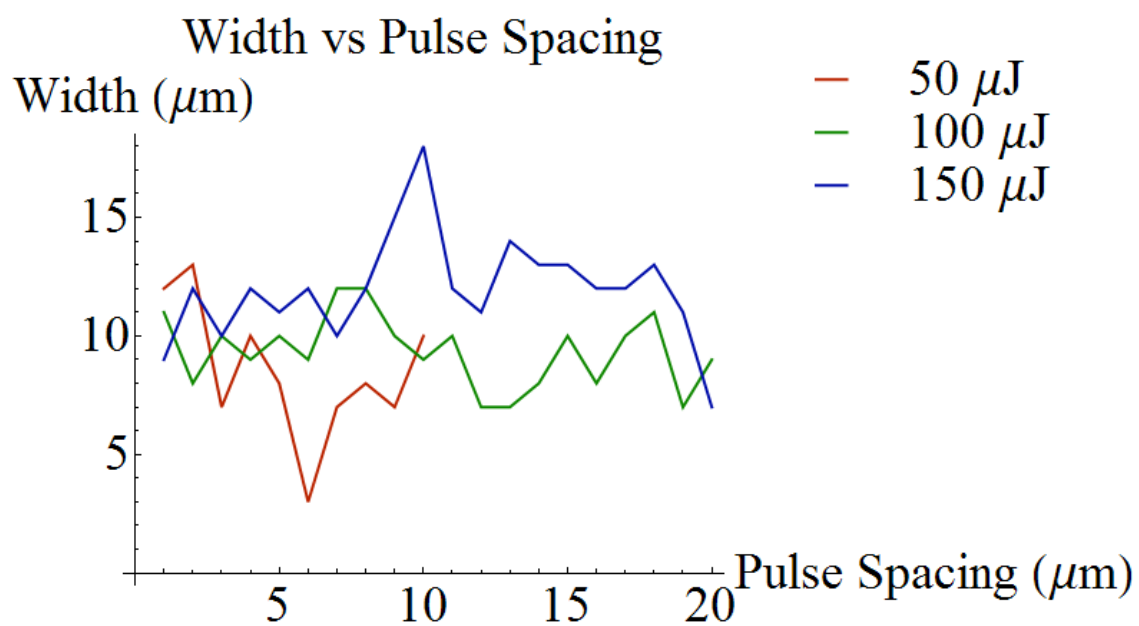


Figure 12: Widths of channels fabricated with a 0.65 NA microscope objective; dimensions were measured by SEM imaging of cross sections.

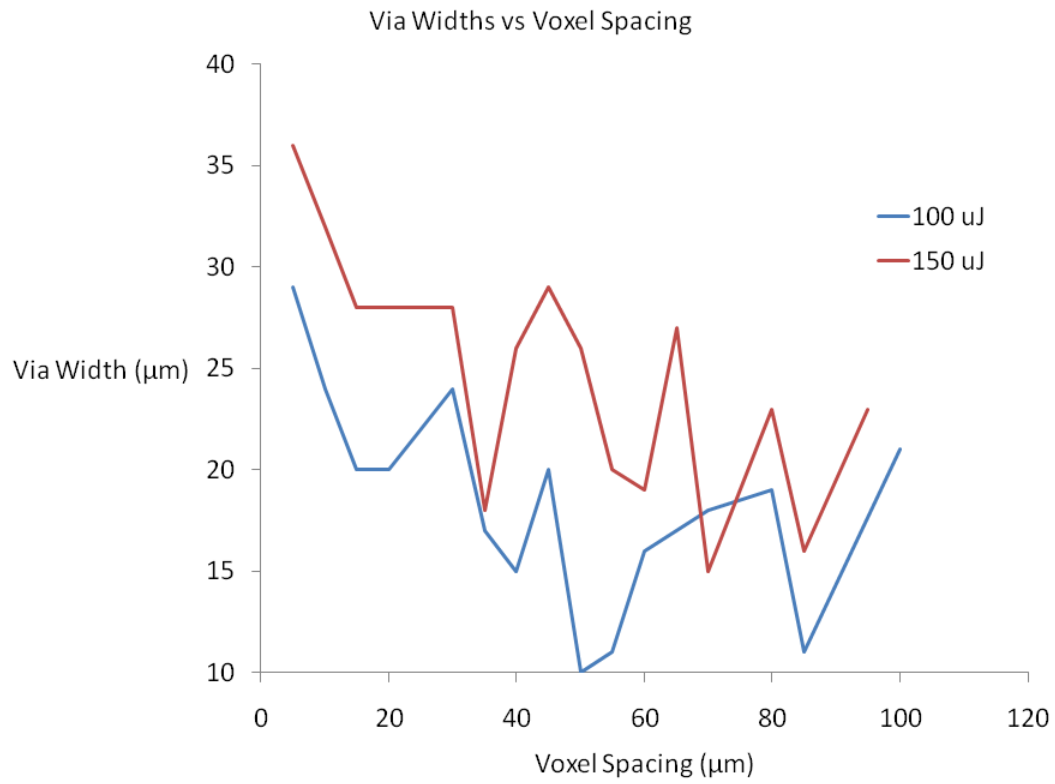


Figure 13: Widths of vias fabricated with a 0.65 NA microscope objective; dimensions were measured by SEM imaging.

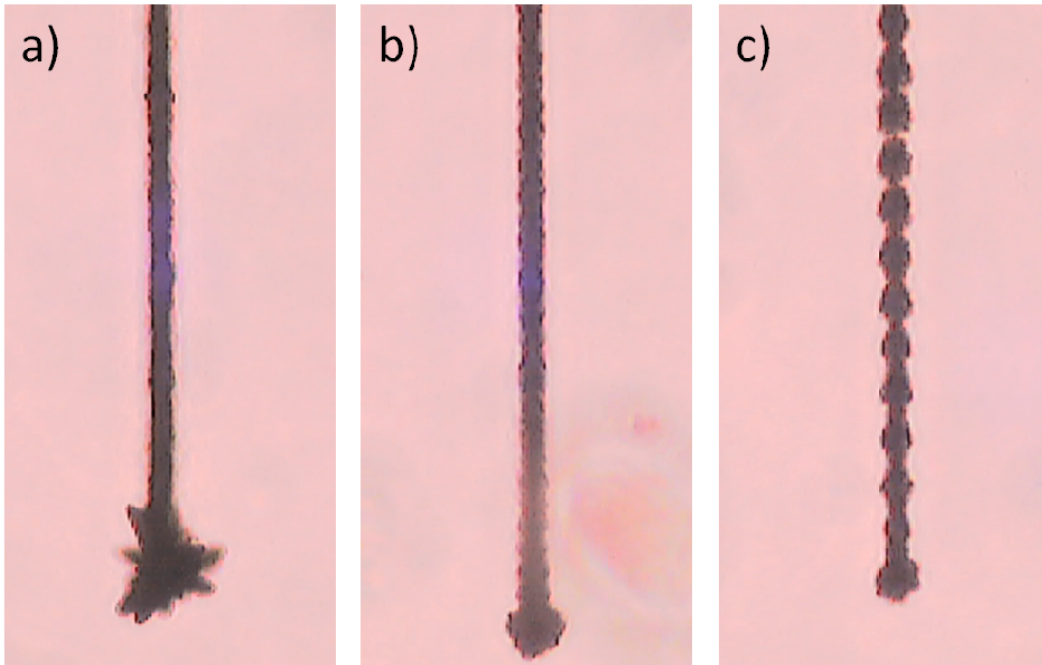


Figure 14: Top view of channels fabricated at $100 \mu\text{J}$ by a 0.65 NA objective. Pulse separations of $1 \mu\text{m}$ (a) and $5 \mu\text{m}$ (b) yield smooth channels. The channel with $10 \mu\text{m}$ spacing (c) is heavily scalloped, but largely continuous; above this spacing, channels were heavily gapped.

Chapter 6

THREE DIMENSIONAL FEATURES FABRICATED BY LASER ABLATION

Tolerances and Design Rules

In the previous chapter, a process that resulted in functioning channels and vias was developed. In this chapter, some simple three dimensional devices will be explored. One crucial step in converting a process for simple features into a process applicable to a system of devices is determining its design rules. These are the set of rules for a process which guarantee a final working device (or, at the least, feature fidelity).

First, there are rules imposed by the system design. Since we are fabricating features with light entering from the top of the PDMS chip, features at a lower depth need to be fabricated first. Attempting to fabricate a feature under a pre-existing one can result in attenuation of the beam, and distort the feature. This rule was implemented in the simple CAD design – machine code parser written as part of the software package for the system. One important difference between this technique and conventional surface laser machining is that the cutting direction for vias is reversed. In our case, a via is initiated in the bulk material, and the laser focus is then moved up towards the surface; this ensures that the ablated via does not obscure the incident laser beam.

For features such as corners, where the stages accelerate rapidly, optimal results were obtained by triggering the laser based on stage position output[28]. This ensures an even spatial distribution of pulses, which is not the case when pulse spacing is controlled by firing at a fixed frequency and

varying the stage velocity. This is less important at lower stage velocities, and was implemented only for lateral stage motion.

In addition to laser pulse energy and voxel spacing, there are two process-based rules that need to be determined: minimum channel-to-channel spacing in both vertical and horizontal directions. For a complete process description, the minimum spacing requirements for vias should also be determined. Since vias were typically used singly, or with wide separations, this tolerance was not determined. Channel spacing tolerances were determined by ablating arrays of channel doublets at varying channel-to-channel separation distances. Both the lateral and vertical arrays were fabricated with 100 μJ pulses spaced 5 μm apart, as these parameters had been established as giving acceptable channel quality. For vertically spaced channels, a minimum separation 15 μm greater than the channel height (in this case, 115 μm of separation in the stage frame) resulted cleanly separated channels (Figure 1). For laterally spaced channels, this is approximately 25 μm for fully separated channels, and 40 μm for distortion-free features (Figure 2). Residual stress from the ablation process may account for the distortion effects; in some cases, the second channel ablated will be highly curved. Another possible cause is that as the spacing is reduced, the conical incoming beam is partially shadowed by the initial channel, resulting in a distorted second channel. If we envision the converging beam as a cone of light, then the minimum separation distance will occur when this cone is in contact with the top of the first channel. Solving geometrically for a minimum channel spacing δl with a channel height h_c gives:

$$\delta l = h_c \tan\left(\sin^{-1}\frac{NA}{n}\right)$$

Applying this to our channels, a nominal height of 100 μm yields a minimum lateral separation of 51 μm , which is fairly consistent with the measured 40 μm . We now have a set of process rules, which can be used to fabricate more complex devices.

Three Dimensional Structures

The first three dimensional devices fabricated were fully embedded vias between two channels at different depths. An example is shown in Figure 3. The working distance of the optical system used, combined with the channel height, allows for multiple overlapping layers to be fabricated. This enables more complicated three dimensional topologies, such as the crossover shown in Figure 4a to be fabricated. With crossovers, networks of channels with arbitrary connectivity can be fabricated; for larger scale chips this would allow for systems such as nested arrays. Crossovers are ablated sequentially by feature depth, rather than as a series of continuous moves. Thus, to ablate a higher level channel, the stages need to return to the endpoint of the connecting via. To ensure that good fluidic connections are made, it is helpful to add a small amount of overlap at junctions. Only a small amount – as little as 10 μm – is necessary.

Structures with true three dimensional curves, such as coils, were also fabricated. These require smooth control of the stages at constant vectorial velocity; they also demonstrate the abilities of backlash-free stages. We were able to demonstrate fluid flow in coils, however, the pressures required to clear the channels of the ablation residue were much higher (40 psi) than expected compared to channels of equal length (10-20 psi). Sharp junctions, especially those involving changes in depth appear to be prone to blockage by ablation residue. Coils with radii as small as 25 μm were successfully fabricated.

In the future it may be possible to fill such coil structures with a conducting fluid, or perhaps solid metal[29]; they could then function as fully embedded electromagnets. One direct application of such coils is on-chip electric actuation of an embedded magnet. Coils such as the one shown in Figure 5 with a central channel could potentially be used to trap magnetic particles. Attempts were made to fill coils at various geometries with gallium. Since gallium is liquid at room temperature, metallic, and unlike mercury, fairly nontoxic, it is a good choice for such a task. Unfortunately, it is also extremely viscous compared to water, and could not be forced through the channels at available pressures.

The development of design rules, embedded vias, and crossovers demonstrate the ability of this instrument to fabricate complex, multi-element structures. The ability to fabricate helical structures capable of fluid flow opens the door to direct integration of magnetic on-chip functionality. This instrument is thus a powerful tool for fabricating truly novel microfluidic devices.

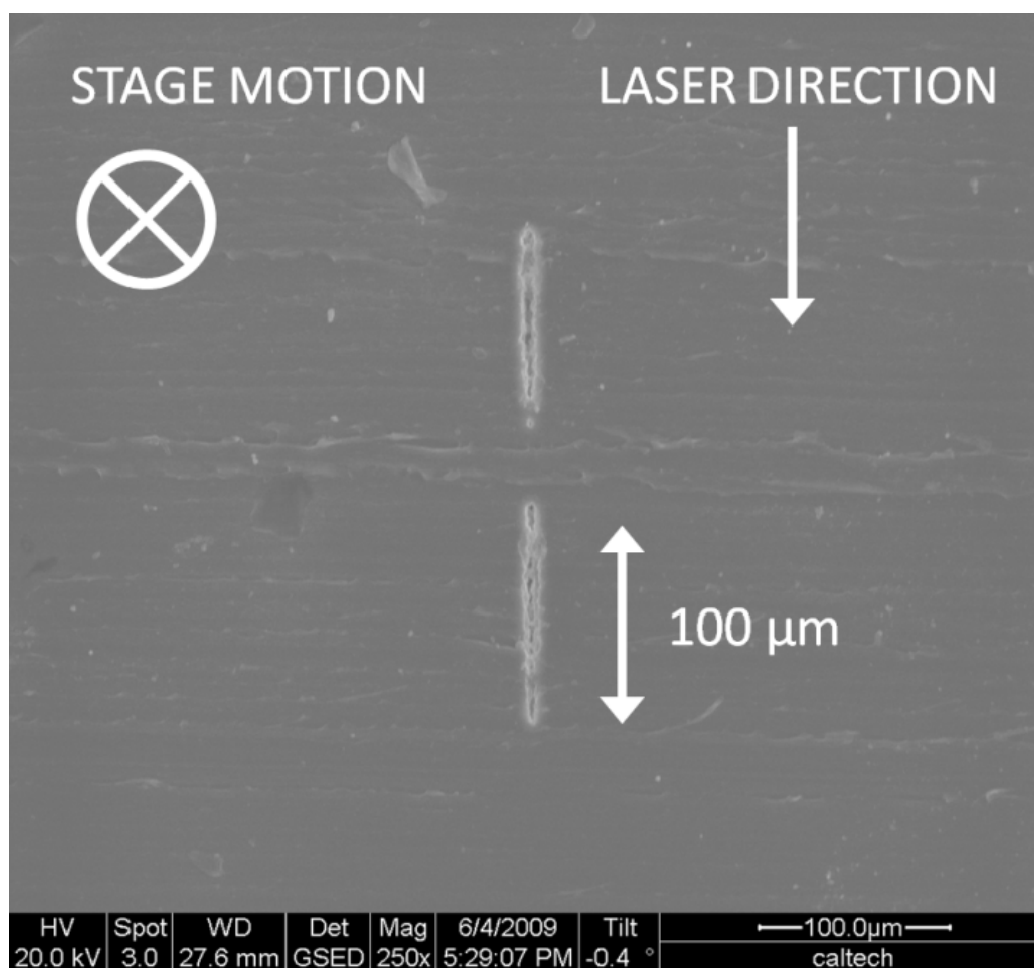


Figure 1: Two vertically spaced channels, with a center-to-center spacing of 115 μm in the stage coordinate frame.

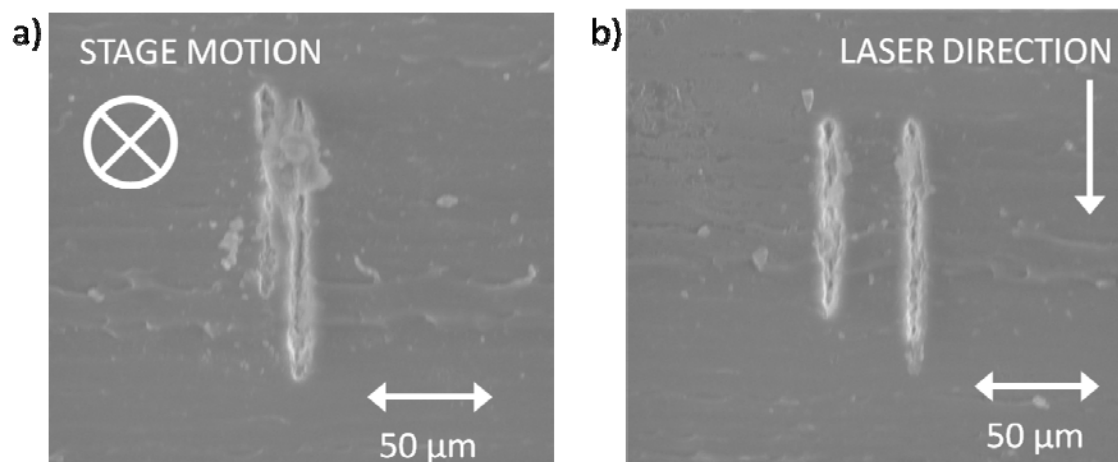


Figure 2: Lateral separation tolerancing pairs. At a separation of $20\ \mu\text{m}$ (a), the channels are distorted, and may overlap; at a separation of $40\ \mu\text{m}$ (b), the channels are discrete and well-formed.

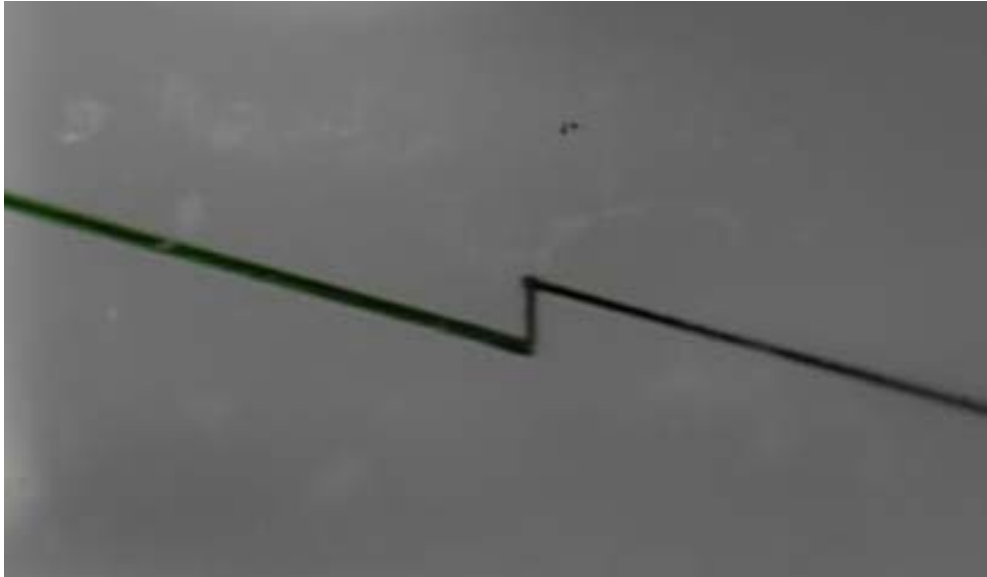


Figure 3: Single vertical via used to connect two channels at different depths; the channels are vertically spaced by $300\ \mu\text{m}$ in the stage frame (about $500\ \mu\text{m}$ in the PDMS). The structure has been flushed of ablation residue with water, and filled with green dye.

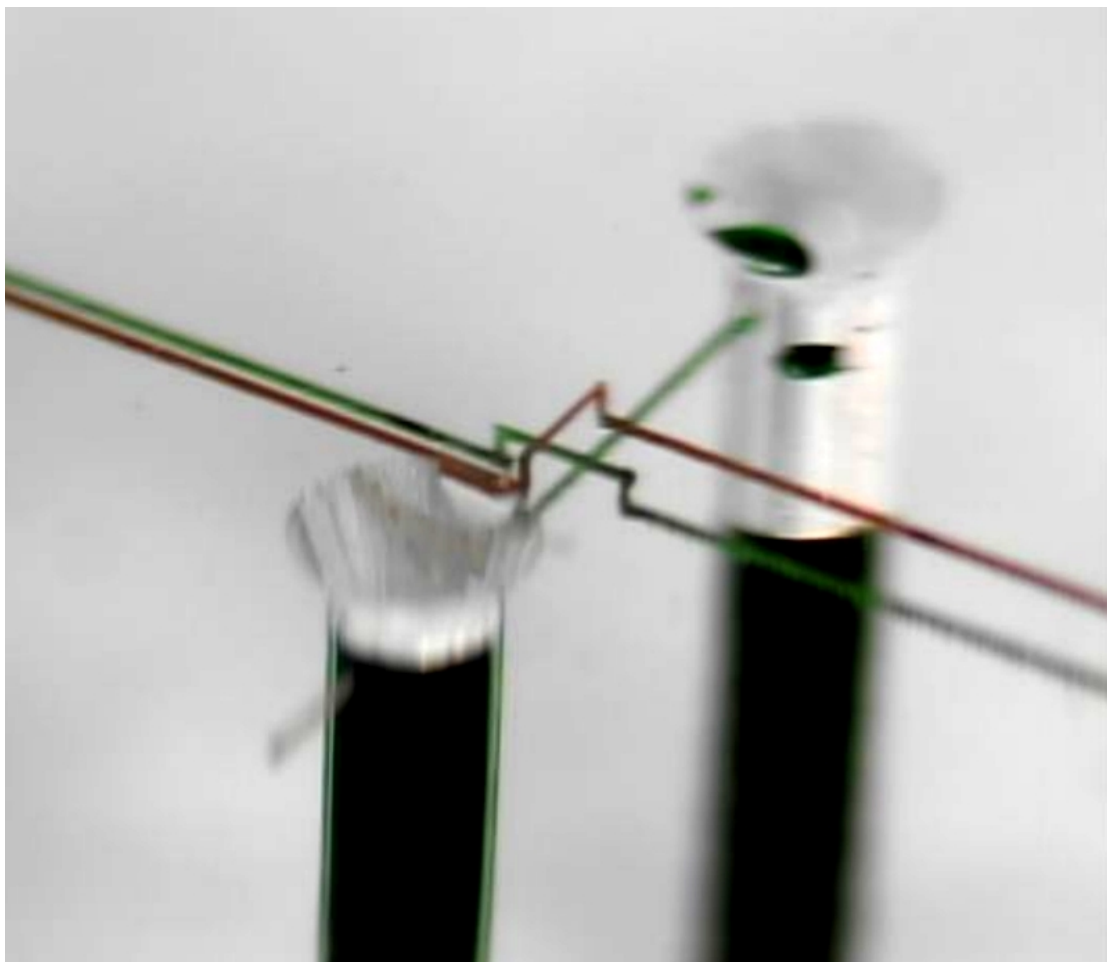


Figure 4: A three level crossover with 200 μm vertical channel-to-channel separation is imaged with colored dyes. Note the small overlaps at the crossover corners (most visible on the central channel); adding small overlaps at corners ensures a good fluidic connection.



Figure 5: A vertical via, filled with red dye, is surrounded by a helical water-filled channel; the spiral has a radius of $100\ \mu\text{m}$ and nominal total height of $392\ \mu\text{m}$. The central via is $520\ \mu\text{m}$ tall; the maximum depth for channels in this process is $620\ \mu\text{m}$.

Chapter 7

FLUID FLOW CHARACTERISTICS OF CHANNELS AND VALVES

Channel Flow Characteristics

While properly-ablated channels are continuous, they are filled with ablation waste products. When pressure is applied, the byproducts are flushed out, and the channel visibly clears. As long as the minimum channel dimensions are larger than the maximum size of the byproduct, flow may be reliably obtained. Channel dilation under applied pressure assists this process. Typical threshold pressures for initiating flow were in the 65 to 140 kPa (10-20 psi) range, with larger channels requiring a lower initial pressure. Once a channel has been cleared, the threshold pressure for flow drops, in some cases to a few 10's of kPa, due the removal of the obstructions.

While traditional surface-style PDMS channels may delaminate from neighboring layers under pressure, the limiting factor to applied pressure for the embedded channels is the fracture strength of the PDMS itself. This allows for an interesting phenomenon – highly nonlinear flow resistance. For laminar flow in a pipe with a constant cross section, the flow rate may be linearly related to the applied pressure, exactly as current and voltage are related in a resistor. This holds as long as the flow remains laminar – with a Reynolds number under 2000 – and the cross section is nearly constant. For our channels, the Reynolds number is:

$$Re_c = \frac{2r_c\rho\bar{u}}{\mu}$$

Here, r_c is the minimum length scale of the pipe cross section, ρ is the density of water (1000 kg/m³), \bar{u} is the average velocity, and μ is the viscosity (8.9 x 10⁻⁴Pa.s at STP). Picking a flow rate of 10 μ L/min and nominal channel dimensions of 10 μ m x 100 μ m, we obtain a Reynolds number of 0.37. These dimension and flow rates are typical of those encountered in microfluidic systems. With a Reynolds number this low, laminar flow is assured, despite the roughness of the channel walls.

When the pipe can deform as a function of pressure, flow resistance ceases to be linear. PDMS has a relatively low Young's Modulus E (1 MPa)[30]. With devices capable of withstanding the maximum pressure we can apply (50 psi – 344 kPa), we can induce significant channel deformation.

As has been demonstrated in the case of conventional rectangular channels[31], the elasticity of PDMS results in channel deformation under pressure, reducing the fluidic resistance. In our case, we have a non-rectangular channel. We will use a thin channel approximation[32] for a channel of thickness t to determine the flow rate Q for a differential channel length dz :

$$Q = -\frac{1}{12\mu} \frac{dP}{dz} \int t^3(x) dx$$

A channel can be modeled as a double vertical parabola of height h and thickness w . Since the majority of pressure-induced channel deformation will occur on the sidewalls, this is a reasonable approximation. This yields the following flow rate for a differential length:

$$Q = -\frac{dP}{dz} \frac{4w^3h}{105\mu}$$

Channel expansion can be approximated to first order by adding a pressure term to the channel width. Since PDMS is soft but incompressible, stress on the horizontal axis can be converted into strain on the vertical one, which then allows the channel to expand. Following a scaling law approach[31] with pressure as the applied stress results in:

$$w = w_0 \left(1 + \frac{Pw_0}{Eh} \right)$$

Integrating the pressure along a channel of length L gives:

$$P = \frac{Ew_o}{h} \left[\left(\frac{105\mu QL}{Ew_o^4} + 1 \right)^{\frac{1}{4}} - 1 \right]$$

This model was tested by measuring flow-pressure curves for several 5 mm long channels ablated at 50, 100, and 150 μ J. Flow was generated by connecting a water-filled Tygon Microbore line to a regulated nitrogen supply. Pressure near the input of the channel was read from a Dwyer DPGW-07 gauge connected in to the input of the channel with a T-junction and tubing; all of the piping was water filled, and visually checked for bubbles. Flow was measured with a flowmeter (Upchurch Scientific) connected in series with the channel under test.

When making precision pressure-flow measurements, it is helpful to consider the flow resistances and deformations of the testing equipment in the same way one would consider parasitic resistance and capacitance in the context of electronic testing. In this case, the calculated parasitic resistance of the Microbore tubing (0.61 kPa-s/ μ L for a one meter length) is negligible compared to the

resistance of the channels (1260 kPa-s/ μ L for a 5 mm channel), as was the measured resistance of the flowmeter. Thus, a flowmeter coupled to a water-filled Microbore line may be placed in series with a channel without fear of distorting the measurement.

Initial attempts to use a syringe pump as a constant current source with a pressure gauge connected just above the channel entrance, however, worked poorly. The parasitic fluidic capacitance (deformation of the syringe body, tubing, and pressure gauge), coupled with the resistance of the channels led to exponential decay constants ranging from 10 minutes to several hours, depending on fluid flow rates. The effective fluidic capacitance of the syringe-pressure gauge system was measured by directly connecting the pump to the gauge, and measuring the pressure-displacement curve. This is directly analogous to hooking up a constant current source to a capacitor, and measuring the voltage over time to determine capacitance.

Using regulated nitrogen as a pressure source and measuring the flow, however, effectively removed the parasitic fluidic capacitance of the pressure gauge from the system. This allowed for measurement times faster than 30 seconds.

The resulting data was fitted to the model, and values for h , w_0 , E , and L were extracted. Extracted values for L and h were consistent with their expected values; however, the fitted width and value of Young's Modulus were not. In general, the smaller, lower aspect ratio channels (cut at 50 μ J) showed much higher values of E (5-10 MPa). For larger channels, with higher aspect ratios, values of E were somewhat higher (1.3 MPa) than reported results[30]. The largest difference, however, lies in the extracted channel width. The effective channel width was a factor of 3-10 smaller than that expected from SEM imagery. This is likely caused by several factors; the imaged channels

contained ablation residue, which may have forced the channels open; the ablation process may induce stress in the sidewalls, causing them to close when the residue is removed; finally, the roughness of the channel wall may effectively extend the no-slip boundary condition to a point inside the channel, i.e., the surface roughness may create a stationary flow boundary layer.

An interesting effect occurs when the channels have been maintained in the wetted condition for roughly one hour; the fluidic resistance increases. When the flow curve for a channel tested in the initially dry state is compared to a comparable curve for the same channel in the wetted state, and channel parameters extracted by fitting, the value for E is fairly constant, but the channel width w approaches zero. For the flow curves shown in Figure 1, the extracted values of h and E were 1.2 μm , and 1.3 MPa for the dry case, and 0 μm , and 1.4 MPa for the wet case. This effect is repeatable; if the same channel is allowed to dry, and then re-tested in the initially dry and wetted conditions, similar curves are obtained. Since bulk PDMS does not swell with water, this suggests that the ablated surface does; either due to the remaining ablation residue swelling or another surface modification caused by the ablation process, such as increased porosity caused by micro cracking.

Another possible explanation for this is a change in the surface over time, from a hydrophobic state to a hydrophilic one. The above flow resistance analysis assumes a no-slip boundary condition for flow inside the channel. This means that, at the PDMS-water boundary, the water velocity is always zero. PDMS is naturally hydrophobic, and for extremely hydrophobic surfaces the no-slip condition may not hold. The water could thus slip by as more of a solid plug, with lower associated flow resistance. However, since PDMS has only single bonds in its backbone, elements along the polymer chain are free to rotate. Thus, if the polymer chain contains hydrophilic side groups,

perhaps as a result of the ablation process, these would migrate towards the channel walls during prolonged exposure to water. After enough time, the wall would change to a hydrophilic one, restoring the no-slip condition and increasing flow resistance.

Valves

The nonlinear flow effect lends itself to fabricating valves; since fluidic resistance is such a strong function of channel width, actuating this should strongly control flow rates. Simple “pinch” valves were fabricated by ablating two gate channels on either side of a central channel; side and top views are shown in Figures 2a and 2b. These gate channels were then pressurized with nitrogen to actuate the valve. This applied pressure caused the gate channels to expand, and thus constrict the central channel (Figures 2c and 2d). By controlling the constriction of the channel, flow can be reduced, or completely halted. Pressure at, or greater, than the channel pressure must be applied to the gates to stop the flow completely, however, flow can be largely halted with gate pressures less than this (Figure 3). Sweeping the channel pressure at different gate pressures yields a set of flow curves similar to channel flow curves for increasing values of Young’s modulus, i.e., increased stress on the central channel (Figure 4). These are analogous to the IV curves used to characterize MOS transistors. To date, only valves with fairly long gates (1mm) have been fabricated. Given the strong dependence of fluid resistance on channel width, and the fairly short region (100 μm) over which the channel visibly constricts, it should be possible to fabricate working valves with much shorter (perhaps 200 μm) gate lengths.

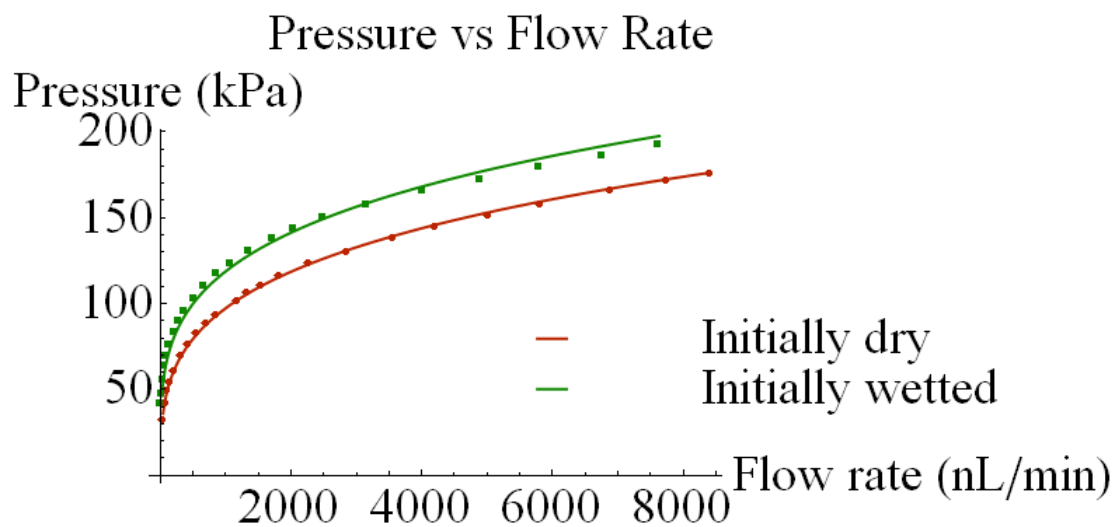


Figure 1 – Pressure vs. flow rate for single channel under initially dry and initially wetted conditions. Points are data; smooth lines are the associated fits to equation 4. This particular channel was cut at $100\ \mu\text{J}$ with a pulse spacing of $3\ \mu\text{m}$.

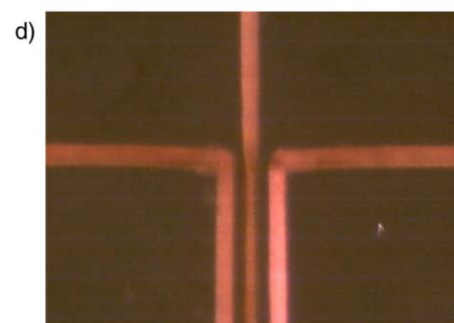
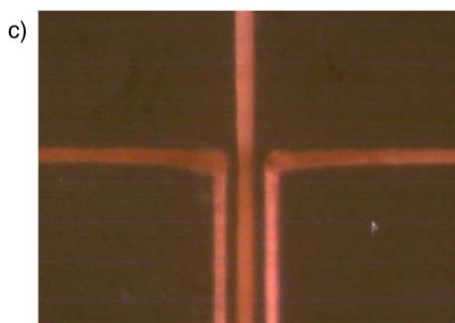
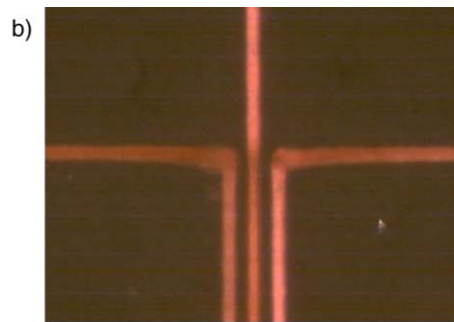
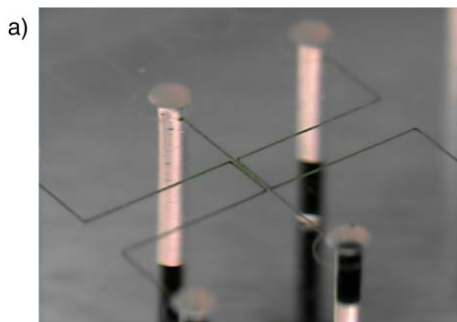


Figure 2: Figure a) shows a pinch valve with a 1mm gate length, and 4.5 mm total channel length imaged with green dye. Figure b) shows a similar valve, cut at 100 μJ with 5 μm pulse spacing, and nominal gate-to-channel separation distance of 30 μm ; all channels are unpressurized. When pressurized at 30 psi (207 kPa), the center channel expands (c); when the gate channels are also pressurized to 40 psi (276 kPa), they expand and constrict the central channel (d).

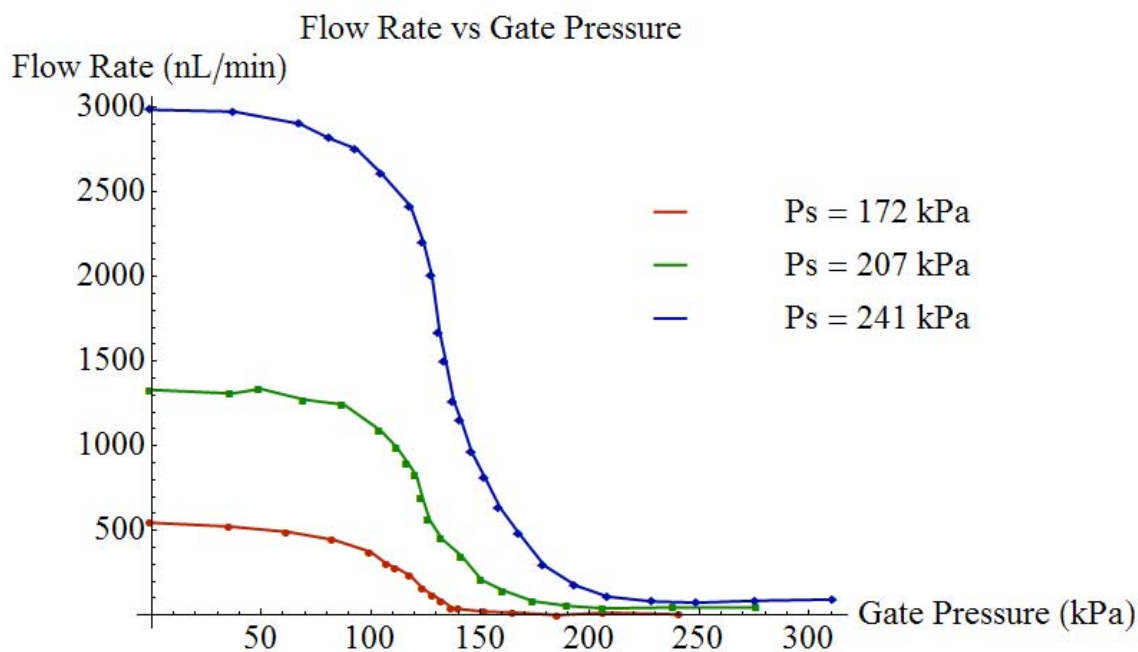


Figure 3: Flow rate vs. gate pressure for valve with a 1mm long gate region (4.5mm total channel length), 35 μm gate-channel spacing, cut at 100 μJ with 5 μm voxel separation.

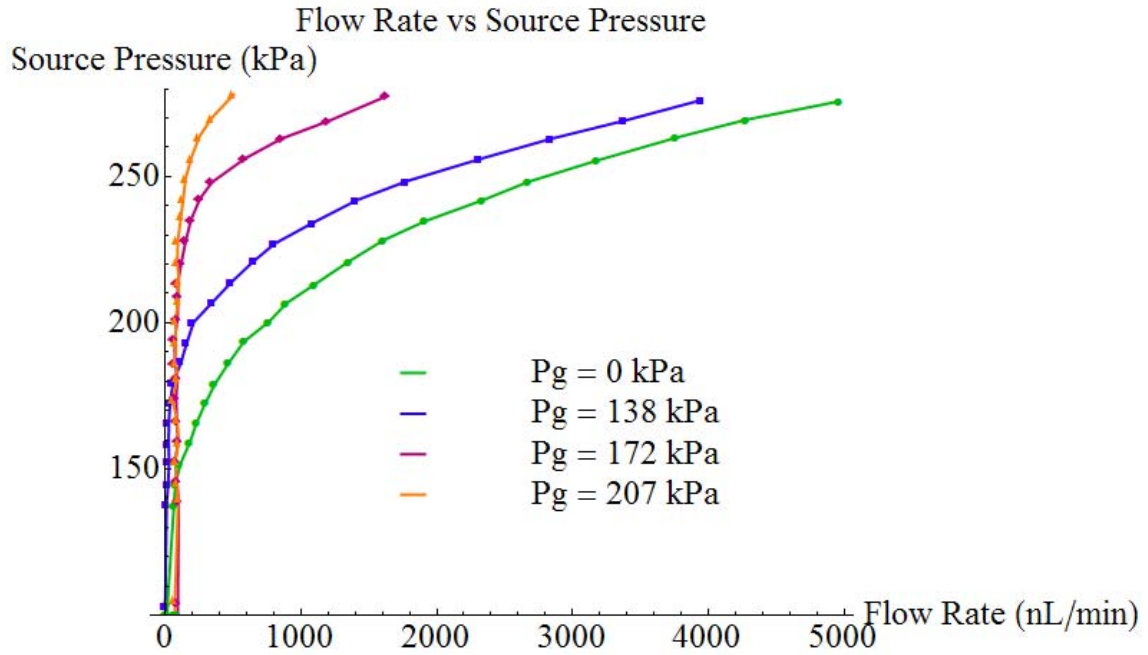


Figure 4: Flow rate vs. source pressure for the same valve as in Figure 3, at a variety of fixed gate-drain pressures.

Chapter 8

FUTURE WORK

The material presented in this thesis so far covered the two largest projects attempted during my graduate research. Many other projects were also worked on along the way, and some of them have potential for future research. Four of these are presented in this chapter; two based on further work in ablation, and two which present unique approaches to building microfluidic systems.

Alternate Materials for Ablation

In addition to PDMS, this ablation process can be used with other transparent materials. PDMS was chosen simply for its ubiquity within the field of microfluidics, and for the comparative ease with which samples can be connected to existing fluidic test infrastructure. This system was also tested on two other materials, glass and acrylic. Performing volume ablation with acrylic was straightforward; channels could be easily cut within a solid block. Fluidic testing requires drilling into the block to connect to features, and sealing a capillary tube to the block; for this reason, the fabrication of devices in acrylic has been relegated to future work.

Glass proved to be a much more difficult material to process. Machining simple voxels into glass proved straightforward. Continuous channels, however, often resulted in shattered chips. Glass is extremely brittle, and the thermal stress associated with laser machining typically resulted in crack formation. A process to fabricate vias in fairly thin (1mm) glass chips was developed (Figure 1). It relied on minimizing pulse energy, surrounding the chip with a working fluid (water), and starting the via at the surface of the chip; this resulted in a continuously wetted via during ablation. Wetting the chip may have helped to damp the ablation-induced shock wave, thus limiting crack propagation, and also reduced thermal stress by cooling the ablated region. Suspending the chip in

water also assisted the ejection of the ablated glass from the via. Productive future work on glass would likely require either an ultrafast laser to minimize thermal damage, or the development of a combined ablation/photochemical process.

Microfluidic Chips Configured by Laser Ablation

The bulk of this thesis has focused on ablating three dimensional structures, or structures which are embedded within a block of PDMS. The ablation system may also be used to modify existing PDMS structures fabricated through conventional soft lithography techniques. Since conventional microfluidic chips typically have layers under 100 μm thick, the laser processing time required to ablate a hole between two layers is small (potentially under a second). This raises the possibility of using the automated laser ablation system as a fast processing step to quickly customize microfluidic systems.

To take advantage of this capability, one would produce a large number of some standard type of microfluidic chip in advance, and then determine its functionality by later connecting the proper pathways through laser ablation. This approach is similar to that taken by the electronics industry with the development of PROM (programmable read-only memory) and FPGA (programmable gate array) chips. An FPGA allows the user to purchase a generic chip, and program in logic functionality at the time of use. Since the basic chips are mass produced, this functionality comes at a much lower cost than, say, producing a custom chip for every application.

To test this idea, we are currently developing a generalized microfluidic chip specifically for laser customization. This is a simple two layer chip, composed of arrays channels and overlapping cavities in both layers. In its normal state, none of the channels connect. However, by ablating

small vias between the channels and cavities, fluidic connections between arbitrary points on the chip may be made. The connectivity of the chip can thus be “programmed” by automated laser ablation. A layout of the chip is shown in Figure 2, and a picture of one of the early generations with ablated vias is shown in Figure 3. This chip is aligned to the system by a set of ablation fiducials, and once aligned, may be modified with fully automatic control.

At present, the chip is simply designed to allow for arbitrary routing of fluidic connections. Future versions may include functional blocks containing valves, multiplexers, and more complex devices, which would then be connected in a custom sequence by ablation.

Analog Microfluidic Systems

Standard PDMS microfluidic chips are composed of some combination of channels, and pressure-actuated valves. The valves are simply crossovers between two channels which may be closed by applying adequate pressure to one of the channels, compressing the other. Systems using these chips typically relegate pressure control and valve actuation to equipment located outside of the chip. These devices – pumps, pressure regulators, solenoids, etc – are bulky, and not amenable to miniaturization. In addition, creating reliable, miniaturized connections to microfluidic circuits is still somewhat challenging. The end result is often a miniaturized chip surrounded by a lab bench full of connecting tubing and support equipment. For devices designed to operate in field environments, it would be desirable to a) regulate pressures entirely on chip, and b) reduce the number of control connections.

Towards that end, it is profitable to approach microfluidic chips not as arrays of digitally actuated valves, but rather as analog systems, and apply the well-developed base of analog circuit design theory to flow control problems.

The first step in this process is solving the flow equations for a valve. Valves made in the standard process used by the Caltech-KNI microfluidics foundry are based on channels roughly 12 μm tall, which have been rounded to a roughly parabolic shape. Typical valves are 100 μm by 100 μm squares at the where two channels overlap. As the valve closes, it forms a double parabolic saddle structure. Since this is a high-aspect ratio channel, its fluid flow may be determined by the approach used in the earlier nonlinear flow portion of this thesis. Solving for the fluid flow of this conduit yields:

$$Q = \frac{8wP}{105\mu L} \left\{ \frac{2h_c + 3h_0}{4h_c h_0^2} + \frac{3 \tan^{-1} \left(\sqrt{\frac{h_0 - h_c}{h_c}} \right)}{4h_c^{5/2} \sqrt{h_0 - h_c}} \right\}^{-1}$$

Here, Q is the flow rate, w is the width of the valve, L its length, P pressure across the drain and source of the valve, and h_0 and h_c the heights at the edge and center of the valve, respectively. Solving for the deformation of the valve as a function of applied pressure is significantly more complex, and beyond the scope of this work. The important result from this is that even with a simple linear deformation model, flow through a constricting gate is a highly nonlinear function of the channel geometry, and thus of the applied gate pressure.

As an initial test, valves were imaged under various conditions of applied gate-source pressure. A dye was used in the flow channel, allowing the surface profile of the valve to be extracted by image processing (Figure 4). The results confirm that the valve deforms in approximately the expected shape, and has a range of pressures for which it is partially open.

At this point, it becomes possible to perform system design. The valve has a highly nonlinear pressure-flow curve. Taking a small portion of that curve, and linearizing the valve function, we can build systems using the same small-signal models used for designing electronic amplifiers. Effectively, we are treating the valve as PMOS transistor, and channels as resistors. A variety of simple circuits were produced, including a 10:1 amplifier (Figure 5). Measurements of the circuit show small signal pressure gain slightly in excess of what was expected, but within experimental error. Analytical work remains to model valve actuation, as does significant circuit testing; eventually, it should be possible to develop microfluidic control circuits with the same tools used for electronic ones, such as SPICE.

Fabrication of Microfluidic Circuits in Printed Circuit Boards

Currently, most microfluidic devices are fabricated either in a soft lithographic process, injection molding, or via traditional photolithographic processes in glass. These processes all produce miniature, highly accurate devices, but require significant amounts of capital equipment. Because of the high capital equipment cost, devices become cheap only if produced in very large volume, and custom devices remain prohibitively expensive. If we can find a commercially available process which has the correct tolerances required for microfluidic devices, and adapt it with a modicum of effort, then we will be able to mass produce chips, including custom designs at low cost.

Printed circuit board (PCB) fabrication techniques are a natural fit to the problem of creating microfluidic chips. The size scales involved (50-100 micron traces) are the same size scales used in microfluidic chips for channels; the fabrication technologies have been well-developed by the electronics industry over the past 40 years, with associated reduction of production cost; finally, these techniques allow for easy integration of electronic systems with microfluidic ones.

PCBs are composed of alternating planar layers of insulating materials (FR4, polyimide, ceramics), and layers of conducting metals (copper, aluminum, gold) which have been defined through photolithography to form systems of traces, or conducting circuits. Holes between layers are drilled, and sometimes plated, to allow for vias, or vertical connections between layers.

The most common materials system for a PCB is one composed of FR4 (fiberglass in an epoxy matrix) for the insulator and copper for the traces. Boards are typically fabricated by performing photolithography and etching on a two-sided copper-clad FR4 core, drilling and plating holes for buried vias, and then laminating these cores together. By doing so, finished boards with an arbitrary number of buried traces and vias may be produced. Finally, holes for discrete components (semiconductor devices, resistors, etc) are drilled and plated, as are alignment and mounting holes. Boards are typically processed in the form of large panels, and later sawed (diced) into individual boards, allowing many discrete boards to be fabricated in a single batch.

Our goal is to adapt this material system to microfluidics with as little modification to the process as possible. If we can do this, then we can build microfluidic chips within the infrastructure developed for manufacturing PCBs. This means restricting ourselves to fabrication processes

which occur only *after* a completed PCB has been received from a supplier, and using only common, commercially available PCB processes.

The approach taken was to use the internal copper traces as sacrificial layers for microfluidic channels. A PCB would be fabricated by an outside supplier; the copper would then be etched out, leaving clear channels for fluid flow.

This was initially tested with a ferric chloride immersion etch on devices which were simple channels. It proved possible to remove the embedded copper, leaving a clear channel (Figure 7). The etch time required was impractical – nearly two weeks for a 5 mm long channel. A typical channel might have a height of 40 μm , a width of 200 μm , and length of 10 mm. Removing the copper by a wet chemical etch is thus equivalent to etching extremely high aspect ratio wells, and is limited by diffusion.

Removing the copper by chemical etch thus required defeating diffusion. This was accomplished through ultrasonic agitation, which reduced the time required dramatically (a factor of 30 for a 5 mm long test channel). The etch rate varies significantly based on channel geometry; still, reasonably sized, complex devices can typically be etched overnight (Figure 8).

This process thus opens up a prospect of affordable, highly custom microfluidic chips which can be fabricated with no user equipment more complicated than an ultrasonic etcher.

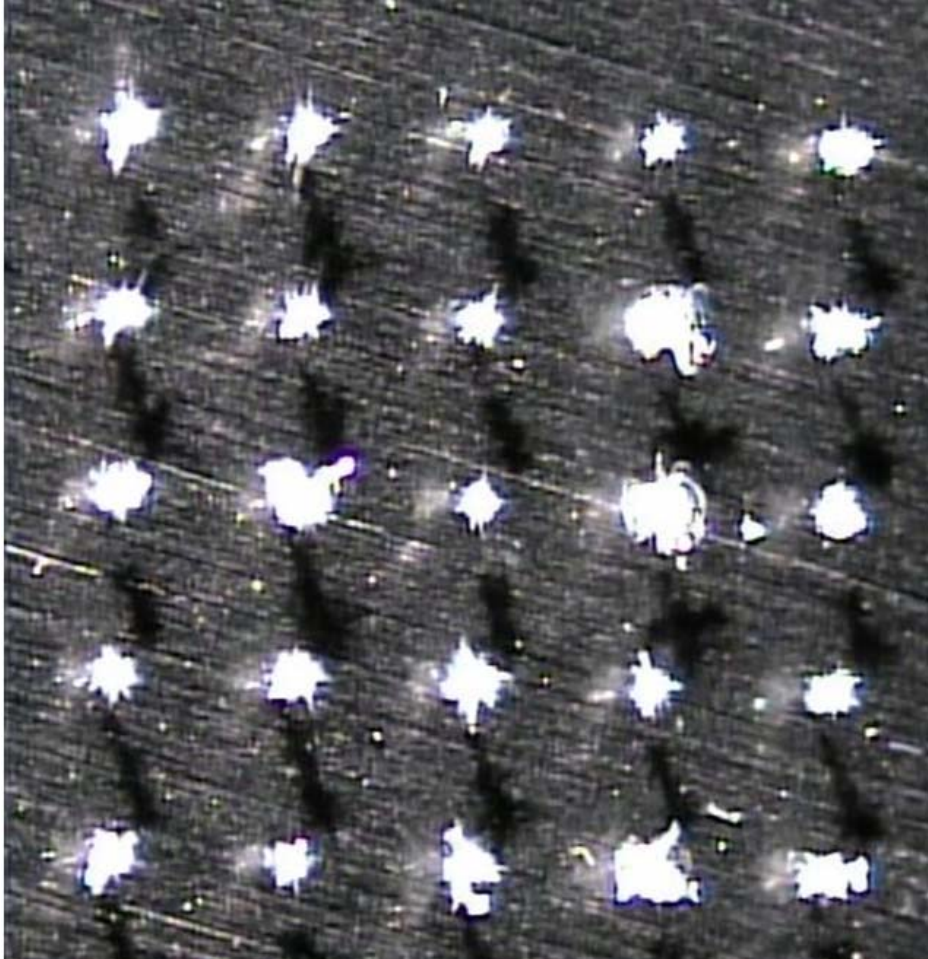


Figure 1: Array of vias cut in glass with a water-assisted laser ablation process. Even with carefully controlled powers, and immersion in water, the vias display significant spalling and cracking.

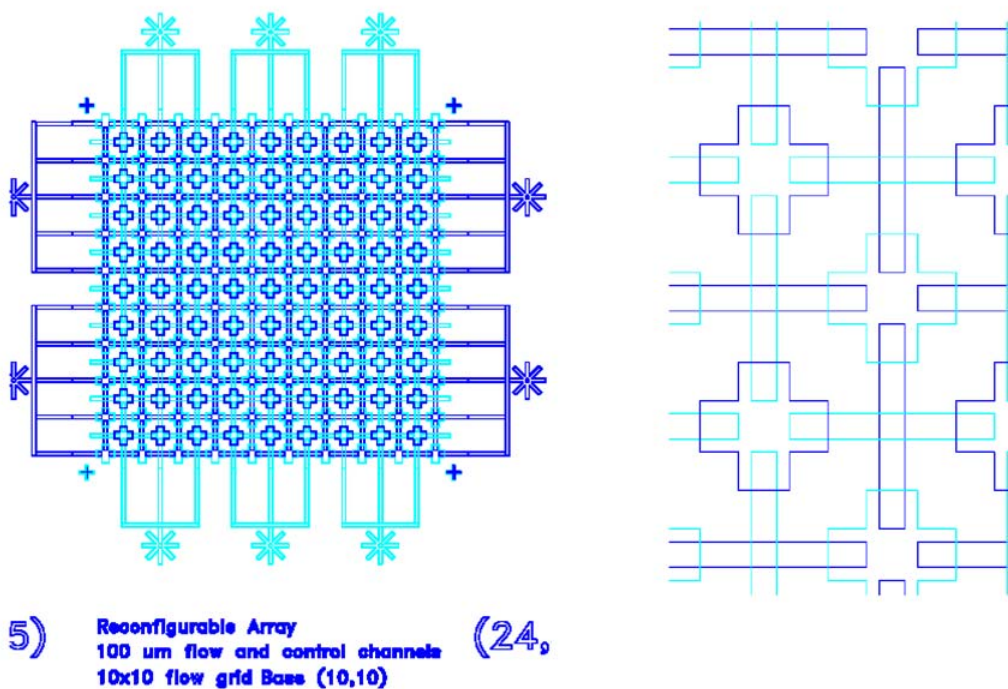


Figure 2: Layout of a microfluidic chip designed specifically for laser ablation. By ablating holes between the two layers (shown in turquoise and purple), arbitrary connectivity between channels may be obtained.



Figure 3: A microfluidic chip designed for generic connectivity after undergoing laser ablation.

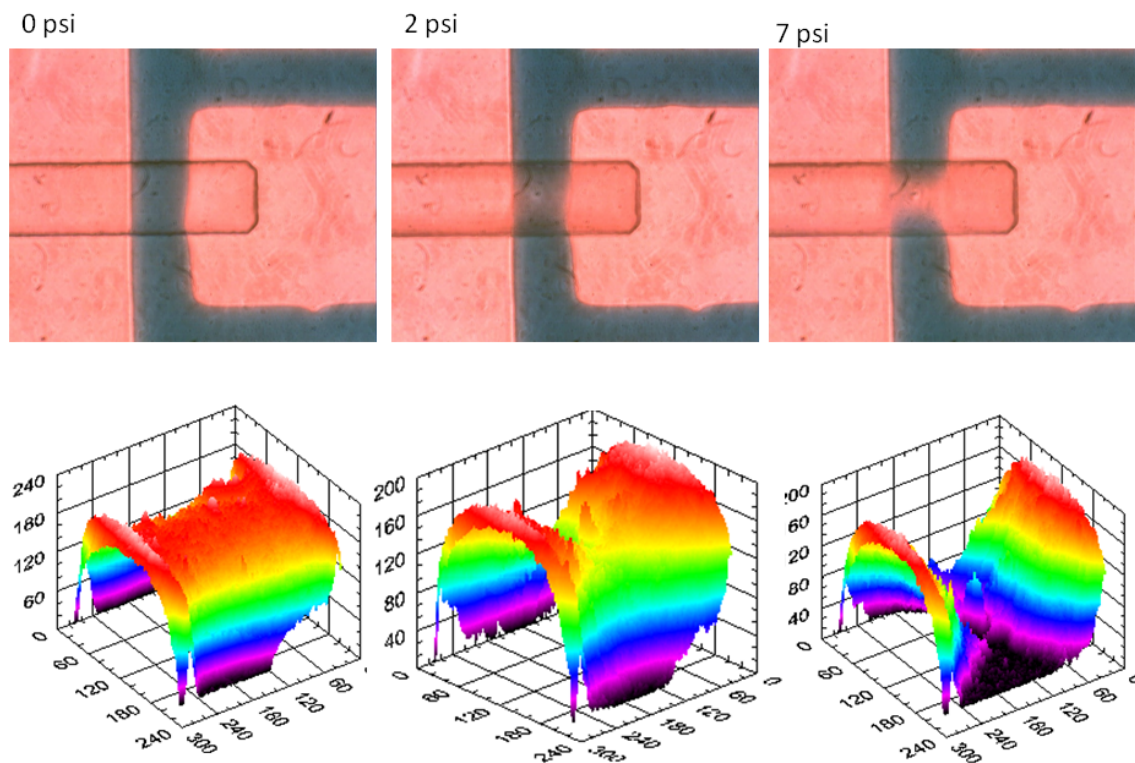


Figure 4: A microfluidic valve in three states of closure. Upper images show the valve with the flow channel filled with dye; lower images show the actual surface of the valve. At 0 psi relative pressure, the valve is fully opened, showing a roughly parabolic channel. With 2 psi differential pressure applied between the gate and channel, the valve begins to close, restricting flow. At 7 psi differential pressure, the gate closes completely, sealing the valve.

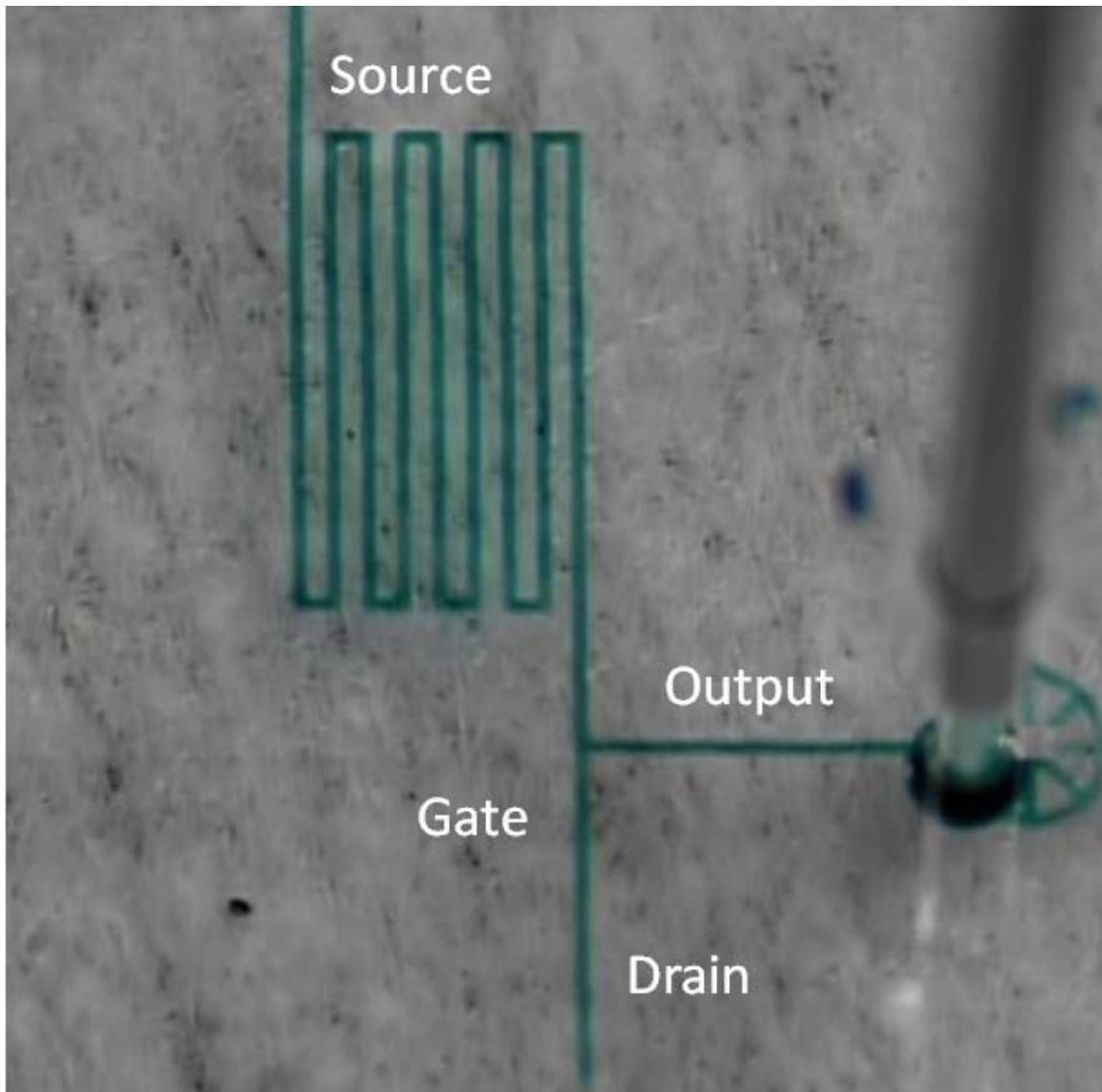
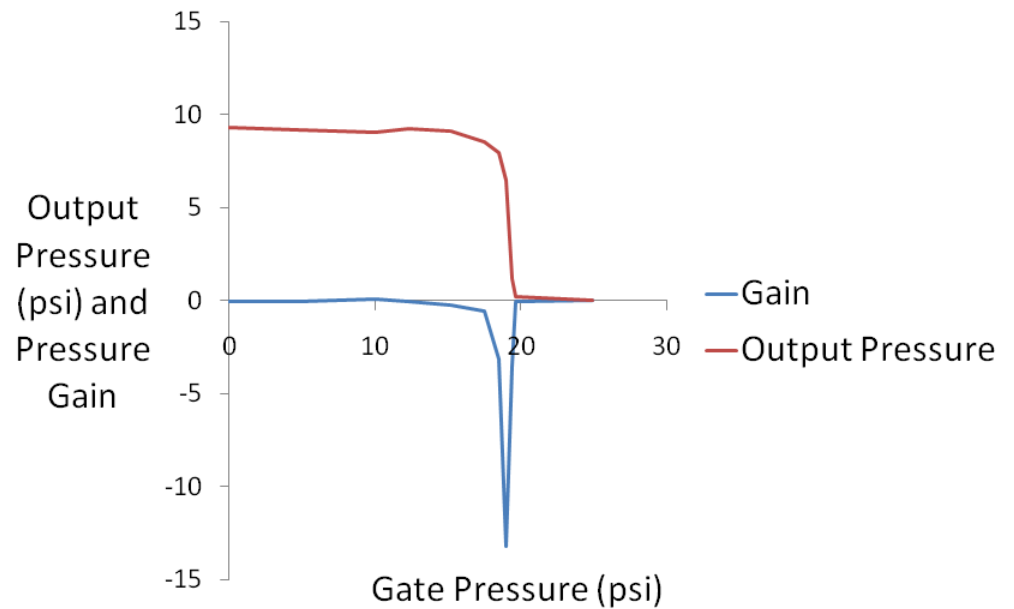


Figure 5: 10:1 common source fluidic amplifier. Water (dyed) enters from the top; the output is just above the gate channel (filled with air). After the valve, a small channel acts. Long channels on both sides of the valve act as resistors, which in this case are designed to provide a small signal amplification of 10.



10:1 common source amplifier
 Source pressure: 10 psi
 Gate pressure: 0-25 psi

Figure 6: 10:1 common source fluidic amplifier performance. This is quite similar to what one would expect from the analogous transistor amplifier. The circuit has a higher measured pressure gain (12) than expected, which is probably due to experimental error.

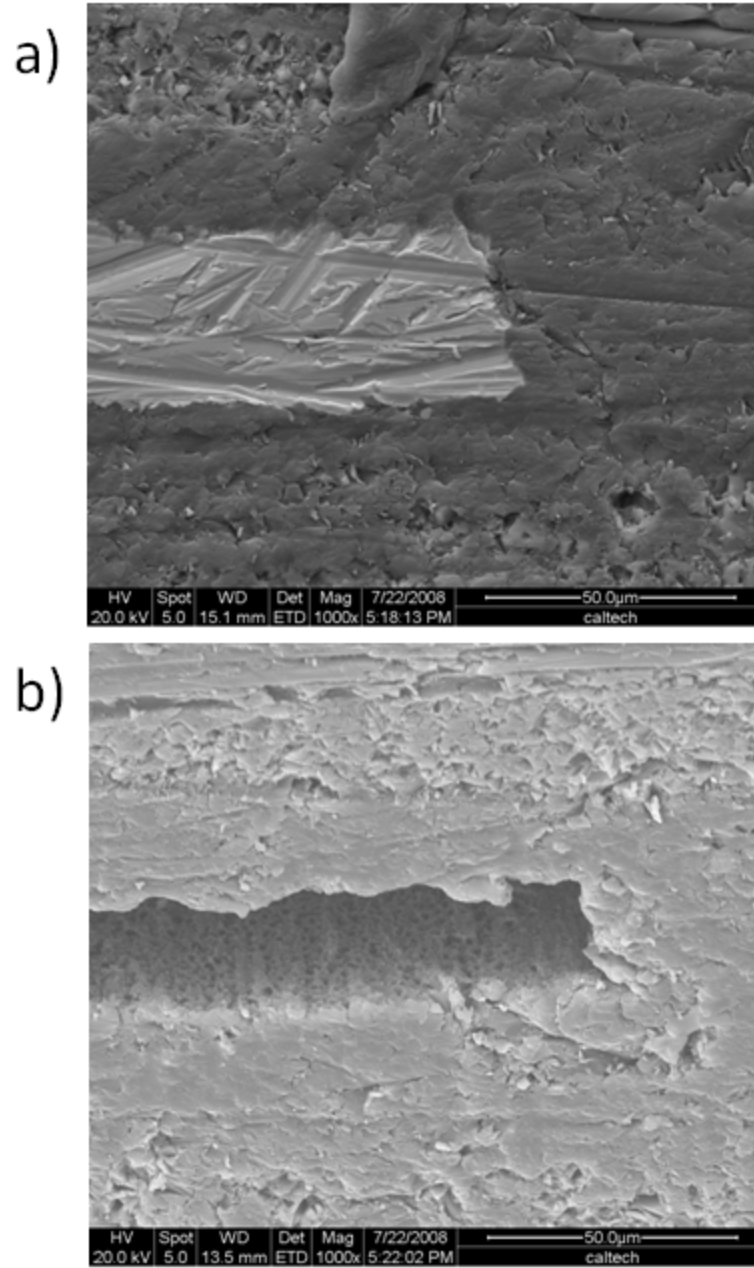
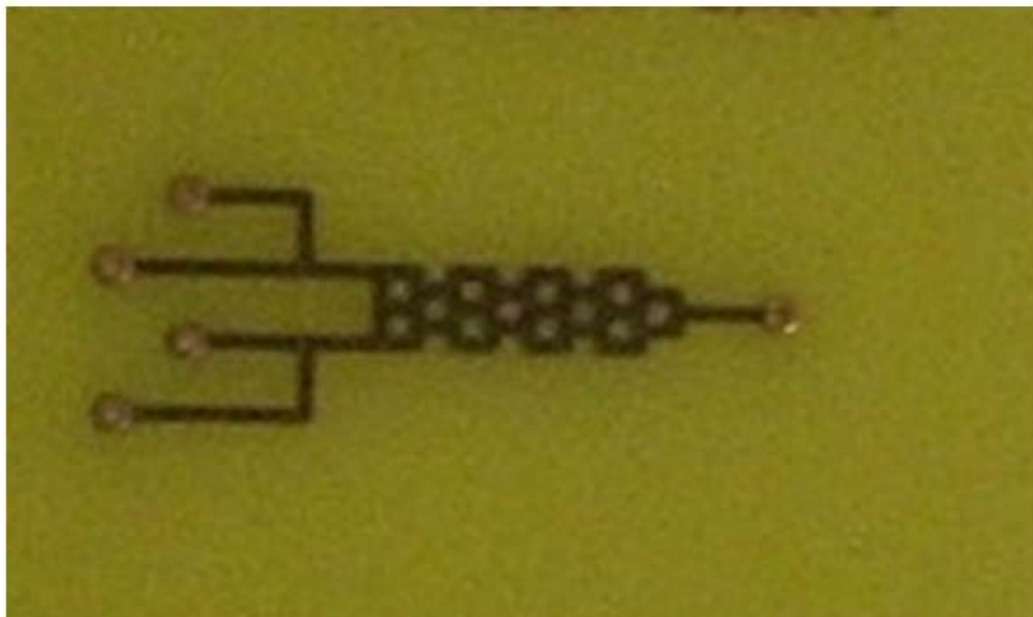


Figure 7: SEM image of a cross section of a PCB channels taken before and after etching. Channel height is about 40 microns.

a)



b)

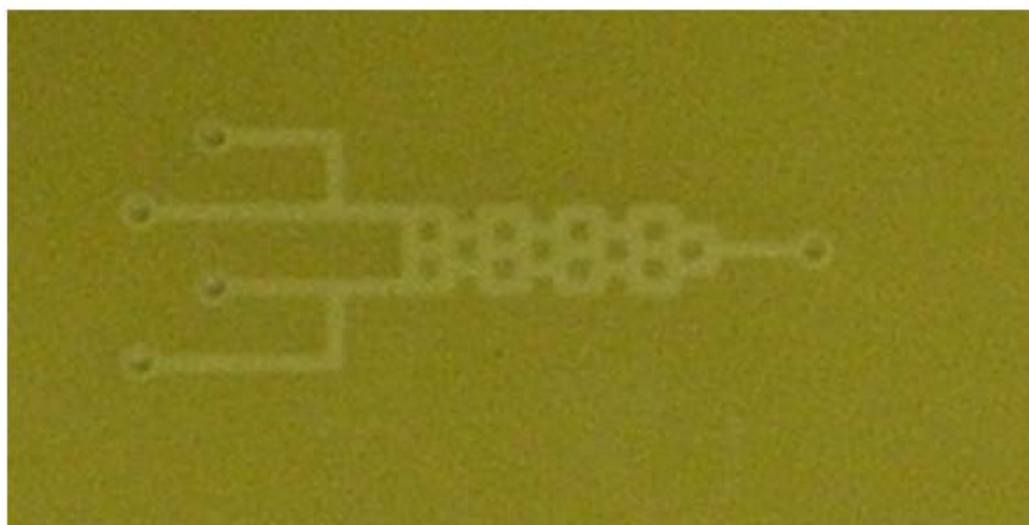


Figure 8: Microfluidic mixer fabricated in a printed circuit board (a), etched for 24 hours with ferric chloride under ultrasonic agitation (b). The total length of the mixer is about 1 inch.

- [1] D. C. Duffy, J. C. McDonald, O. J. A. Schueller, and G. M. Whitesides, "Rapid prototyping of microfluidic systems in poly(dimethylsiloxane)," *Analytical Chemistry*, vol. 70, pp. 4974-4984, Dec 1998.
- [2] S. R. Quake and A. Scherer, "From micro- to nanofabrication with soft materials," *Science*, vol. 290, pp. 1536-1540, Nov 2000.
- [3] M. A. Unger, H. P. Chou, T. Thorsen, A. Scherer, and S. R. Quake, "Monolithic microfabricated valves and pumps by multilayer soft lithography," *Science*, vol. 288, pp. 113-116, Apr 2000.
- [4] E. P. Kartalov, W. F. Anderson, and A. Scherer, "The analytical approach to polydimethylsiloxane microfluidic technology and its biological applications," *Journal of Nanoscience and Nanotechnology*, vol. 6, pp. 2265-2277, Aug 2006.
- [5] D. B. Weibel, W. R. DiLuzio, and G. M. Whitesides, "Microfabrication meets microbiology," *Nature Reviews Microbiology*, vol. 5, pp. 209-218, Mar 2007.
- [6] E. P. Kartalov, C. Walker, C. R. Taylor, W. F. Anderson, and A. Scherer, "Microfluidic vias enable nested bioarrays and autoregulatory devices in Newtonian fluids," *Proceedings of the National Academy of Sciences of the United States of America*, vol. 103, pp. 12280-12284, Aug 2006.
- [7] J. R. Anderson, D. T. Chiu, R. J. Jackman, O. Cherniavskaya, J. C. McDonald, H. K. Wu, S. H. Whitesides, and G. M. Whitesides, "Fabrication of topologically complex three-dimensional microfluidic systems in PDMS by rapid prototyping," *Analytical Chemistry*, vol. 72, pp. 3158-3164, Jul 2000.
- [8] B. H. Jo, L. M. Van Lerberghe, K. M. Motsegood, and D. J. Beebe, "Three-dimensional micro-channel fabrication in polydimethylsiloxane (PDMS) elastomer," *Journal of Microelectromechanical Systems*, vol. 9, pp. 76-81, Mar 2000.
- [9] T. Yasukawa, A. Glidle, M. Nomura, and J. M. Cooper, "Fabrication of robust 2-D and 3-D microfluidic networks for lab-on-a-chip bioassays," *Journal of Microelectromechanical Systems*, vol. 14, pp. 839-846, Aug 2005.
- [10] K. S. Yun and E. Yoon, "Fabrication of complex multilevel microchannels in PDMS by using three-dimensional photoresist masters," *Lab on a Chip*, vol. 8, pp. 245-250, 2008.
- [11] J. C. McDonald, M. L. Chabinyc, S. J. Metallo, J. R. Anderson, A. D. Stroock, and G. M. Whitesides, "Prototyping of microfluidic devices in poly(dimethylsiloxane) using solid-object printing," *Analytical Chemistry*, vol. 74, pp. 1537-1545, Apr 2002.
- [12] T. N. Kim, K. Campbell, A. Groisman, D. Kleinfeld, and C. B. Schaffer, "Femtosecond laser-drilled capillary integrated into a microfluidic device," *Applied Physics Letters*, vol. 86, p. 3, May 2005.
- [13] V. M. Graubner, R. Jordan, O. Nuyken, T. Lippert, M. Hauer, B. Schnyder, and A. Wokaun, "Incubation and ablation behavior of poly(dimethylsiloxane) for 266 nm irradiation," 2002, pp. 786-790.
- [14] D. J. Hwang, T. Y. Choi, and C. P. Grigoropoulos, "Liquid-assisted femtosecond laser drilling of straight and three-dimensional microchannels in glass," *Applied Physics a-Materials Science & Processing*, vol. 79, pp. 605-612, Aug 2004.
- [15] K. Ke, E. F. Hasselbrink, and A. J. Hunt, "Rapidly prototyped three-dimensional nanofluidic channel networks in glass substrates," *Analytical Chemistry*, vol. 77, pp. 5083-5088, Aug 2005.
- [16] M. D. Perry, B. C. Stuart, P. S. Banks, M. D. Feit, V. Yanovsky, and A. M. Rubenchik, "Ultrashort-pulse laser machining of dielectric materials," *Journal of Applied Physics*, vol. 85, pp. 6803-6810, May 1999.
- [17] B. C. Stuart, M. D. Feit, S. Herman, A. M. Rubenchik, B. W. Shore, and M. D. Perry, "Nanosecond-to-femtosecond laser-induced breakdown in dielectrics," *Physical Review B*, vol. 53, pp. 1749-1761, Jan 1996.
- [18] T. Suhara and H. Nishihara, "INTEGRATED-OPTICS COMPONENTS AND DEVICES USING PERIODIC STRUCTURES," *Ieee Journal of Quantum Electronics*, vol. 22, pp. 845-867, Jun 1986.
- [19] D. Taillaert, W. Bogaerts, P. Bienstman, T. F. Krauss, P. Van Daele, I. Moerman, S. Verstyuyft, K. De Mesel, and R. Baets, "An out-of-plane grating coupler for efficient butt-coupling between compact planar waveguides and single-mode fibers," *Ieee Journal of Quantum Electronics*, vol. 38, pp. 949-955, Jul 2002.
- [20] T. Baehr-Jones, M. Hochberg, C. Walker, and A. Scherer, "High-Q ring resonators in thin silicon-on-insulator," *Applied Physics Letters*, vol. 85, pp. 3346-3347, 2004.
- [21] T. Baehr-Jones, M. Hochberg, C. Walker, and A. Scherer, "High-Q optical resonators in silicon-on-insulator-based slot waveguides," *Applied Physics Letters*, vol. 86, p. 081101, 2005.
- [22] M. Hochberg, T. Baehr-Jones, C. Walker, J. Witzens, L. Gunn, and A. Scherer, "Segmented waveguides in thin silicon-on-insulator," *Journal of the Optical Society of America. B, Optical physics*, vol. 22, pp. 1493-1497, 2005.

- [23] M. Hochberg, T. Baehr-Jones, C. Walker, and A. Scherer, "Integrated plasmon and dielectric waveguides," *Optics Express*, vol. 12, pp. 5481-5486, Nov 2004.
- [24] K. Takada, H. Sun, and S. Kawata, "Improved spatial resolution and surface roughness in photopolymerization-based laser nanowriting," *Applied Physics Letters*, vol. 86, p. 071122, 2005.
- [25] J. W. Goodman, *Introduction to Fourier Optics*, 1996.
- [26] A. Yariv, *Optical Electronics in Modern Communications*, 1997.
- [27] J. T. Verdeyen, *Laser Electronics*, 1981.
- [28] F. E. Livingston and H. Helvajian, "Selective activation of material property changes in photostructurable glass ceramic materials by laser photophysical excitation," 2006, pp. 310-318.
- [29] A. Siegel, D. Bruzewicz, D. Weibel, and G. Whitesides, "Microsolidics: Fabrication of three-dimensional metallic microstructures in poly(dimethylsiloxane)," *Advanced materials*, vol. 19, p. 727, 2007.
- [30] J. Lotters, W. Olthuis, P. Veltink, and P. Bergveld, "The mechanical properties of the rubber elastic polymer polydimethylsiloxane for sensor applications," *Journal of Micromechanics and Microengineering*, vol. 7, pp. 145-147, 1997.
- [31] T. Gervais, J. El-Ali, A. Gunther, and K. F. Jensen, "Flow-induced deformation of shallow microfluidic channels," *Lab on a Chip*, vol. 6, pp. 500-507, 2006.
- [32] R. K. Shah and A. L. London, *Laminar Flow Forced Convection in Ducts* vol. Supplement 1, 1978.